OUKA
The University of Osaka
Institutional Knowledge Archive

Title	A Study on the Dynamic Nonprehensile Manipulation of Deformable Objects
Author(s)	Ixchel, Georgina Ramirez Alpizar
Citation	大阪大学, 2013, 博士論文
Version Type	VoR
URL	https://hdl.handle.net/11094/27556
rights	
Note	

The University of Osaka Institutional Knowledge Archive : OUKA

https://ir.library.osaka-u.ac.jp/

The University of Osaka

Doctoral Dissertation

A Study on the Dynamic Nonprehensile Manipulation of Deformable Objects

Ixchel Georgina Ramirez Alpizar

January 2013

Graduate School of Engineering
Osaka University

工甲 16405

Doctoral Dissertation

A Study on the Dynamic Nonprehensile Manipulation of Deformable Objects

Ixchel Georgina Ramirez Alpizar

January 2013

Graduate School of Engineering

Osaka University

Abstract

The manipulation of an object made by a robot can be generally classified into two main types: grasping manipulation and nonprehensile (graspless) manipulation. The former makes use of fingers to grasp or pick the object with dexterity and precision; while the latter uses a plate or a probe and manipulates the object without grasping it. The nonprehensile manipulation scheme is discussed in this work, which aims to develop a manipulation strategy to rotate a deformable object effectively on a plate and estimate the object's physical parameters. A novel idea in this work is to aggressively utilize the object's dynamic deformation generated by high-speed vibrations of a simple flat plate. Such deformation of the object can drastically contribute to produce a fast and stable rotation. At first, for theoretical and simulation analyses, a viscoelastic multi-nodal model is introduced to represent the dynamic behavior of a deformable object. Then, it is shown how to experimentally obtain the model parameters of a real object. Through simulation analysis, it was discovered that the object's rotational behavior changes with respect to the plate's motion frequency in a way that is similar to a biped transitioning from a sliding to a walking and to a running gait. Also, the optimal plate motion and the optimal friction coefficient leading to the object's maximal angular velocity are obtained. The first one depends on the angular acceleration of the plate and is achieved with a running gait, while the second one depends on the type of gait-like behavior of the object. Next, it is explored how to estimate the physical parameters of a deformable object by a nonprehensile approach. In the proposed manipulation scheme, the object's high frequency in bending vibration is converted to a low-frequency rotating motion as a result of the friction effect together with the object's gait-like behavior. This suggests that the information of two physical parameters of the object: the natural bending frequency and the friction between the object and the plate is included in the object's rotational velocity. Based on this idea, the transition of the object's rotational velocity is characterized by a Lorentzian distribution function. Then, the correlations of the Lorentz function parameters with the object's physical parameters are revealed. Using these correlations, an estimation method of these parameters by only observing the object's rotational velocity is proposed. Simulation and experimental results are shown to verify the validity of the proposed method.

Acknowledgments

First, I want to express my most sincere and deep appreciation to my supervisor Associate Professor Mitsuru Higashimori, for accepting me as a doctoral course student and for his always enthusiastic supervision, encouragement and support through the realization of this work, with which I learned a lot and at the same time enjoyed my research.

To Professor Makoto Kaneko, Professor Koichi Osuka and Professor Keisuke Morishima for accepting and taking the time to review this dissertation, and for their invaluable comments and discussions that enriched this work, my deepest appreciation.

I would like to express my gratitude to the Monbukagakusho Scholarship Program of the Ministry of Science, Culture, Sports, Science and Technology (Monbukagakusho) for providing me the financial support for my studies in Japan.

To Assistant Professor Kenjiro Tadakuma for his cheering and support through my stay at Kaneko-Higashimori Laboratory, thank you very much. To Dr. Dylan Tsai, postdoctoral fellow of Kaneko-Higashimori Laboratory, thanks for the cheers and the chats we had. My deepest gratitude to my lab-mate Mr. Tomoyuki Inahara, for all his kind support and help during these 3 years, always taking the trouble of helping me. To my lab-mate Mr. Masaru Shamoto for taking the time and all the trouble of helping me with the experimental system when it broke down, thank you very much. A special thanks to my lab-mates Mr. Wataru Fukui and Mr. Yosuke Kimura for taking the time to talk with me and help me with my Japanese, I enjoyed the little chats we had.

To my parents Claudia and Eduardo, for their guidance and support without which I wouldn't be here, thank you so much. To my aunt Hilda, thank you for all your help, advice and support through these years. To all my family, specially to my brother Yail, his wife Marisela and my cousin Martha, thank you for all your support and the time we spent talking that kept me close to home. To my fiancé Shin, for all your patience, support and cheering during the hard times, thank you so much.

Contents

List of Figures xi

List of Tables xv

Nomenclature xvii

1 Introduction 1

1.1 Background and Motivation 1

1.2 Objective 3

1.3 Dissertation Outline 4

1.4 Related Works 5

1.4.1 Nonprehensile Manipulation 5

1.4.2 Dynamic Manipulation 8

1.4.3 Manipulation of Deformable Objects 9

2 Manipulation Scheme 13

2.1 Introduction 13

2.2 Robot System for Nonprehensile Manipulation 13

2.2.1 Design Guideline 14

2.2.2 Experimental System 16

2.3 Principle for Rotating an Object 18

2.4 Basic Experiment 21

2.5 Summary 25

3 Modeling 27

3.1 Introduction 27

3.2 Simulation Model 27

3.2.1 Assumptions 27
3.2.2 Deformable Object Model 28
3.2.3 Contact Model 29
3.3 Parameter Estimation 30
3.3.1 How to Estimate Parameters 30
3.3.2 Experimental Parameter Estimation 32
3.4 Summary 34

4 Optimal Manipulation for Rotating a Deformable Object 37
4.1 Introduction 37
4.2 Settings 37
4.3 Analogy to Bipedal Gaits 39
4.4 Optimal Plate Motion 41
4.5 Optimal Friction Coefficient 45
4.6 Summary 47

5 Estimating Physical Parameters of an Object 49
5.1 Introduction 49
5.2 Nonprehensile Approach to Estimate Physical Parameters of an Object 50
5.3 Characterization of the Object's Angular Velocity 51
5.3.1 Object's Angular Velocity Transition 51
5.3.2 Curve Fitting Using the Lorentz Distribution Function 52
5.4 Estimation of the Object's Natural Angular Frequency in Bending . . . 56
5.5 Estimation of the Friction between the Object and the Plate 59
5.6 Validation of the Proposed Method 63
5.6.1 Simulation Results 63
5.6.2 Experimental Results 70
5.7 Discussion 73
5.8 Summary 75

6 Conclusion 77
6.1 Conclusion 77
6.2 Future Work 79

Appendix A Coefficients of Determination 81

Appendix B t **Statistic Test** **83**

References **87**

Achievements **97**

List of Figures

1.1 Types of manipulation depending on the end-effector utilized. 2
1.2 Classification of robotic manipulation. 3

2.1 Dynamic nonprehensile manipulation for rotating an object. 14
2.2 Conceptual image of the robot system. 15
2.3 Overview of the experimental system. 17
2.4 Experimental system of the robot manipulator. 17
2.5 Model of the plate-object system for analysis. 18
2.6 Rotation mechanism. 20
2.7 Rotational motion of a rigid object for $A_p = 16$ deg. 22
2.8 Rotational motion of a deformable object for $A_p = 16$ deg. 22
2.9 Rotational motion of a deformable object for $A_p = 24$ deg. 24
2.10 Rotational angle of the object ${}^m\theta_B$ with respect to time for a plate amplitude $A_p = 16$ deg. 24
2.11 Angular velocity of the object with respect to the plate amplitude A_p. . 25
2.12 Bending motions of the deformable object during rotational motion for four rotational amplitudes of the plate. 25

3.1 Analytical model of the plate-object system. 28
3.2 Deformable object model. 29
3.3 Three-DOFs joint unit. 29
3.4 Contact model between the plate and the object. 30
3.5 Parameter estimation model. 30
3.6 Snapshots of the experiment to estimate the viscoelasticity parameters in bending. 33

3.7 Angle ϕ_2 with respect to time during the estimation of the viscoelasticity in bending. 33

3.8 Snapshot of the experiment to estimate the viscoelasticity parameters in compression. 34

3.9 Displacement s and contact force f_s with respect to time during the estimation of the viscoelasticity in compression. 35

4.1 Slice of cheese used in experiments in (a) and the simulation model in (b). 38

4.2 Snapshots of the experiment using $\omega_p/\omega_n = 2.4$. 39

4.3 Snapshots of the simulation using $\omega_p/\omega_n = 2.4$. 40

4.4 Angular velocity of the object ω_B with respect to the angular frequency of the plate ω_p/ω_n. 41

4.5 Analogy to bipedal gaits. 42

4.6 Relationship between the plate's rotational amplitude A_p, the plate's angular frequency normalized by the first-order natural frequency of the object in bending ω_p/ω_n, and the angular velocity of the object ω_B with $B_p = 3$ mm. 43

4.7 Relationship between the plate's rotational amplitude A_p, the plate's angular acceleration $A_p\omega_p^2$, and the angular velocity of the object ω_B with $B_p = 3$ mm. 44

4.8 Relationship between the friction angle between the plate and the object α, the angular acceleration of the plate $A_p\omega_p^2$, and the angular velocity of the object ω_B with $A_p = 3$ deg, $B_p = 3$ mm and $\omega_n = 10\pi$ rad/s in (a), and the top view of (a) with ω_B normalized by its maximal value and represented with contour lines in (b). 46

5.1 The object's angular velocity ω_B that corresponds to a low rotation frequency f_B in (a) is the result of the combination of the object's high natural angular frequency in bending w_n in (b) and the friction angle α between the plate and the object in (c). 50

5.2 Relationship between the object's angular velocity ω_B and the plate's motion frequency f_p with respect to (a) the plate's angular amplitude A_p for $\omega_n = 10\pi$ rad/s, and (b) the object's first-order natural frequency in bending ω_n for $A_p = 3$ deg. Both (a) and (b) with $B_p = 3$ mm and $\alpha = 36.9$ deg. 52
5.3 Lorentz distribution for three different values of λ and $x_0 = 0$. 53
5.4 Relationship between the object's angular velocity ω_B and the plate's motion frequency f_p, for (a) $\omega_n = 10\pi$ rad/s, $\alpha = 36.9$ deg, (b) $\omega_n = 33\pi$ rad/s, $\alpha = 36.9$ deg, and (c) $\omega_n = 10\pi$ rad/s, $\alpha = 56.3$ deg. 55
5.5 Relationship between the object's angular velocity ω_B and the plate's motion frequency f_p, for different friction angles α and different deformable objects for (a) $A_p = 3$ deg and (b) $A_p = 12$ deg, with $B_p = 3$ mm. 57
5.6 Relationship between the object's first-order natural angular frequency in bending ω_n and the parameter $\omega_{Br\,\max}$ obtained from the nonlinear regression of f_p vs. ω_B, for (a) $A_p = 3$ deg and (b) $A_p = 12$ deg, with $B_p = 3$ mm. 58
5.7 Relationship between the object's first-order natural angular frequency in bending ω_n and the parameter f_0 obtained from the nonlinear regression of f_p vs. ω_B, for (a) $A_p = 3$ deg and (b) $A_p = 12$ deg, with $B_p = 3$ mm. 59
5.8 Relationship between the friction angle α and the half width at half maximal b obtained from the nonlinear regression of f_p vs. ω_B, for (a) $A_p = 3$ deg and (b) $A_p = 12$ deg. 60
5.9 Relationship between the half width at half maximal b divided by the frequency of resonance f_0 and the friction angle α obtained from the nonlinear regression of f_p vs. ω_B, for (a) $A_p = 3$ deg and (b) $A_p = 12$ deg. 61
5.10 Relationship between the half width at half maximal b divided by the frequency of resonance f_0 and the ratio γ expressing the damping coefficients as $c_c = \eta c_{c_0}$ and $c_b = \eta c_{b_0}$, for four different ω_n and $A_p = 3$ deg. 63
5.11 Linear regression between the object's real ω_n and the estimated one $\hat{\omega}_n$. Simulation results for $A_p = 3$ deg in (a) and simulation and experimental results for $A_p = 12$ deg in (b). 68

5.12 Linear regression between the real friction angle α and the estimated one $\hat{\alpha}$. Simulation results for $A_p = 3$ deg in (a) and simulation and experimental results for $A_p = 12$ deg in (b). 69
5.13 Pictures of the deformable objects used in experiment. 71
5.14 Relationship between the object's angular velocity ω_B and the plate's motion frequency f_p, for three deformable objects in experiment, with $A_p = 12$ deg and $B_p = 3$ mm. 72
5.15 Comparison between rotational frequency and bending frequency of the object. 74

6.1 Future applications. 80

List of Tables

4.1 Parameters of the object in experiment and simulation. 38

5.1 Parameters estimated for $\omega_n = 3.5\pi$ rad/s and $A_p = 3$ deg. 64
5.2 Parameters estimated for $\omega_n = 10\pi$ rad/s and $A_p = 3$ deg. 65
5.3 Parameters estimated for $\omega_n = 23\pi$ rad/s and $A_p = 3$ deg. 65
5.4 Parameters estimated for $\omega_n = 33\pi$ rad/s and $A_p = 3$ deg. 65
5.5 Parameters estimated for $\omega_n = 1.4\pi$ rad/s and $A_p = 12$ deg. 66
5.6 Parameters estimated for $\omega_n = 3.5\pi$ rad/s and $A_p = 12$ deg. 66
5.7 Parameters estimated for $\omega_n = 6.5\pi$ rad/s and $A_p = 12$ deg. 66
5.8 Parameters estimated for $\omega_n = 10\pi$ rad/s and $A_p = 12$ deg. 67
5.9 Object's first-order natural frequency in bending and its rotation frequency. 74

A.1 Coefficients of determination for $A_p = 3$ deg. 81
A.2 Coefficients of determination for $A_p = 12$ deg. 82

B.1 Regression Analysis Parameters. 85
B.2 Calculated values of t and its associated p. 85

Nomenclature

$\boldsymbol{x}_1$	Displacement vector of the plate
$\boldsymbol{n}_1$	Inertial load vector
m_p	Mass of the plate
I_x	Moment of inertia around the X_1-axis
I_y	Moment of inertia around the Y_1-axis
I_z	Moment of inertia around the Z_1-axis
L	Distance between the center of mass of the plate and the handling position
X	Translational motion of the plate along the horizontal axis
Θ	Rotational motion of the plate around the horizontal axis
μ	Coefficient of friction without distinction between static and dynamic friction
Σ_R	Reference coordinate system
Σ_m	Coordinate system fixed at the plate
Σ_B	Coordinate system fixed at the center of mass of the object
${}^m x_B$	Position of Σ_B in the x axis, with respect to Σ_m
${}^m y_B$	Position of Σ_B in the y axis, with respect to Σ_m
${}^m \theta_B$	Orientation of Σ_B with respect to Σ_m
${}^R x_B$	Position of Σ_B in the x axis, with respect to Σ_R

NOMENCLATURE

${}^{R}y_B$	Position of Σ_B in the y axis, with respect to Σ_R
${}^{R}\theta_B$	Orientation of Σ_B with respect to Σ_R
m_B	Mass of the object
A_B	Contact area between the object and the plate
ξ	Axis that passes through the center of mass of the object and runs parallel with the x_m-axis
g	Gravitational acceleration constant
dA	Small area of the object
${}^{m}x_r, {}^{m}y_r$	Position of an arbitrary point of the object
$p({}^{m}y_r)$	Pressure applied to dA around $({}^{m}x_r, {}^{m}y_r)$
n	Rotational moment around the center of mass of the object
n_+	Moment contributing to the rotation of the object
n_-	Moment breaking the rotation of the object
A_p	Angular amplitude of the plate motion
μ_s	Static coefficient of friction
μ_k	Dynamic coefficient of friction
l	Length of the virtual tile link of the deformable object model
m	Mass of each node of the deformable object model
k_b	Elasticity of the bending joint in the deformable object model
c_b	Viscosity of the bending joint in the deformable object model
k_c	Elasticity of the compression joint in the deformable object model
c_c	Viscosity of the compression joint in the deformable object model
f_i^{contact}	Contact force applied to the i-th node in the contact model

a_i	Distance between the surface of the plate and the surface of the i-th virtual link in the contact model
k_{contact}	Elasticity of the contact model
c_{contact}	Viscosity of the contact model
f_i^{friction}	Frictional force applied to the i-th node in the contact model
v_i^{slip}	Slip velocity of the i-th node with respect to the plate, in the contact model
V	Friction transition velocity in the contact model
ϕ_1	Deformation angle of link 1 in the estimation model for the bending parameters
ϕ_2	Deformation angle of link 2 in the estimation model for the bending parameters
t_i	Time at the i-th sample in experiment
N	Total number of data samples in experiment
$\hat{k}_b$	Estimated elasticity of the bending joint unit in the deformable object model
$\hat{c}_b$	Estimated viscosity of the bending joint unit in the deformable object model
d	Thickness of the deformable object
s	Displacement caused by the applied force in the estimation model for the compression parameters
k_s	Elasticity of the estimation model for the compression parameters
c_s	Viscosity of the estimation model for the compression parameters
f_s	Contact force applied to the surface of the estimation model for the compression parameters
$\hat{k}_s$	Estimated elasticity of the estimation model for the compression parameters
$\hat{c}_s$	Estimated viscosity of the estimation model for the compression parameters

NOMENCLATURE

$\hat{k}_c$	Estimated elasticity of the compression joint unit in the deformable object model
$\hat{c}_c$	Estimated viscosity of the compression joint unit in the deformable object model
r	Radius of the real deformable object
M	Mass of the real deformable object
B_p	Linear amplitude of the plate motion
ω_p	Angular frequency of the plate motion
f_p	Frequency of the plate motion
ω_B	Angular velocity of the deformable object
ω_n	First-order natural angular frequency in bending of the deformable object
$\omega_{B\,\max}$	Maximal angular velocity of the deformable object
α	Friction angle between the plate and the object
κ	Ratio between the object's angular velocity and its maximal value $\omega_B/\omega_{B\,\max}$
β	Ratio between the dynamic and the static coefficients of friction μ_k/μ_s
f_B	Object's frequency of rotation on the plate
f_n	First-order natural bending frequency of the deformable object
$\omega_{Br\,\max}$	Maximal amplitude of the object's angular velocity at $f_p = f_0$
f_0	Frequency of resonance at which $\omega_B = \omega_{Br\,\max}$
b	Half width at half maximal of the Lorentzian curve
$\hat{\omega}_n$	Estimated first-order natural angular frequency in bending of the object
η	Scaling factor of the damping coefficients estimated for a slice of cheese
$\hat{\alpha}$	Estimated friction angle between the object and the plate

Chapter 1

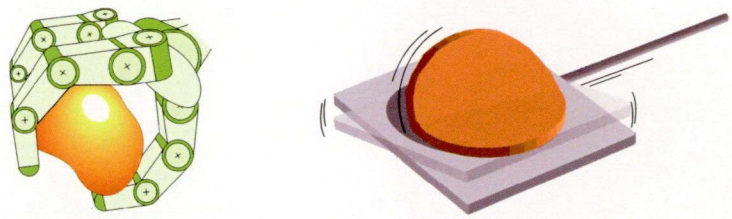
Introduction

1.1 Background and Motivation

The word manipulation derived from the verb manipulate comes from the Latin word *manipulus*, which is the diminutive of *manus* meaning hand, therefore manipulation means literally an action made by or using the hands. In robotics, there is a wide variety of manipulation schemes that can be broadly classified depending on the type of end-effector or hand into two major types: grasping manipulation and nonprehensile or graspless manipulation, as shown in Fig. 1.1. Grasping manipulation makes use of fingers to grasp or pick the object with dexterity and precision, using a gripper or an anthropomorphic robot hand to carry out pick and place tasks, as shown in Fig. 1.1(a). Nonprehensile manipulation uses a plate or a probe and manipulates the object without grasping it[1–48], as shown in Fig. 1.1(b).

Robotic manipulation can also be classified depending on the resting or moving state of the object to be manipulated into two types: static/quasi-static manipulation and dynamic manipulation. Static manipulation copes with objects at rest and discusses stable grasping of many kinds of objects, pick and place tasks, etc. In contrast, dynamic manipulation deals with objects in motion, using mainly high-speed robots to achieve tasks such as catching, juggling, and dribbling of balls[49–57].

Besides these two classifications in robotic manipulation, the works done in this area can be further classified depending on the type of object they deal with: manipulation of rigid bodies and manipulation of deformable objects[58–91]. The manipulation of rigid bodies being the most common since it is convenient from the point view of both



(a) Grasping/picking type by hand/gripper

(b) Nonprehensile type by plate/probe

Figure 1.1: Types of manipulation depending on the end-effector utilized, in (a) grasping type and in (b) nonprehensile type.

dynamic and geometric analyses. All of these different classifications are illustrated in Fig. 1.2.

The nonprehensile manipulation scheme has attracted many researchers in the past two decades, which have mainly focused on the manipulation of rigid objects or particles on vibrating plates aimed for practical uses in factories as parts feeders, sorters, etc[2–7,12–16,19,30,35,37–43]. However, for manipulating deformable objects, most of the works utilize the grasp manipulation approach to handle the object that is typically consider to be a linear object e.g. ropes, wires, cords, etc[58,59,62–68,71–76,78–82,84,88]. As far as we know, there are no works discussing the manipulation of deformable objects by a nonprehensile approach.

Let us consider which are the advantages of a nonprehensile manipulation scheme when handling deformable objects, over a grasp manipulation one. Since the object is not grasped, one advantage is the reduction of the stress concentration on the object, therefore the object's destruction can be avoided. This is a very important point, particularly when dealing with delicate objects. Another advantage is that it can remotely manipulate objects by using a simple plate, therefore allowing the robot to operate the object in areas with high temperatures, high humidity, electromagnetic fields, etc, where a gripper or a robot hand with precision devices or electrical hardware is not available or where humans can be in danger. Considering these advantages, this dissertation intends to develop a dynamic nonprehensile manipulation strategy to handle a deformable object on a flat rigid plate, as shown in Fig. 1.1(b). This is classified as illustrated in Fig. 1.2. What does actually happen when a deformable object is placed on a high-speed plate? Is there any effective strategy to manipulate the object and which is? The goal of this dissertation is to answer these questions. It

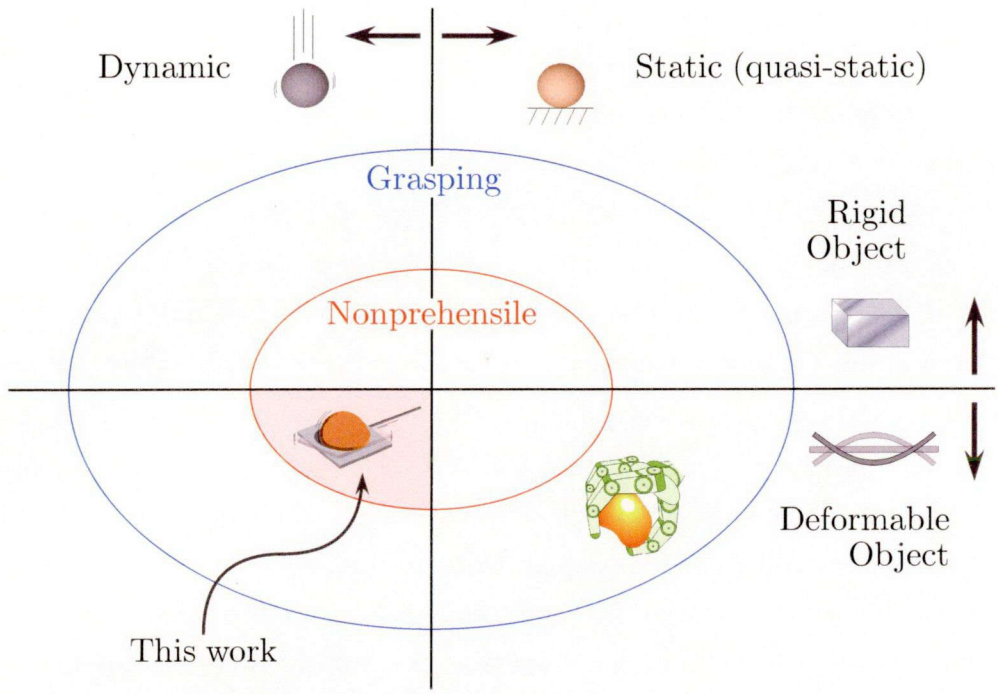


Figure 1.2: Classification of robotic manipulation by the type of end-effector employed into: grasping and nonprehensile; by the type of object into: rigid and deformable; and by the state of motion of the object into: dynamic and static(quasi-static).

is expected that the outcome of this research can remarkably contribute to the food industry automation and speed up of its processes. Also, as this manipulation scheme can prevent a large concentration of stress, it is expected to significantly contribute to the cell/tissue processing technology in the bioscience research.

1.2 Objective

The aim of this work is to develop a dynamic nonprehensile manipulation strategy to manipulate a thin deformable object by actively using its dynamic behavior caused by high-speed motions of a rigid flat plate. This dissertation reveals what actually happens in the manipulation for rotating deformable objects. It also explores the optimal conditions for the plate to achieve an effective rotating motion of the object. Finally, it proposes an estimation method for two physical parameters of the object by characterizing the transition of the object's rotational velocity on the plate.

1.3 Dissertation Outline

This dissertation is organized as follows.

In chapter 2, the design guideline of the robot manipulator with a plate as an end-effector, used in this dissertation is given. Then, after explaining why we used in particular a two-DOFs plate, the experimental system utilized is described. Next, the essence of the principle of rotating an object on the plate is explained. Finally, some basic experiments are shown to demonstrate that in fact a deformable object can rotate faster than a rigid one.

In chapter 3, a simulation model for a deformable object is introduced to approximate the dynamic behavior of the object on the plate. This model is composed of mass nodes connected by viscoelastic joint units. Each viscoelastic joint unit has three DOFs: bending, tension/compression and torsion, where the first two DOFs have viscoelastic elements and the third one is left free. It is explained how to experimentally estimate the parameters of the model for a real deformable object, and the result of estimating these parameters is shown.

In chapter 4, the optimal problem to produce the fastest object's rotation is solved. Simulation analysis based on real food is utilized and it is shown that the simulation results qualitatively correspond with the experimental ones, validating the model introduced. Then, it is shown that the behavior of the deformable object on the plate mimics either a sliding, walking or a running gait of a biped. The optimal plate motion leading to the maximal angular velocity of the object is obtained and it is revealed that the most dominant factor for a dynamically stable and fast object's rotation is the angular acceleration of the plate. Finally, it is shown that the optimal friction coefficient exists and it depends on the type of gait-like behavior of the object.

In chapter 5, the estimation of physical parameters of an object is discussed. It is shown that the line shape of the object's angular velocity with respect to the plate's motion frequency has a resonance-like behavior. Based on this nature, it is demonstrated that it can be represented with a simple mathematical expression like the Lorentz distribution one. Then it is shown that two physical parameters: the object's first natural angular frequency in bending and the friction between the object and the plate, dominate the Lorentzian curve characteristics. Using this relationship, an estimation

method for these two physical parameters is proposed. Finally, the simulation and experimental results of estimating these parameters are shown.

In Chapter 6, the conclusions and future works of this dissertation are given.

1.4 Related Works

In this section, we give a review of the closest works to this dissertation. We classify this works in three areas: nonprehensile manipulation, dynamic manipulation and manipulation of deformable objects, which are the main areas involved in this dissertation.

1.4.1 Nonprehensile Manipulation

In this manipulation scheme, the robot-system can compensate for its lack of degrees of freedom (DOFs) and sensors when using a simple end-effector, by utilizing dynamic effects produced by high-speed robot motions and by using an appropriate manipulation strategy[1–48].

Arai *et al.* discussed a manipulation strategy where a cube is rotated around its edge on a flat plate attached at the tip of a six-DOFs manipulator, and the rotation of the object is controlled[1]. Böhringer *et al.* developed a model for the mechanics of microactuators together with a sensorless parallel manipulation theory[2] and they also analyzed the dynamics involved to predict the behavior of the objects on a vibrating plate[3]. They proposed microassembly of parts using ultrasonic vibration and electrostatic forces to position and align parts in parallel on a vibratory table[4]. They also discussed algorithms for sensorless positioning and orienting of planar parts using different vibration patterns to generate force fields[5]. Zumel and Erdmann have discussed the nonprehensile orientation of planar objects by two palms joined at a central hinge and presented a method for planning part orientation[6]. They also showed how to reorient a part from an unknown initial state, and treated sliding and rolling contacts[7]. Lynch and Mason presented a one-DOF arm with a single revolute joint that perform tasks such as snatching an object from a table, rolling an object on the surface of an arm, and throwing and catching it, these were accomplished by finding (planning) trajectories to move the object[8,9]. They also discussed controllability, motion planning, and implementation of planar dynamic nonprehensile manipulation[11]. Lynch *et al.* examined the juggling skill called "Butterfly", where a ball is transported

along the inside and the outside of a palm surface, and discussed the shape of the robot palm and motion planning[10]. Reznik and Canny presented a simple feeder design in which parts are in permanent contact with a horizontally-vibrating flat plate, they called each plate vibration a "pump-like" motion[12]. They also developed the Universal Planar Manipulator (UPM) based on a single horizontally-vibrating plate with three DOFs and demonstrated that multiple objects were simultaneously moved toward target directions[13–15]. Using this UPM, Reznik *et al.* generated a special plate vibration that creates an average force field that they called "jet", they used it to move a single object enabling full parallel manipulation[16]. Erdmann discussed the manipulation of an object with two robots with flat palms attached to each of their wrist. Different manipulations were developed which include holding the object, rotating the object and slipping one palm on the other against the surface of the object[17]. Mason made a review in nonprehensile manipulation and its potential future work[18]. Šafarič *et al.* presented a programmable and position closed-loop controllable pneumatic active surface device, and showed the position and orientation control of rigid objects such as VLSI chips and MEMS and of flexible objects such as PVC polyvinyl foil and paper[19]. Amagai *et al.* showed the experiments where an object is manipulated on a plate attached at the tip of a six-DOFs manipulator based on visual information[20]. Huang and Holden discussed a nonprehensile manipulation using a mobile robot equipped with low-DOF palm manipulators. They showed how to pick up a box from a specific place by using the developed motion planner[21]. Maeda *et al.* presented a planning method for graspless manipulation by multiple robot fingers. A rigid object is moved to a goal position by tumbling and sliding operations and discussed the stability of the object[22,23]. They also discussed how to automatically determine which kind of control mode (position and force control) is best for the robot fingers to manipulate an object[24]. Based on this, they considered the motion planning of the robot fingers[25,26] and investigated the robustness of the graspless manipulation[27]. Tabata and Aiyama discussed tossing manipulation by a one-DOF manipulator that swings its arm to roll/slide an object on it, and then tosses it to a desire position[28]. They also discussed what they called passing manipulation which consist in one manipulator tossing an object and another one catching the tossed object without impact[29]. Frei presented a vibratory conveyor consisting of a flat rigid plate with three translational DOFs that is capable of moving

objects in two dimensions[30]. Gupta and Huang discussed a carrying task by two mobile robots equipped with a flat palm with two DOFs, they developed an algorithm to maintain the contact with the object at a nominal position on the palms so the robots do not drop the object[31]. Hara *et al.* proposed an estimation method of the position and velocity of a crystal sphere on a flat disk that is supported by three robot fingers with three DOFs, each of the fingers has a three-directional force sensor placed at its tip. Based on force information only, they successfully controlled the sphere on the disk[32] and analyzed the stability of their controller[33]. Maneewarn and Detudom presented a nonprehensile manipulation done by multiple robots that pull an object along a desired path using a rope[34]. Mitani *et al.* examined a saw-toothed feeder surface for a unidirectional feeding of microparts. They analyzed the influence of the driving forces, the point contacts and the angle of the saw-toothed surface[35]. Akbarimajd *et al.* discussed a manipulation method by an array of one-DOF arms based on backward throws where a polygonal object is manipulated to a goal configuration by a sequence of juggles[36]. Vose *et al.* examined how to create force and velocity fields by a plate rotating about an axis below the plate[37]. They also discussed sensorless control methods for point parts sliding on a rigid plate by estimating the programmable velocity fields for point parts, and showed basic experiments by using a six-DOFs vibrating plate[38]. They demonstrated that translation and rotation of a rigid plate induces parts on the plate to move toward or away from a nodal line aligned with the rotational axis[39]; and how to find frictional velocity fields generated by plate motions[40]. They also showed that the trajectory of a rigid part sliding on a rigid vibrated plate can be described by a first-order system[41]. Umbanhowar and Lynch discussed a vibratory part transport mechanism that uses both static and dynamic frictions to linearly transport parts in a horizontal direction[42]. Umbanhowar *et al.* examined the role of anisotropic friction properties in vibratory parts manipulation and showed experimental results that quantify the anisotropic friction effects on the generation of asymptotic velocity fields on a rigid vibrating plate[43]. Mori *et al.* developed a one-DOF planer manipulator that throws a disk in a frictionless plane, controlling the translational velocity, angular velocity and direction of the disk[44]. Mettin *et al.* and Bätz *et al.* examined a ball dribbling task by proposing a manipulator equipped with a spring that gets compressed when the ball bounces against it and presented a planning motion for this modified dribbling

motion[45,46]. Bätz *et al.* discussed the nonprehensile catching of a ball using an industrial robot with six revolute joints and a force/torque sensor at the end-effector, which is a circular plate. They achieved the nonprehensile ball catching based on visual and force/torque sensor information[47]. Ryu *et al.* presented a stabilization control of a nonprehensile rolling manipulation system that they called the disk-on-disk. An upper disk (target object) is free to roll on to the lower disk (hand or end-effector) under the influence of gravity[48].

Most of these works done on manipulation utilizing a simple end-effector have supposed that the object is a particle(s) or a rigid body(ies) since it is convenient from the viewpoint of both geometric and dynamic analyses.

1.4.2 Dynamic Manipulation

The increasingly rapid evolution of technology has allowed the development of dynamic skills in robots, making possible human-like tasks which include quick motions and continuous movements[49–57].

Namiki *et al.* and Imai *et al.* developed a high-speed robotic hand with eight joints and three fingers that can close its joints at 180 deg per 0.1 s[49]. They also developed a hand control system to catch a falling ball and a falling cylinder using feedback from a high-speed vision system[50]. Kaneko *et al.* discussed the design of a high-speed capturing robot and show through experiments that its maximal acceleration is 91G with a capturing time of 25 ms[51]. Higashi *et al.* designed the 100G capturing robot from the viewpoint of dynamic pre-shaping, they discussed how to determine the mechanical parameters to successfully catch a ball[52]. Furukawa *et al.* discussed a strategy for the dynamic re-grasp of an object by throwing it up and then catching it. They divide the re-grasp task into throwing strategy and catching strategy using a high-speed vision system to compute the position and orientation of the object[53]. Higashi *et al.* proposed a dynamic capturing strategy for a 2-D stick-shaped object that has both translational and rotational velocities, the object is on an air table and captured by two robotic fingers that stopped the object completely[54]. Haddadin *et al.* showed a cyclic ball dribbling task achieved with a seven-DOFs articulated anthropomorphic robot equipped with an elastic compliant hand. They used only force sensing, without any visual information[55]. Bätz *et al.* presented a control structure to equip humanoid robots with dynamic skills, they achieved ball dribbling and catching tasks using an

anthropomorphic dual-arm robot with 14 DOFs[56]. Kizaki and Namiki achieved a two-ball juggling task using a single high-speed hand-arm with seven DOFs and three general purpose fingers. One ball is tossed by a commercially available toss machine and the other is thrown by the hand-arm, a stereo vision system is used to calculate the ball trajectories to catch the balls and continue with the juggling task. They showed experimental results where the robot hand-arm achieved the juggling of two balls five times[57].

All of these works discussed the manipulation of an object in motion, this type of manipulation is called dynamic manipulation, it typically deals with rigid objects and in most of the cases a robot hand is used as the end-effector.

1.4.3 Manipulation of Deformable Objects

For the manipulation of deformable objects there is an important consideration to be made in comparison with the manipulation of rigid objects, which is the deformation of the object that can be permanent or momentary. Conventional works treating a deformable object have generally supposed two or more fingers for grasping and handling the object[58–91].

Wakamatsu *et al.* analyzed stable grasping of deformable objects and formulated the deformation of linear objects e.g. ropes, wires, cords, etc[58]. Sun *et al.* discussed the handling of a general flexible object by two manipulators, they showed that the object achieves the desired position/orientation[59]. Howard and Bekey modeled a 3D deformable object and calculated its deformation characteristics to learn the required forces needed to grasp the object[60,61]. Henrich *et al.* investigated the handling of non-rigid one-dimensional objects by a robot manipulation system. They analyzed stable point contacts and possible contact states of a one-dimensional object with polyhedral obstacles[62] and Remde *et al.* additionally discussed the transitions between contact states and its conditions[63]. Yue and Henrich presented different adjustment-motions that eliminate vibration of deformable linear objects when handled by robot manipulators[64]. They also discussed fast manipulation using a force/torque sensor mounted on the robot's wrist to recognize the vibrational phase of the deformable linear object[65]. Schlechter and Henrich analyzed oscillations that occur while handling deformable linear objects and presented a method for active open-loop damping[66]. Acker and Henrich investigated a formulation for assembly or disassembly tasks based on contact states for

the handling of deformable linear objects in a polyhedral environment[67]. Fukuda *et al.* discussed the manipulation of a flexible object by a dual manipulator system, they tied a cylinder object with a rope based on vision and force information[68]. Hirai *et al.* presented a robust control law for the grasping manipulation of deformable objects using three 2-DOFs fingers and a real-time vision system. They showed that translation, rotation and deformation of a planar sponge made of polyester can be achieved with the control law they proposed[69]. Foresti and Pellegrino developed a vision-based system that is able to automatically recognize deformable objects to estimate their position/orientation and select suitable picking points for the robot arm[70]. Hashimoto *et al.* proposed a rigid body link model of a string as an example of deformable object to manipulate it dynamically by a robot manipulator. They showed experimental results of flinging-up motion of a string as an example of dynamic manipulation[71]. Wakamatsu *et al.* presented a planning method for linear object manipulation such as knotting and raveling using only a single six-DOFs manipulator and a CCD camera. They showed experiments where a linear object made of rubber is placed on a table, its shape is captured by the camera to generate a plan for knotting or unknotting[1] the object[72] and for tightly tying the object[73]. They also classified the unraveling process into crossing state transitions and planned the manipulation process based on the initial crossing state of the object[74,75]. Wakamatsu *et al.* additionally introduced a criteria for evaluating the manipulation plans to reduce its number[76]. Garg and Dutta analyzed the internal force requirements when grasping and manipulating deformable objects by a three finger robot. They clarified that the required internal force varies depending on the size of the object and the finger contact angle with the object[77]. Matsuno *et al.* proposed an algorithm for shape recognition of a rope and conducted an experiment of knotting a rope using a dual manipulator system. Their algorithm is used to evaluate if the rope is deformed or not[78,79]. Saha and Isto developed a motion planner for manipulating deformable linear objects using two cooperating robot arms. The planner is able to tie self-knots and knots around simple static objects[80]. Yamakawa *et al.* proposed a strategy for making knots with a single high-speed multifingered robot hand equipped with tactile sensors, which are used in the sensor based control[81]. They also

[1]The term "unknotting" is used by Wakamatsu *et al.* to refer to the inverse process of knotting. It does not refer to the unknot in the mathematical theory of knots, which is defined as a closed loop that is not knotted[92].

proposed the dynamic knotting of a flexible rope by a single high-speed robot arm, a model for the linear flexible object was derived and used for the motion planning of the robot arm[82]. They additionally considered the dynamic folding of a cloth by two high-speed multifingered hands mounted on two sliders and using a high-speed vision system for feedback to the control system. They extended their model for linear objects to a sheet-like flexible object model and used it for the motion planning of the robot hands[83]. They also analyzed the mechanics of a flexible rope and demonstrated deformation control of the rope[84]. Kita *et al.* proposed a strategy for a dual-arm robot to pick up a specific part of a cloth with one hand while holding it with its other hand, using a trinocular stereo vision system[85]. Shibata *et al.* discussed the wiping motion of a deformable object by a robotic hand with two grippers, each of which can move independently in both vertical and horizontal directions therefore allowing the robot hand to pinch and wrinkle the deformable object to achieve the wiping motion[86]. Bersch *et al.* presented a fully autonomous system capable of transforming a T-shirt from a random configuration into a folded state. The robot used has two 7-DOFs arms that have two-finger parallel jaw grippers mounted on its rotating wrists, it also has stereo cameras mounted on its head and mono-cameras mounted on its forearms along with pressure sensor arrays in each gripper's fingertips[87]. Vinh *et al.* proposed a new strategy for knotting a deformable rope. A seven-DOFs manipulator arm was taught to tie a knot by using a Wii remote controller as a teaching pennant[88]. Cretu *et al.* discussed the design and implementation of a framework that automatically extracts and monitors the shape of deformations of soft objects using a video sequence and mapping them with force measurements with the aim of providing the necessary information to a three-finger robotic hand controller in order to manipulate deformable objects[89]. Khalil and Payeur made a review on robotic manipulation of deformable objects that uses vision, force and tactile information as feedback into their systems[90]. Jimenez made a survey on manipulation planning of deformable objects that use a model of the deformable object to achieve tasks like path planning, folding/unfolding, topology modifications, and assembly[91].

As far as we know, there are no works dealing with a deformable object as the main target in nonprehensile manipulation.

Chapter 2

Manipulation Scheme

2.1 Introduction

A typical nonprehensile manipulation scheme consists of a vibrating plate placed close to the necessary sensors and actuators to generate the desired motions/vibrations in order to manipulate the targeted object(s). However, this type of design has space and environmental limitations. Instead, we consider a design where the robot can remotely manipulate the object as shown in Fig. 2.1(a). Also, most of the works done in nonprehensile manipulation have supposed that the object is rigid or a particle. On the contrary, we will deal with the dynamic nonprehensile manipulation of a deformable object, as shown in Fig. 2.1(b). In this chapter, the details of the robot design and the experimental system constructed are given in section 2.2. Next, the principle for manipulating an object, especially for rotating it on a rigid plate, is explained in section 2.3. Finally, in section 2.4 basic experiments with both rigid and deformable objects are shown and compared.

2.2 Robot System for Nonprehensile Manipulation

In this section we describe the manipulation scheme used in this dissertation, and explain why we chose it. Then we show the experimental system constructed to achieve this manipulation.

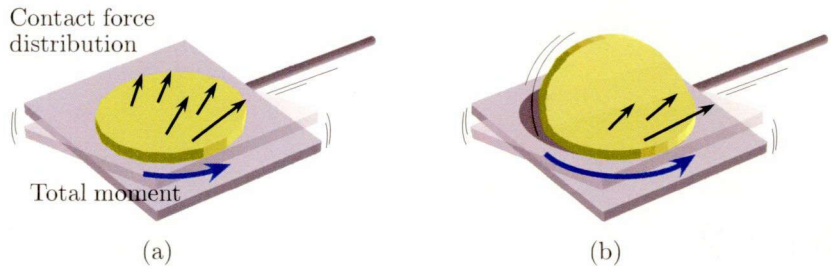


Figure 2.1: Dynamic nonprehensile manipulation for rotating: (a) a rigid body and (b) a deformable body. The object's deformation generated by dynamic effects as shown in (b), can decrease the negative moment. As a result, the object can rotate faster.

2.2.1 Design Guideline

A typical nonprehensile manipulation scheme consists of a vibrating plate placed close to the necessary sensors and actuators to generate the desired motions/vibrations, as previously introduced in section 1.4.1. This type of design has space and environmental limitations, since the plate itself has underneath mechanical and electronic/electrical devices that may not work adequately depending on climate conditions, etc. Instead, we consider a design where the robot can remotely manipulate the object even in areas where electrical hardware and electronic precision instruments cannot approach. To achieve this, we choose a simple flat plate as end-effector, handled by a long bar which is driven by actuators, as shown in Fig. 2.2(c), where a supporter is placed to compensate for the gravitational effect. In this case, we no longer have the hardware restriction of implementing a complex actuation/transmission mechanism near the plate, and we can design and choose the robot mechanism freely. Here, an important point is to appropriately choose the arrangement of DOFs of the plate for the reduction of the inertial load towards the feasibility of high-speed motions. Let us discuss which DOFs are suitable to achieve these high-speed motions. Fig. 2.2(a) shows a plate and its six DOFs around its center of mass at the handling position, under no gravitational effects. Let the displacement vector of the plate and the inertial load vector applied to the handling position be expressed by $\boldsymbol{x}_1 \triangleq [X_1, Y_1, Z_1, \Theta_{X1}, \Theta_{Y1}, \Theta_{Z1}]^T$ and $\boldsymbol{n}_1 \triangleq [m_p, m_p, m_p, I_X, I_Y, I_Z]^T$, respectively; where m_p, I_x, I_y, and I_z express the mass, the moments of inertia around the X_1-axis, the Y_1-axis, and the Z_1-axis, respectively. Next, suppose the handling position is located at a distance L, far from the center of mass by using a bar with a negligible small mass, as shown in Fig. 2.2(b). In this case, the inertial load vector

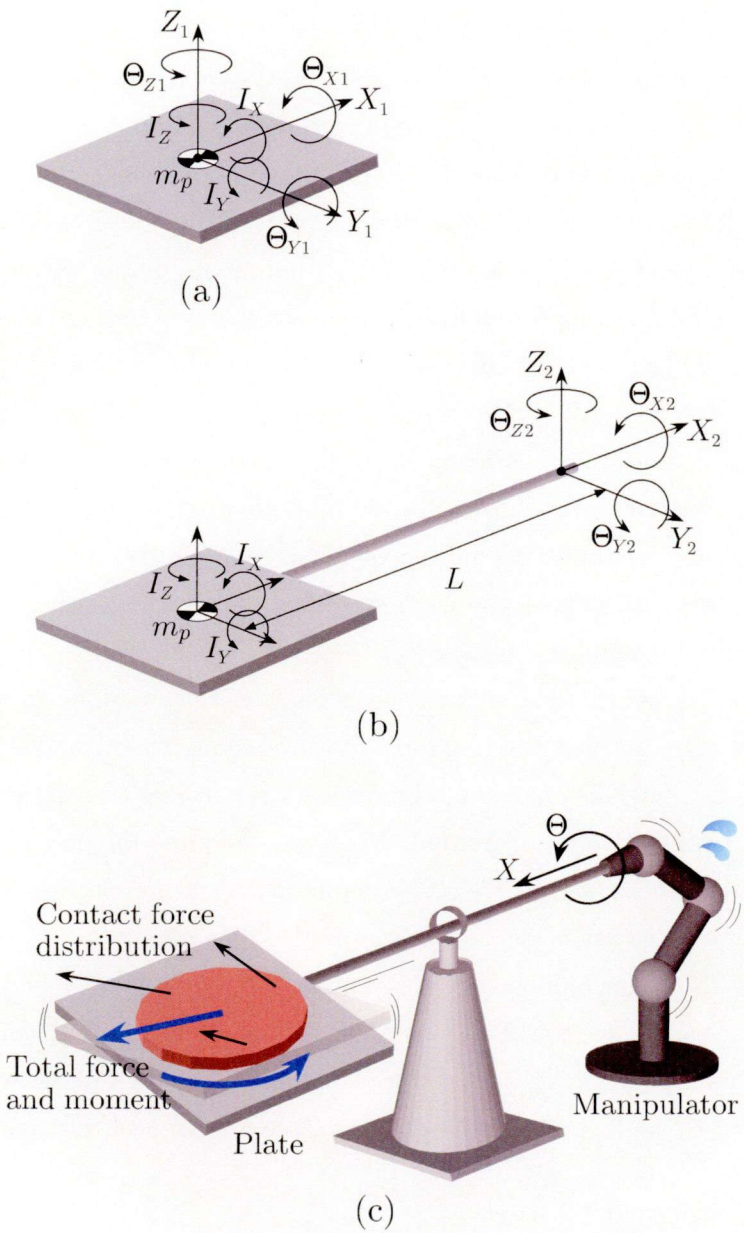


Figure 2.2: Conceptual image of the robot system. Six DOFs of the plate and its inertial loads are shown, where the handling position is located on the center of mass of the plate in (a) and on the bar with a distance L in (b). The same inertial loads are applied to the handling position in (b) independently of the distance L, as long as we choose two DOFs (X_2, Θ_{X2}) to generate the plate motions. This arrangement of DOFs works effectively to produce quick plate motions through the long bar, from the viewpoint of low inertial loads applied to actuators as shown in (c).

is given by $\boldsymbol{n}_2 \triangleq [m_p, m_p, m_p, I_X, I_Y + m_pL^2, I_Z + m_pL^2]^T$ with respect to the displacement vector of $\boldsymbol{x}_2 \triangleq [X_2, Y_2, Z_2, \Theta_{X2}, \Theta_{Y2}, \Theta_{Z2}]^T$. From this relationship, we can confirm that the same inertial loads are applied to the handling position independently of the distance L, as long as we choose two DOFs (X_2, Θ_{X2}) to generate the plate motions[93]. Therefore, the arrangement of DOFs (X, Θ) in Fig. 2.2(c) is effective from the viewpoint of the reduction of loads applied to actuators and important for the robot to generate quick plate motions through the long bar for manipulating both position and orientation of an object on the plate.

As illustrated in Fig. 2.2(c), the manipulation strategy for controlling the position and orientation of objects, has already been discussed by Higashimori *et al.*[93]. The object moves backward or forward in the parallel direction to the bar by giving only a linear acceleration to the plate motion of X, as this plate's acceleration generates an inertial force that overcomes the frictional force between the object and the plate. Also, when we give an angular displacement to Θ, the object moves in the perpendicular direction to the bar, as this angular displacement generates a slope in the plate thus moving the object by the gravitational force that overcomes the frictional force between the object and the plate. These two mechanisms for generating translational motions of the object can be intuitively understood. However, the most important feature of the nonprehensile scheme showed in Fig. 2.2(c) is its ability to remotely rotate the object keeping its center of rotation located on the plate. This manipulation for rotating an object is achieved by the combination of the plate accelerations of $\ddot{X}$ and $\ddot{\Theta}$; a detailed explanation is given in section 2.3. Based on the above discussion, this dissertation focuses on the manipulation strategy for rotating an object on a plate, where dynamic effects generated by high-speed motions of the plate are aggressively utilized.

2.2.2 Experimental System

Fig. 2.3 shows an overview of the experimental system. A plate attached at the tip of a manipulator generates translational and rotational motions of an object, and a vision system observes the object on the plate. Fig. 2.4 shows the manipulator and the object. The manipulator possesses three active joints and one free joint (or passive joint), where an AC servo motor for driving each joint is implemented at each active joint. A plate is fixed at the tip of a bar that moves along the longitudinal axis of it (translational DOF: X) by the rotations of the 1st and the 2nd joints. The plate rotates

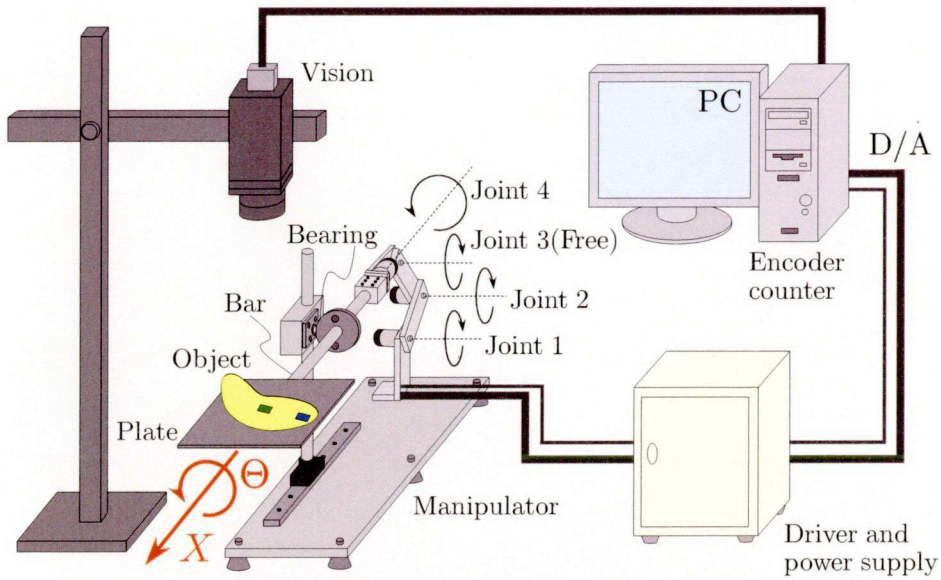


Figure 2.3: Overview of the experimental system.

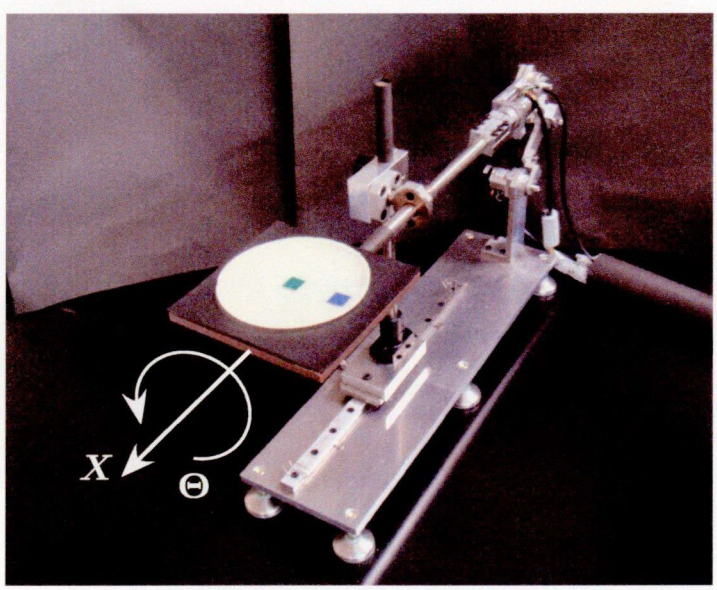


Figure 2.4: Experimental system of the robot manipulator.

around the longitudinal axis of the bar (rotational DOF: Θ) by the rotation of the 4th joint. Here we would like to emphasize that although the plate has actually three DOFs, only two DOFs: X and Θ, as shown in Fig. 2.4 are utilized in the experiments. The plate measures 100 mm $\times$ 100 mm, and the position and the orientation of the plate

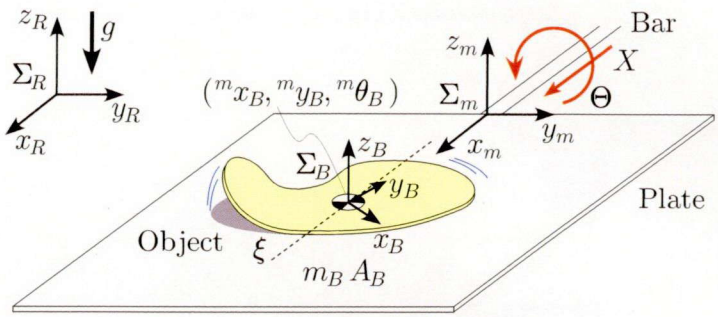


Figure 2.5: Model of the plate-object system for analysis.

(X and Θ) are measured by the encoders integrated in the motors. The gravitational load applied to the joints is supported by a bearing holding up the bar. Additionally, since we are considering a remote manipulation scheme that can be used in areas where electrical/electronic hardware is not available or cannot approach, we only use a vision system to measure the object's angular velocity, as the camera does not need to be close to the manipulation area. We intentionally attach to the object two rectangular shaped markers: one in the center of the object and the other on its perimeter to form a radial line, as shown in Fig. 2.4, so that the vision system can recognize both the position and the orientation of the object with a frame rate of 120 fps. However, the system can work without these markers.

2.3 Principle for Rotating an Object

Consider a plate and a deformable object as shown in Fig. 2.5. To simplify the analysis, we set the following assumptions:

1) The plate is rigid.
2) The object has a uniform mass distribution and a negligible thickness.
3) The plate is large enough not to drop the object.
4) The friction coefficient based on Coulomb's law between the plate and the object is uniform, and is given by μ, where static and dynamic frictions are not distinguished.

The meaning of the symbols in Fig. 2.5 is as follows:

Σ_R: Reference coordinate system. The x_R-y_R plane is horizontal.

Σ_m: Coordinate system fixed at the plate. The z_m-axis is perpendicular to the plate.

Σ_B: Coordinate system fixed at the center of mass of the object. The z_B-axis is perpendicular to the contact plane.

${}^m x_B, {}^m y_B$: Position of Σ_B with respect to Σ_m.

${}^m \theta_B$: Orientation of Σ_B with respect to Σ_m.

${}^R x_B, {}^R y_B$: Position of Σ_B with respect to Σ_R.

${}^R \theta_B$: Orientation of Σ_B with respect to Σ_R.

m_B: Mass of the object.

A_B: Contact area between the object and the plate.

ξ: Axis that passes through the center of mass of the object and runs parallel with the x_m-axis.

g: Gravitational acceleration.

As explained in the previous section, suppose that a plate is attached at the tip of a bar as shown in Fig. 2.5. Σ_m is fixed at the connecting point between the plate and the bar, where the x_m- and the z_m-axes coincide with the longitudinal direction of the bar and the perpendicular direction to the plate, respectively. X and Θ express the linear displacement along the x_m-axis and the rotational angle around the x_m-axis, respectively, where $\Theta = 0$ when the plate is horizontal.

Fig. 2.6 shows the top view and the side view of the object on the plate. The object as well as the plate are stationary ($X = 0$, $\Theta = 0$) in Fig. 2.6(a). As shown in Fig. 2.6(b), suppose that the object starts to slip and moves along the x_m-direction by the motion of the plate when $|\ddot{X}| > \mu g$. In this case, as the pressure distribution on the object is uniform, the frictional force distribution is also uniform, as shown in Fig. 2.6(b), where we simply draw the frictional distribution on the line segment that passes through the center of mass of the object and runs parallel with the y_m-axis. Let us now consider the case when the plate motion of $\ddot{\Theta}$ is added, as shown in Fig. 2.6(c). In this case, the pressure distribution on the object results in a slope by the inertial force generated by $\ddot{\Theta}$. The pressure applied to a small area dA around an arbitrary

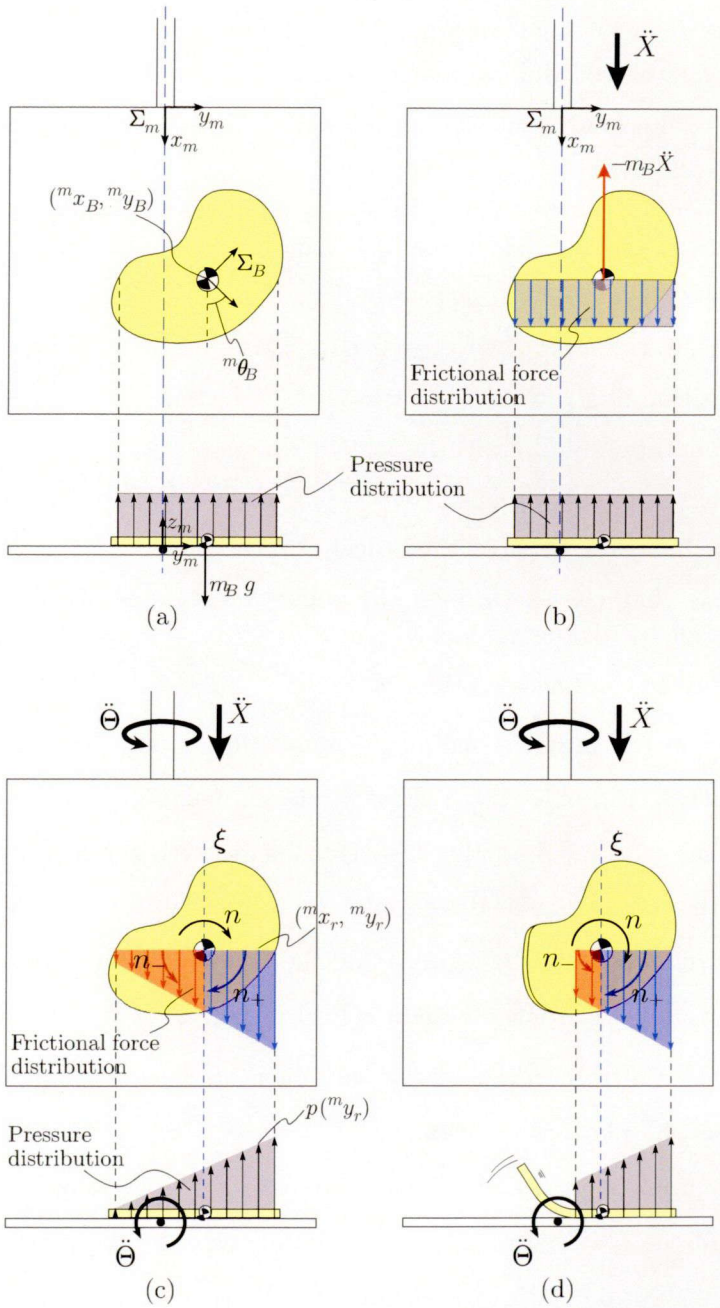


Figure 2.6: Rotation mechanism: (a) Both the plate and the object are stationary, i.e. no motion is given to the plate (b) Only a translational motion $\ddot{X}$ is given to the plate, (c) Both translational $\ddot{X}$ and rotational $\ddot{\Theta}$ motions are given to the plate, (d) Due to the object's deformation the contact area decreases.

point of the object denoted by $({}^m x_r, {}^m y_r)$ is given[94–97] by

$$p({}^m y_r) = \frac{m_B}{A_B}(g + {}^m y_r \ddot{\Theta}). \tag{2.1}$$

As shown in equation (2.1), the pressure distribution on the object is a function of ${}^m y_r$. From equation (2.1), the total moment applied around the center of mass of the object can be expressed by

$$n = -\frac{{}^m \dot{x}_B}{|{}^m \dot{x}_B|}\mu \int_{A_B} ({}^m y_r - {}^m y_B) \cdot p({}^m y_r) dA, \tag{2.2}$$

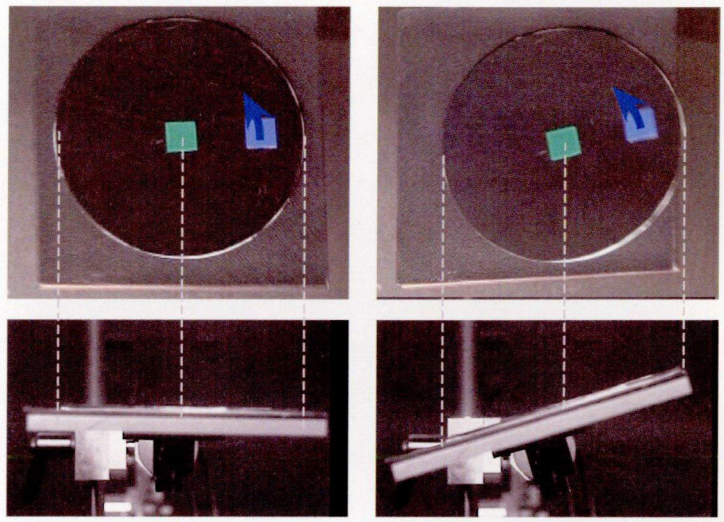
$$= -\frac{{}^m \dot{x}_B}{|{}^m \dot{x}_B|}\mu(g + {}^m y_B \ddot{\Theta}) \int_{m_B} ({}^m y_r - {}^m y_B) dm$$
$$-\frac{{}^m \dot{x}_B}{|{}^m \dot{x}_B|}\mu \ddot{\Theta} \int_{m_B} ({}^m y_r - {}^m y_B)^2 dm, \tag{2.3}$$

where $n > 0$ and $n < 0$ coincide with the moments of the clockwise and the counter clockwise directions, respectively. $\ddot{X}\ddot{\Theta} > 0$ and $\ddot{X}\ddot{\Theta} < 0$ generate the moments for the clockwise direction ($n > 0$) and for the counter clockwise one ($n < 0$), respectively[98].

We now consider the effect of the elasticity of a deformable object. Let us separate the moment of n into two parts by ξ-axis as shown in Fig. 2.6(c), where n_+ and n_- express the moments generated by the friction for the positive and the negative directions, respectively. This means $n = n_+ + n_-$. In this case, when the object has the enough elasticity to be deformed by the plate motion of $\ddot{\Theta}$, the non-contact area between the object and the plate can be generated as shown in Fig. 2.6(d). From this behavior of the deformable object, the negative moment n_- caused by friction decreases, as a result, the net moment n increases. Therefore, a deformable object can be expected to rotate faster than a rigid one, when both have the same shape, mass, and friction coefficient.

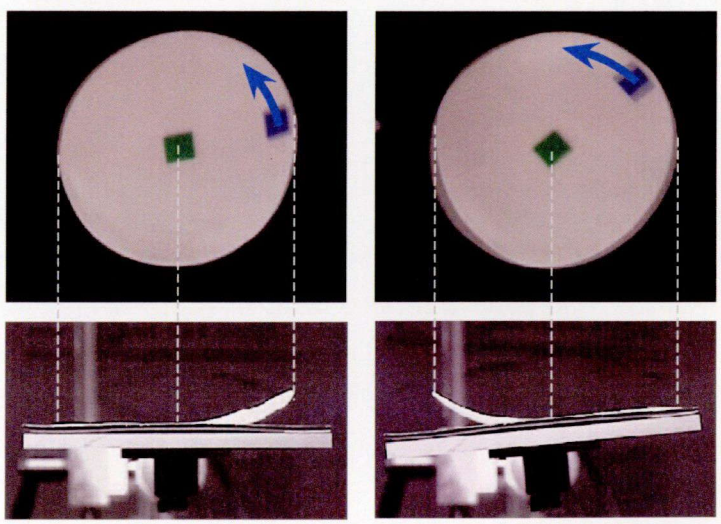
2.4 Basic Experiment

A small circular pancake is utilized as a deformable object. It has a mass of 10 g, a radius of 42 mm, and a thickness of 1.0 mm. Additionally, as a rigid body, we prepare another object made of plastic with the same physical properties except for the bending stiffness. We give to the plate's two DOFs of motion the sinusoidal trajectories given by $X(t) = 2\sin(14\pi t)$ mm and $\Theta(t) = -A_p \sin(14\pi t)$ deg. The object rotates continuously



(a) $t = 0.14$[s] (b) $t = 0.54$[s]

Figure 2.7: Rotational motion of a rigid object: the object is rotating with an angular velocity of 15.7 deg/s, for $A_p = 16$ deg.



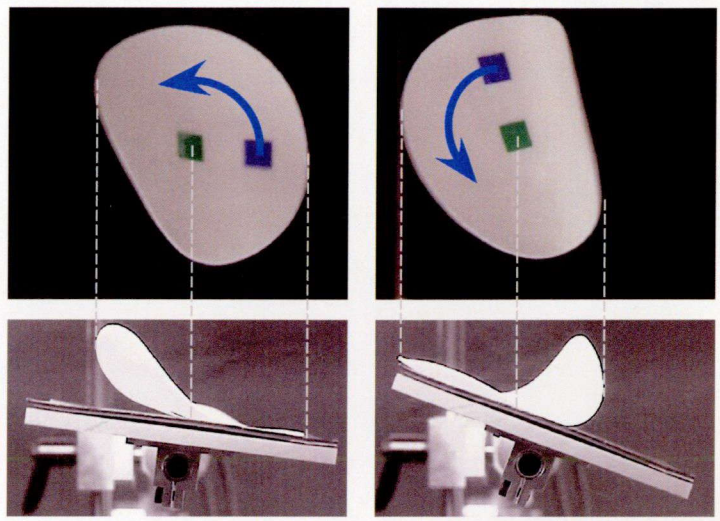
(a) $t = 0.14$[s] (b) $t = 0.52$[s]

Figure 2.8: Rotational motion of a deformable object: the object is rotating with an angular velocity of 56.6 deg/s, for $A_p = 16$ deg.

on the plate by cyclically changing the frictional force distribution. Fig. 2.7 shows a series of photos of the rigid object's rotational motion, where the amplitude of Θ is given by $A_p = 16$ deg. From Fig. 2.7, it can be seen that the object does not bend

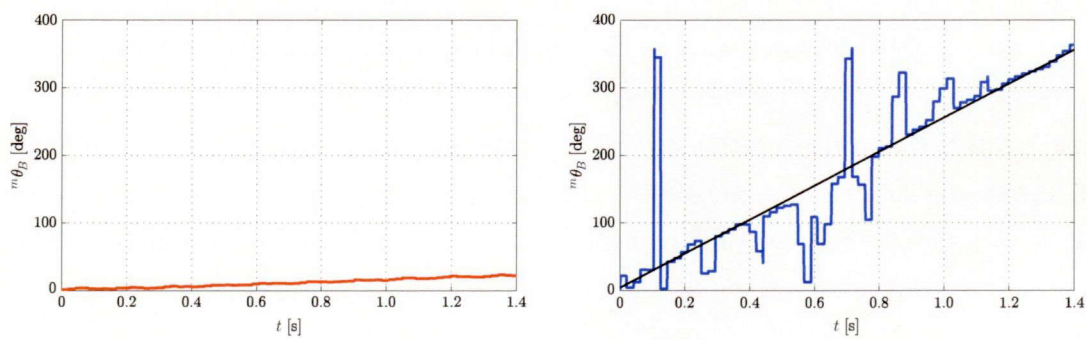
and full contact between the plate and the object is maintained. Here, the object rotates with an angular velocity of 15.7 deg/s, as shown in Fig. 2.10(a), where the rotational angle of the object with respect to time is plotted. Moreover, if we give an amplitude larger than $A_p = 16$ deg, the object becomes unstable and violently falls from the plate. On the contrary, Fig. 2.8 shows a series of photos of the deformable object's rotational motion, for the same plate's amplitude $A_p = 16$ deg. From Fig. 2.8, it can be seen that the object is bent by the inertial force given by the plate, thus the contact area between the plate and the object is decreased. This object's behavior works effectively for decreasing the braking moment, as explained in Fig. 2.6(d). As a result, the deformable object can rotate faster than the rigid one on the plate. The object rotates with an angular velocity of 56.6 deg/s, which is more than three times faster than the rigid object with the same plate motion. Additionally, Fig. 2.9 shows a series of photos of the deformable object's rotational motion, where the amplitude of Θ is given by $A_p = 24$ deg. From Fig. 2.9, it can be seen that the object is bent even more than in Fig. 2.8, reducing the contact area between the plate and the object to almost a half, decreasing even more the braking moment and thus rotating faster. In this case, the object rotates with an angular velocity of 251.7 deg/s, as shown in Fig. 2.10(b), where the rotational angle of the object with respect to time is plotted. Here, the marker placed on the object to measure its position and orientation is hidden by its own deformation at some periods of time, which causes the angle data to have noise. The straight line shown in Fig. 2.10(b) is the linear approximation of the angle data.

Fig. 2.11 shows the relationship between the plate's angular amplitude A_p and the angular velocity of the object for the rigid (○) and the deformable (□) objects of the previous experiments. The hatched areas represent the amplitudes at which the object cannot rotate stable and/or falls from the plate. As shown in Fig. 2.11 the angular velocity of the object increases as the plate amplitude increases, for both rigid and deformable objects. In particular, when the amplitude of the plate is $A_p > 10$ deg it can be seen that the angular velocity of the deformable object begins to increase drastically, while the angular velocity of the rigid object is almost the same as when $A_p < 10$ deg. Fig. 2.12(a)–(d) shows the bending motions of the deformable object during rotational motions for plate amplitudes of $A_p = 6$, $A_p = 16$, $A_p = 24$ and $A_p = 26$ deg, respectively. These amplitudes correspond to Fig. 2.11(a)–(d), in the



(a) $t = 0.21$[s] (b) $t = 0.61$[s]

Figure 2.9: Rotational motion of a deformable object: the object is rotating with an angular velocity of 251 deg/s, for $A_p = 24$ deg.



(a) Rigid object (b) Deformable object

Figure 2.10: Rotational angle of the object $^m\theta_B$ with respect to time for a plate amplitude $A_p = 16$ deg.

same order. In Fig. 2.12(a), (b), and (c) it can be seen that as the plate amplitude increases, the object's deformation becomes larger and as a result the contact area with the plate is decreased. As explained in section 2.3, this object's behavior contributes to the reduction of the torque braking the object's rotation. However, as seen in Fig. 2.12(d), the object becomes unstable, violently hoping on the plate and does not rotate when $A_p = 26$ deg.

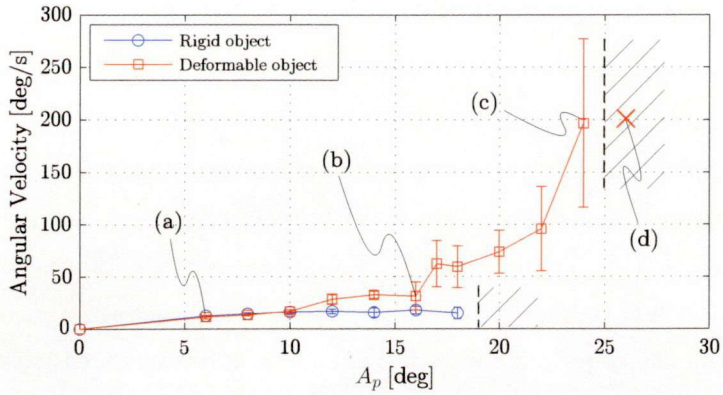
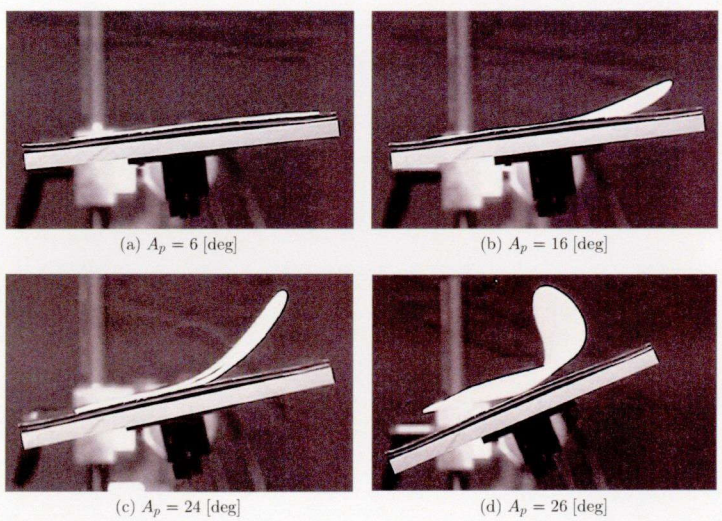


Figure 2.11: Angular velocity of the object with respect to the plate amplitude A_p.



(a) $A_p = 6$ [deg]

(b) $A_p = 16$ [deg]

(c) $A_p = 24$ [deg]

(d) $A_p = 26$ [deg]

Figure 2.12: Bending motions of the deformable object during rotational motion for four rotational amplitudes of the plate.

2.5 Summary

A typical nonprehensile scheme has space and environmental limitations since the actuators and sensors needed for manipulation are placed close to the end-effector. In contrast, the nonprehensile scheme used in this dissertation is remotely manipulated allowing us to utilize it with less space and less environmental limitations, as well as without increasing the inertial loads applied to the handling position when we use only two DOFs. The combination of these two DOFs: a translational motion X with a rotational motion Θ generates the rotational moment n which allows the object to ro-

tate on the plate. Additionally, when using a deformable object its dynamical behavior yields two advantages: the first is the reduction of the moment breaking rotation thus enabling the deformable object to rotate faster than a rigid one, and the second is a more stable contact with the plate due to the softness of the deformable object. The experiments shown, demonstrated that a deformable object can actually rotate faster than a rigid one, under the same plate's motion conditions. It was also shown that as the plate amplitude increases the deformable object's deformation became larger, therefore enabling the object to rotate faster since the contact area with the plate was decreased, for a plate amplitude of $0 \leq A_p \leq 24$ deg. The result discussed in this chapter is the starting point for investigating which parameters dominate the dynamic behavior of the object and how we should actively utilize them towards the optimal manipulation.

Chapter 3

Modeling

3.1 Introduction

In preparation for the motion analysis, in this chapter the analytical model used in this dissertation to approximate the dynamic behavior of a thin deformable object on a plate, is introduced. Then, the experimental estimation of the model parameters for a real deformable object is shown. First, in section 3.2 the analytical model used for simulation analysis is introduced. In 3.2.1 the assumptions of the model are given. In 3.2.2 the viscoelastic model for a deformable object is introduced, and in 3.2.3 the contact model of the object with the plate is shown. Finally, in section 3.3 the experimental estimation of the analytical model parameters is shown.

3.2 Simulation Model

Fig. 3.1 shows the entire model used for simulation analysis. The model is approximating a circular shaped object on a rigid plate with two DOFs.

3.2.1 Assumptions

Consider a plate and a thin deformable object as shown in Fig. 2.1(b). To simplify the analysis, we set the following assumptions:

1) The plate is rigid.
2) The plate's surface area is larger than that of the object.
3) The object is deformable, and its thickness is small.

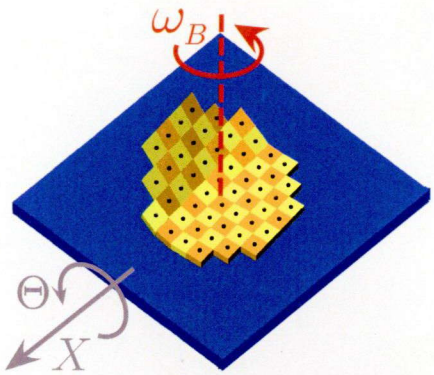


Figure 3.1: Analytical model of the plate-object system.

4) The object is isotropic, and it has uniform mass distribution and uniform viscoelasticity.
5) The nominal pressure distribution on the object is uniform.
6) The plate is large enough not to drop the object.
7) The friction coefficient between the plate and the object that is based on Coulomb's law is uniform and is given by μ_s and μ_k for static and dynamic coefficients, respectively.

3.2.2 Deformable Object Model

For a thin deformable object, we consider virtual tile links as shown in Fig. 3.2. The link is a square with sides of length l. Based on the shape and the size of the modeled object, the arrangement of virtual tiles is determined. A node with a mass of m is located at the center of the link, where adjacent nodes are connected to each other by a viscoelastic joint unit as shown in Fig. 3.3. The joint unit is composed of three DOFs: bending, compression/tension, and torsion, which are supposed to be sufficient to represent the behavior of the deformable object on the plate. The bending and the compression joints have viscoelastic elements that are given by a Kelvin–Voigt model, while the torsion joint is free for simplicity of the simulation model. In Fig. 3.3, k_b and c_b express the elasticity and viscosity, respectively, of the bending joint. Similarly, k_c and c_c are the elasticity and viscosity, respectively, of the compression joint.

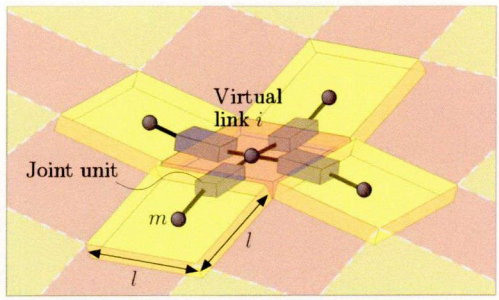


Figure 3.2: Deformable object model.

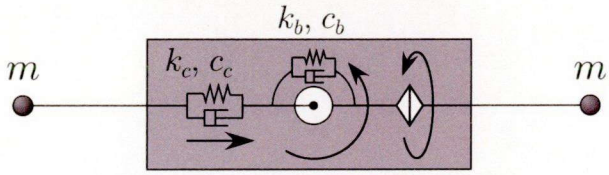


Figure 3.3: Three-DOFs joint unit.

3.2.3 Contact Model

Fig. 3.4 shows the contact model between the plate and the ith virtual link. The contact force is computed with the penalty method that is based on the Kelvin–Voigt model[99]. The contact force f_i^{contact} that is applied to the ith node is given by

$$f_i^{\text{contact}} = k_{\text{contact}} a_i^{2.2} + c_{\text{contact}} \dot{a}_i \quad (a_i \geq 0) \tag{3.1}$$

where a_i, k_{contact}, and c_{contact} are the distance between the surface of the plate and that of the virtual link, the elasticity, and the viscosity, respectively. Also, the frictional force f_i^{friction} that is applied to the ith node is given by,

$$f_i^{\text{friction}} = \mu_* f_i^{\text{contact}}. \tag{3.2}$$

The coefficient of friction in equation (3.2) is defined by

$$\mu_* = \begin{cases} 0 & \text{for} \quad v_i^{\text{slip}} = 0 \\ \mu_s & \text{for} \quad 0 < |v_i^{\text{slip}}| < V \\ \mu_k & \text{for} \quad V \leq |v_i^{\text{slip}}| \end{cases}$$

where v_i^{slip} is the slip velocity of the ith node with respect to the plate, and V is the friction transition velocity that determines the threshold between static and dynamic

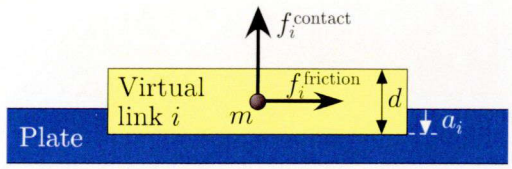


Figure 3.4: Contact model between the plate and the object.

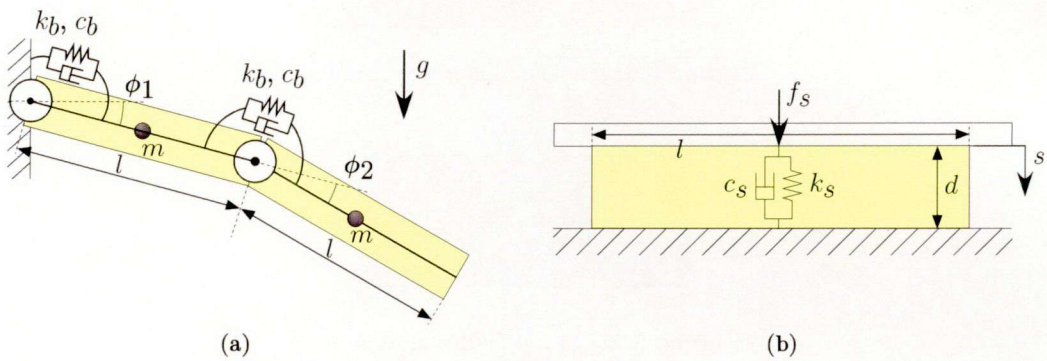


Figure 3.5: Parameter estimation model of the bending joint in (a), and of the compression joint in (b).

frictions. The frictional force f_i^{friction} is in the opposite direction to the slip velocity of the ith node with respect to the plate's surface.

3.3 Parameter Estimation

In this section we show how to estimate the parameters of a real object for the model explained in 3.2.2.

3.3.1 How to Estimate Parameters

Viscoelasticity in Bending: Fig. 3.5(a) shows the side view of the model that is utilized to estimate the viscoelasticity in bending. This model is composed of two links and two bending joints. One joint connects the left tip to the wall, and the other joint connects the two links, leaving the right tip free; thus, it is deformed by gravity. This deformation is approximated by two angles: ϕ_1 and ϕ_2, which denote the angle of the two bending joints, the one between the wall and the left tip of the model, and the one between the two links, respectively. The equation of motion of this model is expressed

as follows:

$$\begin{bmatrix} \dot{\phi}_2 & \phi_2 \end{bmatrix} \begin{bmatrix} c_b \\ k_b \end{bmatrix} = \frac{1}{2} mgl \cos(\phi_1 + \phi_2) - \frac{1}{4} ml^2 \ddot{\phi}_2 - \frac{1}{4} (1 + 2\cos\phi_2) ml^2 \ddot{\phi}_1 \ . \tag{3.3}$$

Using the sampling data in t_i $(i = 1, \ldots, N)$, equation (3.3) is expressed by

$$\boldsymbol{A}\boldsymbol{p}_b - \boldsymbol{q} = \boldsymbol{0} \tag{3.4}$$

where

$$\boldsymbol{A} \triangleq \begin{bmatrix} \dot{\phi}_2(t_1) & \phi_2(t_1) \\ \dot{\phi}_2(t_2) & \phi_2(t_2) \\ \vdots & \vdots \\ \dot{\phi}_2(t_N) & \phi_2(t_N) \end{bmatrix}$$

$$\boldsymbol{p}_b \triangleq \begin{bmatrix} c_b & k_b \end{bmatrix}^{\mathrm{T}}$$

$$\boldsymbol{q} \triangleq \begin{bmatrix} \frac{1}{2} mgl \cos(\phi_1(t_1) + \phi_2(t_1)) - \frac{1}{4} ml^2 \ddot{\phi}_2(t_1) - \frac{1}{4} (1 + 2\cos\phi_2(t_1)) ml^2 \ddot{\phi}_1(t_1) \\ \frac{1}{2} mgl \cos(\phi_1(t_2) + \phi_2(t_2)) - \frac{1}{4} ml^2 \ddot{\phi}_2(t_2) - \frac{1}{4} (1 + 2\cos\phi_2(t_2)) ml^2 \ddot{\phi}_1(t_2) \\ \vdots \\ \frac{1}{2} mgl \cos(\phi_1(t_N) + \phi_2(t_N)) - \frac{1}{4} ml^2 \ddot{\phi}_2(t_N) - \frac{1}{4} (1 + 2\cos\phi_2(t_N)) ml^2 \ddot{\phi}_1(t_N) \end{bmatrix}.$$

From the least-squares solution of equation (3.4), the viscoelastic parameters $\hat{\boldsymbol{p}}_b \triangleq [\hat{c}_b \ \hat{k}_b]^{\mathrm{T}}$ can be estimated by

$$\hat{\boldsymbol{p}}_b = (\boldsymbol{A}^{\mathrm{T}}\boldsymbol{A})^{-1}\boldsymbol{A}^{\mathrm{T}}\boldsymbol{q}. \tag{3.5}$$

Viscoelasticity in Compression: Fig. 3.5(b) shows the side view of the model that is utilized to estimate the viscoelasticity in compression, where one link with a small thickness d is put on a table. The deformation of the link is given by a displacement s, and the viscoelastic parameters in the Kelvin–Voigt model are k_s, and c_s. The contact force f_s that is applied to the upper surface with area l^2 and the displacement s are utilized in the force response equation which is expressed as follows:

$$\begin{bmatrix} \dot{s} & s \end{bmatrix} \begin{bmatrix} c_s \\ k_s \end{bmatrix} = f_s. \tag{3.6}$$

Using the sampling data in t_i $(i = 1, \ldots, N)$, equation (3.6) is expressed by

$$\boldsymbol{B}\boldsymbol{p}_s - \boldsymbol{f}_s = \boldsymbol{0} \tag{3.7}$$

where

$$\begin{aligned}
\boldsymbol{B} &\triangleq \begin{bmatrix} \dot{s}(t_1) & s(t_1) \\ \dot{s}(t_2) & s(t_2) \\ \vdots & \vdots \\ \dot{s}(t_N) & s(t_N) \end{bmatrix} \\
\boldsymbol{p}_s &\triangleq \begin{bmatrix} c_s & k_s \end{bmatrix}^{\mathrm{T}} \\
\boldsymbol{f}_s &\triangleq \begin{bmatrix} f_s(t_1) & \cdots & f_s(t_N) \end{bmatrix}^{\mathrm{T}}.
\end{aligned}$$

From the least-squares solution of equation (3.7), the viscoelastic parameters $\hat{\boldsymbol{p}}_s \triangleq [\hat{c}_s \ \hat{k}_s]^{\mathrm{T}}$ can be estimated by

$$\hat{\boldsymbol{p}}_s = (\boldsymbol{B}^{\mathrm{T}}\boldsymbol{B})^{-1}\boldsymbol{B}^{\mathrm{T}}\boldsymbol{f}_s. \tag{3.8}$$

Here, $\hat{\boldsymbol{p}}_s$ represents the viscoelasticity parameters over the upper surface (l^2). Since, in our model, we want to describe the viscoelasticity over the lateral surface of the link (ld), we convert $\hat{\boldsymbol{p}}_s$ to obtain $\hat{\boldsymbol{p}}_c \triangleq [\hat{c}_c \ \hat{k}_c]^{\mathrm{T}}$ as

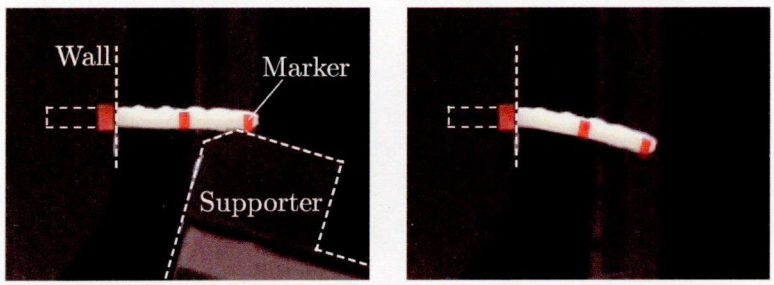
$$\hat{\boldsymbol{p}}_c = \hat{\boldsymbol{p}}_s \, (d/l)^2 \tag{3.9}$$

which expresses the scaled viscoelasticity for a contact force that is applied to the lateral surface of the link with area ld and thickness l, based on assumption 4 that the object is isotropic.

3.3.2 Experimental Parameter Estimation

As a real deformable object, a slice of cheese is employed in the experiment since it is an artificial product that can reasonably correspond to assumptions 4, 5, and 7. Based on the model shown in Fig. 3.2, each squared link has a length of $l = 10$ mm, thickness $d = 2.5$ mm, and mass $m = 0.285$ g.

To estimate the viscoelastic parameters in bending, a slice of cheese was cut to get the two link model shown in Fig. 3.5(a). Actually, its total length is 30 mm, and



(a) $t = 0.0$ [s] (b) $t = 0.20$ [s]

Figure 3.6: Snapshots of the experiment to estimate the viscoelasticity parameters in bending.

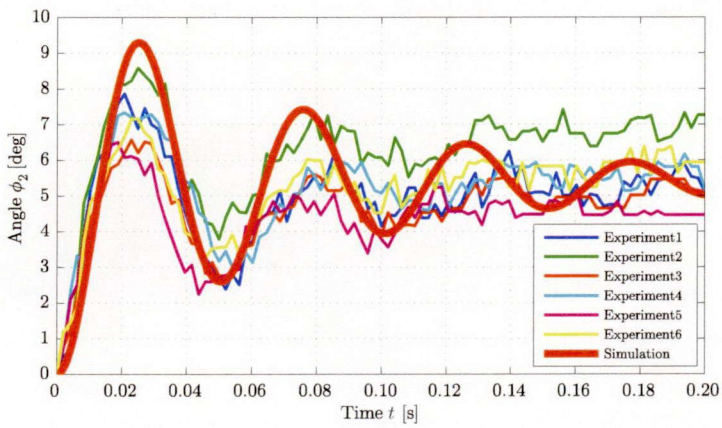


Figure 3.7: Angle ϕ_2 with respect to time during the estimation of the viscoelasticity in bending.

its width is 10 mm, as shown in Fig. 3.6(a), where the left 10 mm of the object was gripped at the wall portion. We placed three red markers: the first one at the wall boundary, the second one at the middle of the right 20 mm of the object, where the virtual joint is located, and the third one at the right tip of the object, which is left free. In the initial state, the cheese is supported as shown in Fig. 3.6(a), and then released to be deformed by gravity, as shown in Fig. 3.6(b). We obtain the joint's angles data $\phi_1(t_i)$ and $\phi_2(t_i)$ $(i = 1, \ldots, N)$ by measuring the markers' positions using vision with 480 frames per second. Fig. 3.7 shows the angle ϕ_2 with respect to time during the deformation by gravity. From these data and equation (3.5) with $N = 97$, the parameters $\hat{k}_b = 2.72 \times 10^{-3}$ N·mm/deg and $\hat{c}_b = 4.23 \times 10^{-6}$ N·mm/(deg/s) are obtained. In Fig. 3.7, the reconstructed result of ϕ_2 using the estimated parameters is

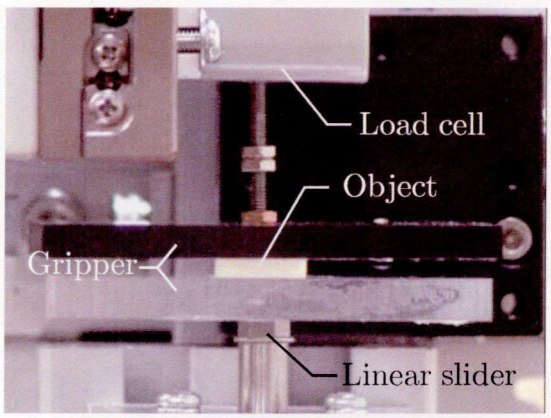


Figure 3.8: Snapshot of the experiment to estimate the viscoelasticity parameters in compression.

overlapped. From this figure, it can be seen that the reconstructed result is similar to the experimental ones.

To estimate the viscoelastic parameters in compression, a slice of cheese was cut to get the single-link model of length $l = 10$ mm, width $l = 10$ mm and thickness $d = 2.5$ mm, as shown in Fig. 3.5(b); as shown in Fig. 3.8 the object is compressed by a parallel jaw gripper that is actuated by a linear slider. The displacement data $s(t_i)$ are measured by a linear encoder that is implemented in the slider, and the contact force data $f_s(t_i)$ $(i = 1, \ldots, N)$ are measured by a load cell that is attached to the parallel jaw gripper. The force sensor sampling time is 1 kHz. Fig. 3.9 shows the displacement s and the contact force f_s with respect to time during the deformation by compression. From these data and equation (3.8) with $N = 10$, the parameters $\hat{k}_s = 12$ N/mm and $\hat{c}_s = 7.9 \times 10^{-3}$ N/(mm/s) are obtained. Then, $\hat{k}_c = 0.79$ N/mm and $\hat{c}_c = 4.9 \times 10^{-4}$ N/(mm/s) are obtained by the conversion that is based on equation (3.9) . In Fig. 3.9, the reconstructed result of f_s using the estimated parameters and the displacement in Experiment 1 is overlapped. From this figure, it can be seen that the experimental results and the reconstructed one are similar.

3.4 Summary

In this chapter, a simulation model for approximating the dynamic behavior of a thin deformable object on a plate was introduced. This model is composed of multiple mass

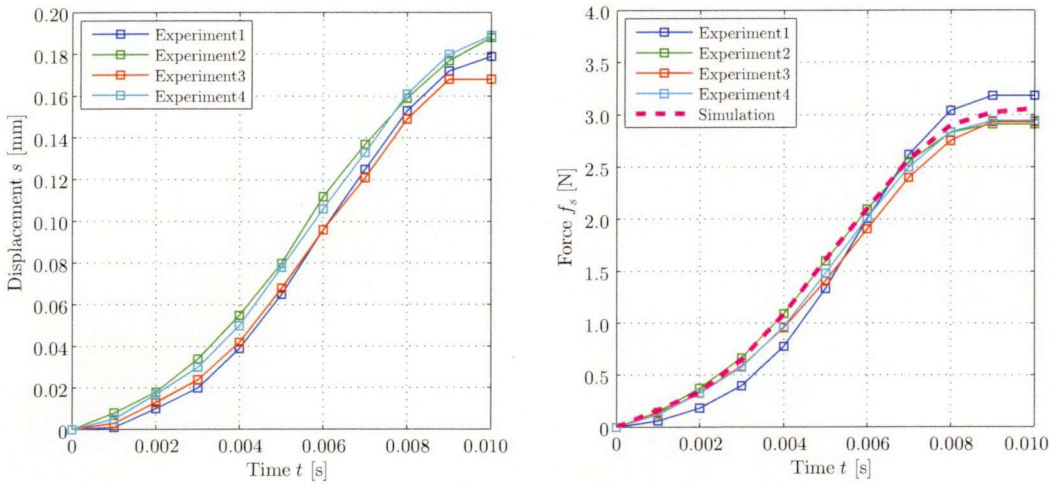


Figure 3.9: Displacement s and contact force f_s with respect to time during the estimation of the viscoelasticity in compression.

nodes and three-DOFs joint units with viscoelasticity elements. It was explained how to estimate the viscoelastic parameters of the introduced model. These parameters were estimated experimentally for a commercially available slice of cheese. The data reconstructed by simulation using the estimated parameters showed qualitatively correspondence with the experimental results, for the bending and the tension/compression parameters of the introduced model for simulation.

Chapter 4

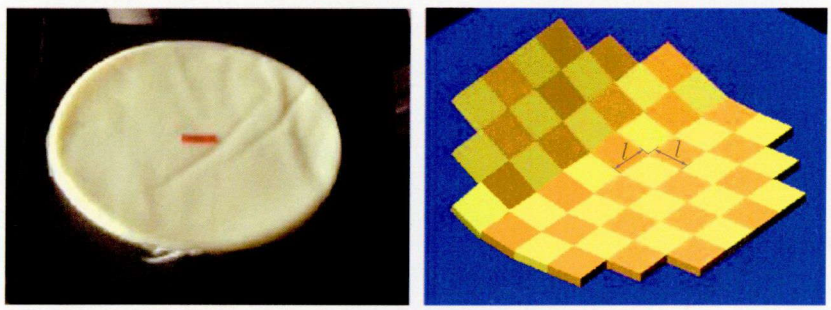
Optimal Manipulation for Rotating a Deformable Object

4.1 Introduction

In this chapter it is investigated how the object's rotational behavior and resultant rotational velocity change with respect to the plate's motion frequency by means of simulation analysis. In section 4.2 the simulation settings are given. Then, in section 4.3 simulation and experimental results of an object rotating on the plate shown qualitatively correspondence to each other, and the object's rotating behavior similarity with a biped's gait is explained. Finally, in sections 4.4 and 4.5 it is shown the existence of the optimal plate motion and the optimal friction coefficient leading to the object's maximal angular velocity, respectively.

4.2 Settings

A commercially available slice of cheese as shown in Fig. 4.1(a) is used as the base model for simulation analysis. The slice of cheese has a circular shape of radius $r = 40$ mm, thickness $d = 2.5$ mm, and mass $M = 13.6$ g. A circular shape was chosen, since its orientation do not influence the value of the moment of rotation generated, therefore a constant rotational velocity can be obtained. However, the manipulation scheme used in this dissertation can be utilized to rotate different shaped objects, in these cases the rotational velocity is not constant. The simulation software MD Adams (MSC.Software Corp.) is utilized to compute the dynamic motion of the object. The



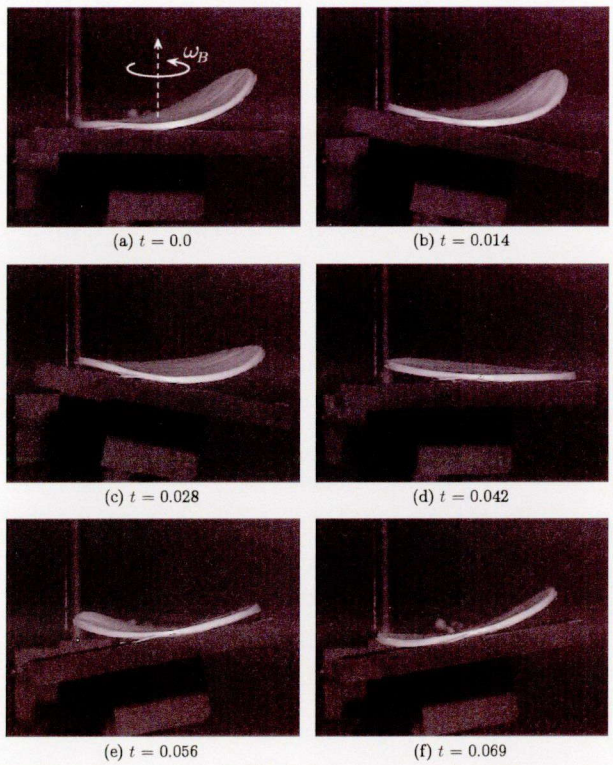
(a) (b)

Figure 4.1: Slice of cheese used in the experiments in (a) and the simulation model of a slice of cheese that is composed of 52 links with $l = 10$ mm in (b).

Table 4.1: Parameters of the object in experiment and simulation.

Cheese	M	13.6 g
	r	40 mm
	d	2.5 mm
Simulation model	m	2.62×10^{-1} g
	l	10 mm
	k_b	2.72×10^{-3} N·mm/deg
	c_b	4.23×10^{-6} N·mm/(deg/s)
	k_c	0.79 N/mm
	c_c	4.9×10^{-4} N/(mm/s)
	k_{contact}	11.86 N/mm
	c_{contact}	7.65×10^{-3} N/(mm/s)
	μ_s	0.75
	μ_k	0.40
	V	100 mm/s

simulation model as shown in Fig. 4.1(b) is composed of 52 links with $l = 10$ mm. The four viscoelastic parameters that were obtained in section 3.3 are utilized together with the friction's coefficients $\mu_s = 0.75$ and $\mu_k = 0.4$ obtained experimentally. Additionally, $k_{\text{contact}} = 11.86$ N/mm, $c_{\text{contact}} = 7.65 \times 10^{-3}$ N/(mm/s) and $V = 100$ mm/s are given empirically. The experiment and simulation parameters are summarized in Table 4.1. In order to rotate the object, we give to the plate's two DOFs of motion the following



(a) $t = 0.0$ (b) $t = 0.014$

(c) $t = 0.028$ (d) $t = 0.042$

(e) $t = 0.056$ (f) $t = 0.069$

Figure 4.2: Snapshots of the experiment using $\omega_p/\omega_n = 2.4$. The object is rotating on the plate with an angular velocity of $\omega_B = 370$ deg/s.

sinusoidal trajectories:

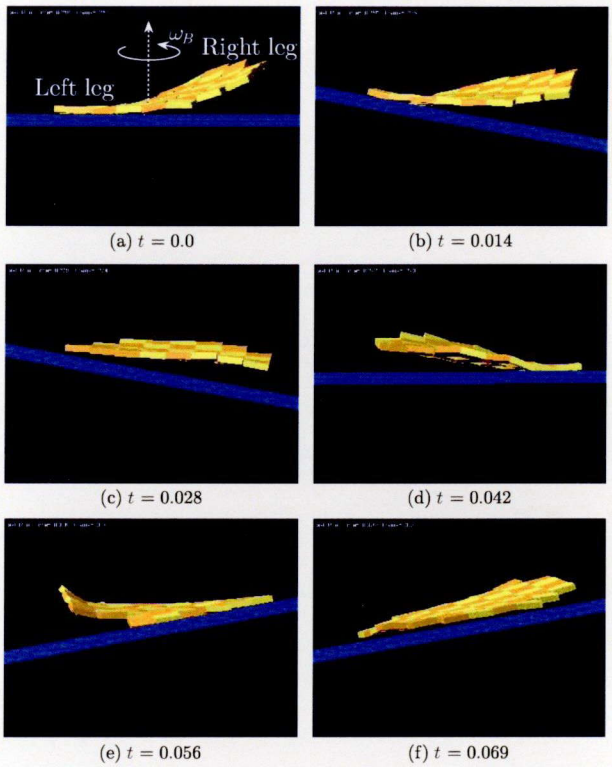
$$\Theta(t) = -A_p \sin(\omega_p t) \tag{4.1}$$

$$X(t) = B_p \sin(\omega_p t) \tag{4.2}$$

where A_p, B_p, and $\omega_p = 2\pi f_p$ denote the angular amplitude, the linear amplitude, and the angular frequency of the plate motion, respectively. Giving $A_p > 0$ and $B_p > 0$, the rotational direction of the object is counter clockwise, as explained in chapter 2.

4.3 Analogy to Bipedal Gaits

Fig. 4.2 and Fig. 4.3 show the experimental result and the simulation result, respectively, with $A_p = 12$ deg, $B_p = 3$ mm, and $\omega_p = 2\pi \times 12$ rad/s. The snapshots in Fig. 4.2 were taken with a high-speed camera to observe in detail the behavior of the object. From these figures, it can be seen that the dynamic behavior in simulation



(a) $t = 0.0$ (b) $t = 0.014$

(c) $t = 0.028$ (d) $t = 0.042$

(e) $t = 0.056$ (f) $t = 0.069$

Figure 4.3: Snapshots of the simulation using $\omega_p/\omega_n = 2.4$. The object is rotating on the plate with an angular velocity of $\omega_B = 350$ deg/s.

and that in the experiment qualitatively correspond to each other. Fig. 4.4 shows the relationship between the angular frequency of the plate ω_p and the angular velocity of the object ω_B in simulation and experiment, where ω_p is normalized by $\omega_n = 10\pi$ rad/s which is the first-order natural angular frequency of the object in bending, that is the frequency with which the object bends up and down freely, with no external force nor restraint. It can be seen that the maximal angular velocity of the object is produced with $\omega_p/\omega_n \approx 2.8$ in both simulation and experiment. This comparison between the experimental and simulation results supports the validity of the parameter estimation and that of the entire simulation model.

Here, it can be noted that the object's behavior changes with respect to ω_p. An interesting observation is that if the whole object is separated into two parts by its center, as shown in Fig. 4.3(a), and regarding each of these parts as left leg and right leg, then the object's behavior can be described with an analogy to bipedal gaits as follows: sliding (both legs always make contact with the floor), as shown in Fig. 4.5(a),

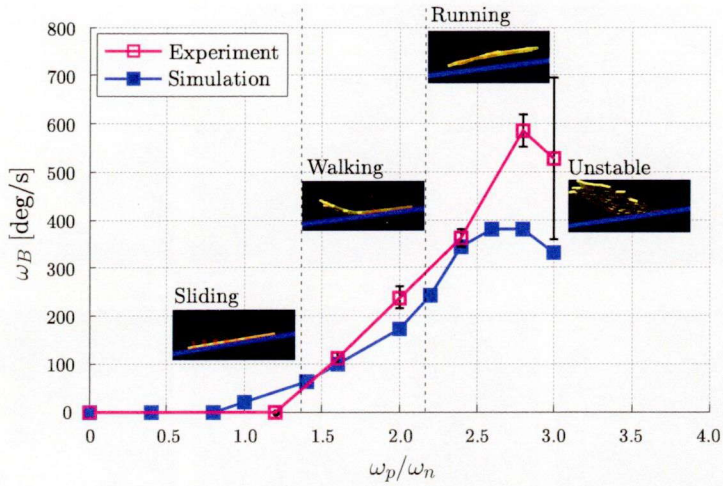
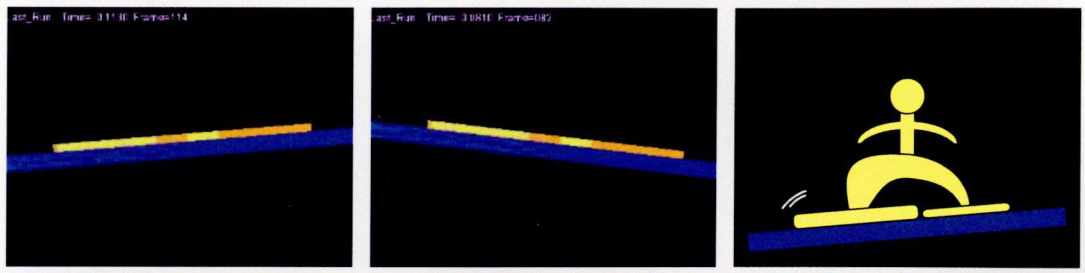


Figure 4.4: Angular velocity of the object ω_B with respect to the angular frequency of the plate ω_p/ω_n. The object's behavior changes as bipedal gaits sliding, walking, and running as ω_p/ω_n increases.

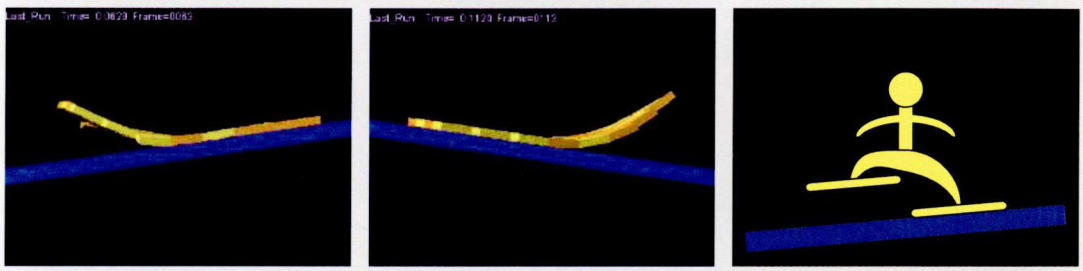
walking (at least one leg makes contact with the floor), as shown in Fig. 4.5(b), and running (both legs float at the same time), as shown in Fig. 4.5(c). The transition of these behaviors as ω_p increases is shown in Fig. 4.4. The maximal angular velocity is achieved in the running phase, which is also dynamically stable. In the running phase it can be observed how the bending motion of the object rhythmically makes contact with the plate, which in consequence makes the object float at the air for some instants of time. This behavior is just as when a human runs keeping its own pace. Finally, for a larger ω_p, the object becomes unstable, and it cannot rotate any more, as shown in Fig. 4.5(d). We define failures as those cases in which the object's center slips more than 10 mm or when the object turns over.

4.4 Optimal Plate Motion

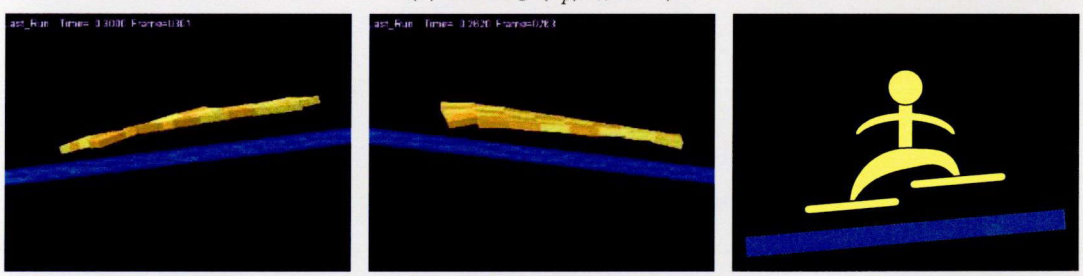
The simulation results in Fig. 4.6 show the relationship between the rotational amplitude of the plate A_p, the angular frequency of the plate ω_p normalized by ω_n, and the angular velocity of the object ω_B with $B_p = 3$ mm. In this case, changing the value of the translational amplitude B_p does not have a significant effect on the object's angular velocity. The dashed lines indicate the maximal angular velocity $\omega_{B\,\max}$ for each A_p, projected onto the ω_p/ω_n–ω_B plane. Each curve stops when the object became unstable



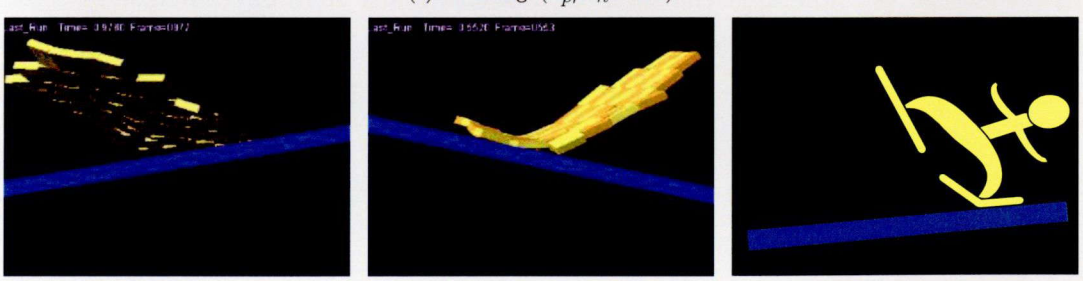
(a) Sliding ($\omega_p/\omega_n = 1.0$)



(b) Walking ($\omega_p/\omega_n = 2.0$)



(c) Running ($\omega_p/\omega_n = 2.6$)



(d) Unstable ($\omega_p/\omega_n = 3.0$)

Figure 4.5: Analogy to bipedal gaits: if the whole object is separated into two parts by its center and regarding each of these parts as left leg and right leg, as shown in Fig. 4.3(a); then the object's behavior can be described with an analogy to bipedal gaits: in (a) sliding (both legs always make contact with the floor), in (b) walking (at least one leg makes contact with the floor), and in (c) running (both legs float at the same time). Failures are defined as those cases in which the object's center slips more than 10 mm or when the object turns over (d).

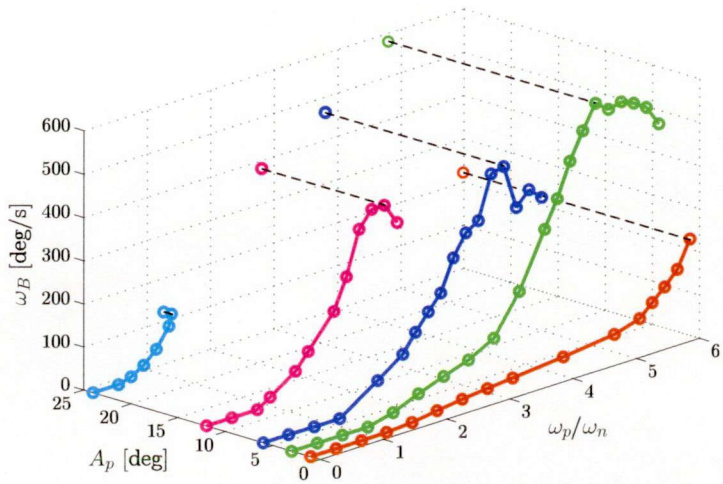
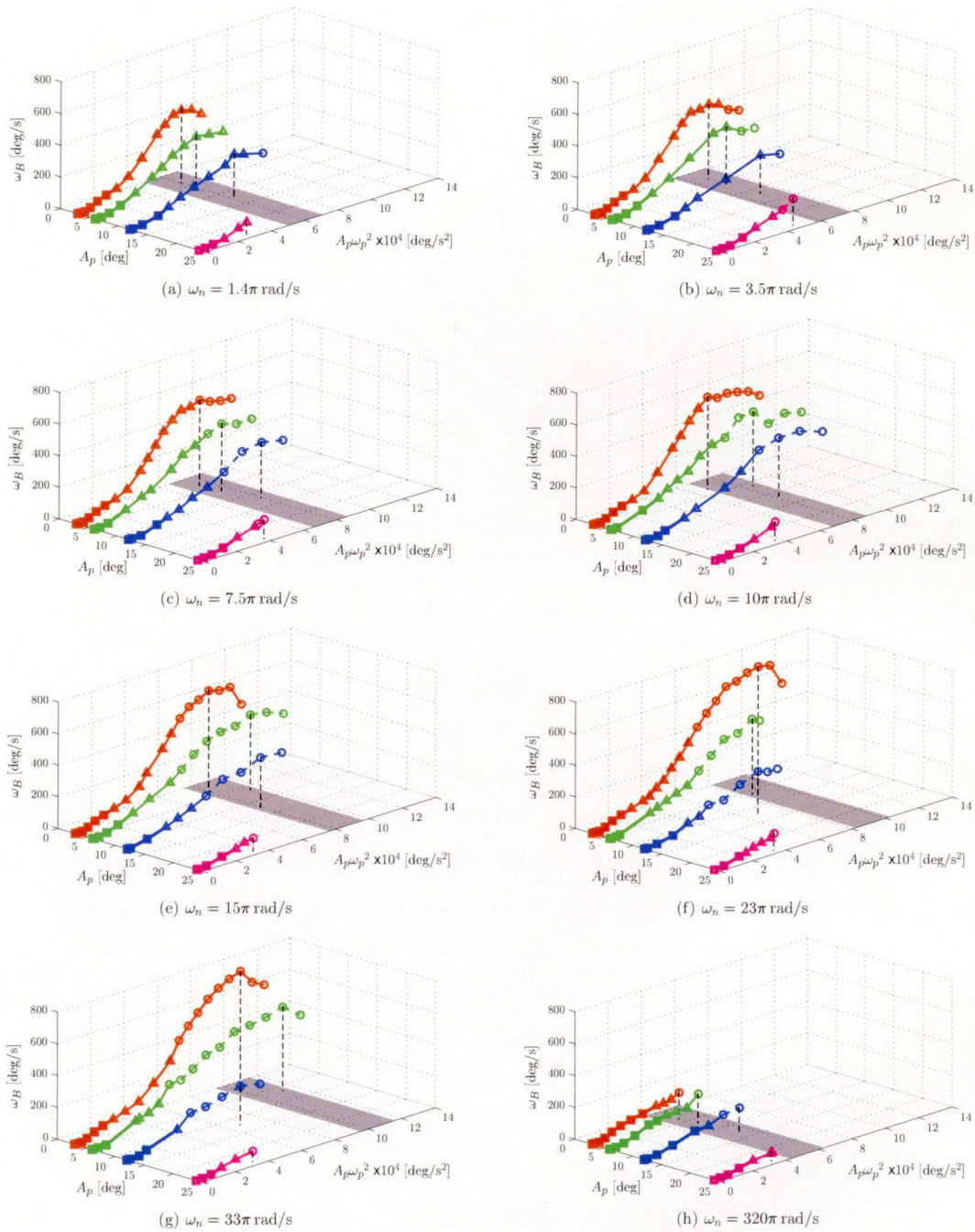


Figure 4.6: Relationship between the plate's rotational amplitude A_p, the plate's angular frequency normalized by the first-order natural frequency of the object in bending ω_p/ω_n, and the angular velocity of the object ω_B with $B_p = 3$ mm.

and failed to rotate, which we define in the previous section, as shown in Fig. 4.5(d). If the robot can generate a high-frequency motion of the plate, e.g. $\omega_p/\omega_n = 5$, the object will be able to rotate faster more stably with a small angular amplitude of the plate rather than with a large one. It can be intuitively understood that a small angular amplitude A_p contributes to the stability of the rotating object. From Fig. 4.6, the optimal combination of A_p and ω_p can be obtained, which leads to the maximal angular velocity of the object, under the given specification of the robot system.

Fig. 4.7(a)–(h) shows the relationship between the angular amplitude of the plate A_p, the angular acceleration of the plate $A_p\omega_p^2$, and the angular velocity of the object ω_B, where the natural angular frequency of the object is: (a) $\omega_n = 1.4\pi$ rad/s, (b) $\omega_n = 3.5\pi$ rad/s, (c) $\omega_n = 7.5\pi$ rad/s, (d) $\omega_n = 10\pi$ rad/s, (e) $\omega_n = 15\pi$ rad/s, (f) $\omega_n = 23\pi$ rad/s, (g) $\omega_n = 33\pi$ rad/s, and (h) $\omega_n = 320\pi$ rad/s, with $B_p = 3$ mm. The value of ω_n is changed by modifying the elasticity of the object for the same mass. In Fig. 4.7, the □, △, and ○ denote the object's sliding, walking, and running phases, respectively. The dashed lines indicate the maximal angular velocity $\omega_{B\,\max}$ for each A_p, projected onto the A_p–$A_p\omega_B^2$ plane. As shown in Fig. 4.7(h), the object with the highest stiffness becomes unstable even with a low acceleration of the plate. Thus, the maximal angular velocity of the object $\omega_{B\,\max}$ is smaller than that of the softer objects in Fig. 4.7(a)–(g). This corresponds to the experimental results as shown in Fig. 2.7 and Fig. 2.9.



(a) $\omega_n = 1.4\pi$ rad/s (b) $\omega_n = 3.5\pi$ rad/s

(c) $\omega_n = 7.5\pi$ rad/s (d) $\omega_n = 10\pi$ rad/s

(e) $\omega_n = 15\pi$ rad/s (f) $\omega_n = 23\pi$ rad/s

(g) $\omega_n = 33\pi$ rad/s (h) $\omega_n = 320\pi$ rad/s

Figure 4.7: Relationship between the plate's rotational amplitude A_p, the plate's angular acceleration $A_p\omega_p^2$, and the angular velocity of the object ω_B with $B_p = 3$ mm. The object's behavior changes with respect to the plate's angular acceleration, from sliding □, to walking △, and to running ◯.

From Fig. 4.7(a)–(h), it can be confirmed that the optimal angular acceleration $A_p\omega_p^2$ is uniquely determined for each of the deformable objects, as indicated by the shaded area, while the maximal angular velocity of the object $\omega_{B\,\max}$ changes depending on how large the amplitude A_p is chosen. It can be noted that for $A_p = 24$ deg, the maximal angular velocity of each of the objects $\omega_{B\,\max}$ in Fig. 4.7(a)–(h), is not within the shaded area, since the objects fall from the plate or turn over before achieving a fast rotation. This means that the plate's amplitude is too large to stably manipulate these objects. Furthermore, it can be seen that for $A_p = 12$ deg, the maximal angular velocity of each of the harder objects in Fig. 4.7(f)–(h) is not within the shaded area. This means that the plate's amplitude $A_p = 12$ deg is still too large to allow these objects to rotate stably on the plate. As shown in Fig. 4.7(c)–(h), the maximal angular velocity of the object $\omega_{B\,\max}$ is produced in the running phase. This means that, to rotate the object faster, the plate needs a large enough acceleration to push up the object so that it can run and turn. In this case, the object mainly rotates in the air by utilizing the inertial effect around its center of mass. However, as shown in Fig. 4.7(a) and (b), the maximal angular velocity of the object is produced in the walking phase. The reason is that the object is too soft, hence the object is greatly deformed, and as a result, it is folded in two before it starts to run. Thus, although the object's behavior differs, an appropriate angular acceleration of the plate is essential to generate a fast and stable rotation of the deformable object. Based on the aforementioned results, we can estimate the specifications of the robot's actuators needed for this manipulation scheme.

4.5 Optimal Friction Coefficient

The simulation results in Fig. 4.8(a) show the relationship between the angular acceleration of the plate $A_p\omega_p^2$, the friction angle between the plate and the object $\alpha = \tan^{-1}(\mu_s)$ and the angular velocity of the object ω_B, for a plate's angular amplitude $A_p = 3$ deg, translational amplitude $B_p = 3$ mm and $\omega_n = 10\pi$ rad/s. The □, △, and ○ denote the object's sliding, walking, and running phases, respectively. Fig. 4.8(b) shows the top view of Fig. 4.8(a) with ω_B normalized by $\omega_{B\,\max}$ and represented with contour lines or isolines, that is, the isoline of κ indicates the points at which $\omega_B/\omega_{B\,\max} = \kappa$, for $0 < \kappa \leq 1$. Here, it must be pointed out that not only the static coefficient of friction

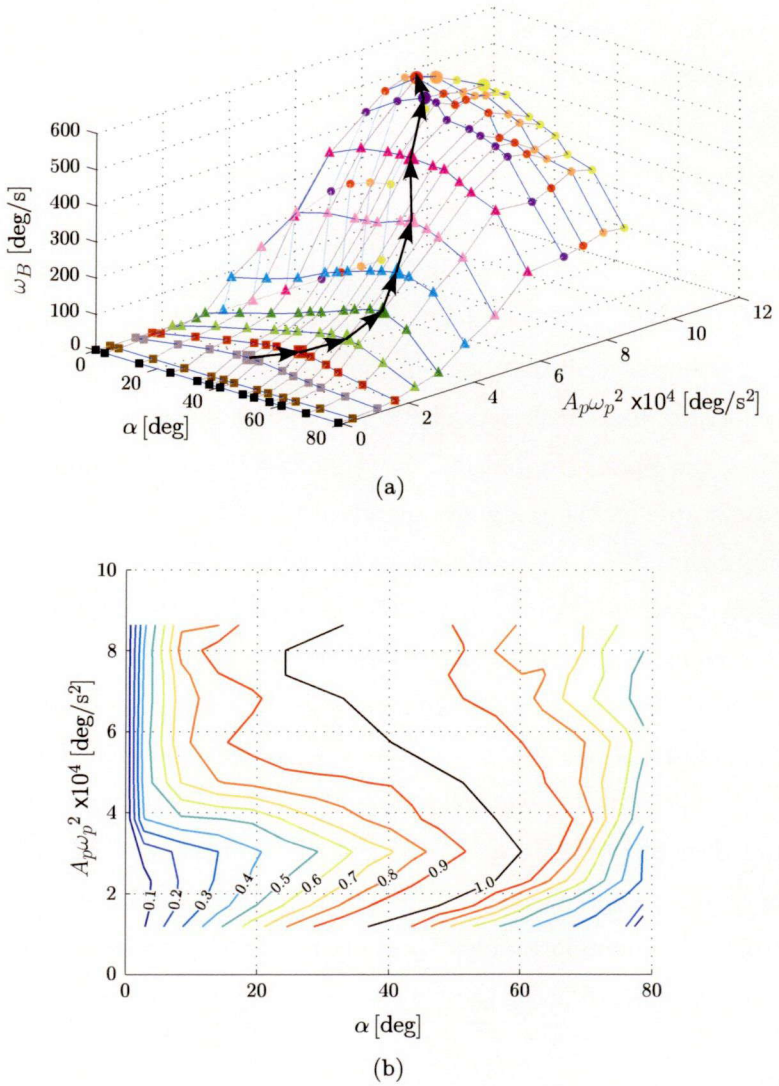


Figure 4.8: Relationship between the friction angle between the plate and the object α, the angular acceleration of the plate $A_p\omega_p^2$, and the angular velocity of the object ω_B with $A_p = 3$ deg, $B_p = 3$ mm and $\omega_n = 10\pi$ rad/s in (a), and the top view of (a) with ω_B normalized by its maximal value and represented with contour lines in (b). The optimal friction angle depends on the object's sliding □, walking △, and running gaits ◯, as denoted by the arrows in (a) and by the black line in (b).

μ_s, but also the dynamic coefficient of friction μ_k changes and it does it proportionally to μ_s, that is $\mu_k = \beta\mu_s$, where $\beta = 0.53$ is constant. This value of β was calculated based on the friction coefficients obtained experimentally for the slice of cheese.

The friction's influence in the object's angular velocity ω_B, as shown in Fig. 4.8,

can also be explained with the analogy to bipedal gaits. When the friction angle α is around 0 deg, the object cannot rotate fast because the moment that contributes to rotation n_+ cannot be generated. This corresponds with a slippery floor for a biped's gait. In the other extreme, when the friction angle α is around 80 deg, the object also cannot rotate fast. This is because the frictional force that is perpendicular to the plate's translational motion X increases as well as the one parallel to X. Therefore, the object will eventually not be able to rotate on the plate, as the friction angle α approaches 90 deg. This corresponds with a sticky floor, where a biped can hardly step. Thus the optimal friction angle leading to the maximal angular velocity $\omega_{B\max}$ exists in an intermediate friction value. For a small $A_p\omega_p^2$ as in the sliding phase $\square$, the object keeps full contact with the plate, and no deformation occurs. In this case, both the contributing moment n_+ and the braking moment n_- are generated, as shown in Fig. 2.6(c), and the optimal friction angle is around 40 deg. In the walking phase $\triangle$, the braking moment n_- decreases due to the object's deformation, as explained in Fig. 2.6(d). Therefore, the optimal friction angle moves to a larger one, around 60 deg, so as to increase the contributing moment n_+ without overcoming the inertial force. For a larger $A_p\omega_p^2$ as in the running phase $\bigcirc$, the object's contact area during rotation is drastically reduced. Thus, the object rotates faster by the inertial effect while floating on the air for most of the time, without making contact with the plate. In this case, a large friction brakes the object's rotation at the instants of time it makes contact with the plate. To avoid this braking, the optimal friction angle moves to a smaller one, around 30 deg. As was explained, the optimal friction angle that is denoted by arrows in Fig. 4.8(a), depends on the object's sliding, walking, and running gaits.

Furthermore, the optimal angular acceleration $A_p\omega_p^2$ is obtained around 8 deg/s^2, regardless of the friction angle α. This angular acceleration is the same as the one obtained in Fig. 4.7(d). This confirms that an appropriate plate's angular acceleration is the most important factor for a fast object's rotation.

4.6 Summary

In this chapter, towards the optimal manipulation, simulation analysis of rotating a deformable object on a plate were carried out after comparing the simulation results with the experimental ones to validate the simulation model introduced in chapter

3. Through simulation analysis, it was discovered that the transition of the object's rotational behavior with respect to the plate's motion frequency mimics either a sliding, walking, or running gait of a biped. Then, the optimal plate motion leading to the object's maximal angular velocity was obtained. Here it was revealed that the angular acceleration of the plate is the most important factor for a dynamically stable and fast object rotation. Finally, the influence of the friction between the plate and the object in the object's angular velocity was discussed. It was shown that the optimal friction coefficient depends on the object's bipedal gait-like behavior. The results shown in this chapter could be a guideline for the design of a fast and dynamically stable manipulation strategy.

Chapter 5

Estimating Physical Parameters of an Object

5.1 Introduction

This chapter discusses how to identify two physical parameters of deformable objects by nonprehensile manipulation, characterizing the transition of the object's angular velocity. After explaining the concept in section 5.2, it is shown that that the curve describing the relationship between the plate's motion frequency and the object's angular velocity has a resonance-like curve in section 5.3. Using this similarity, we employ a Lorentzian curve fitting to represent the dynamic characteristics of the object's rotation with a simple mathematical expression, instead of the equation of motion that is rather complex and difficult to obtain because of the intricate dynamics of the system. In section 5.4 and 5.5, through simulation analysis it is revealed that two physical parameters: the first-order natural angular frequency in bending of the object ω_n, and the friction angle α between the object and the plate, strongly dominate the Lorentzian curve characteristics. Based on such nature, we propose an identification method to estimate these physical parameters of unknown objects. Finally, in section 5.6 we show the simulation and experimental results of estimating these parameters to confirm the validity of the proposed method.

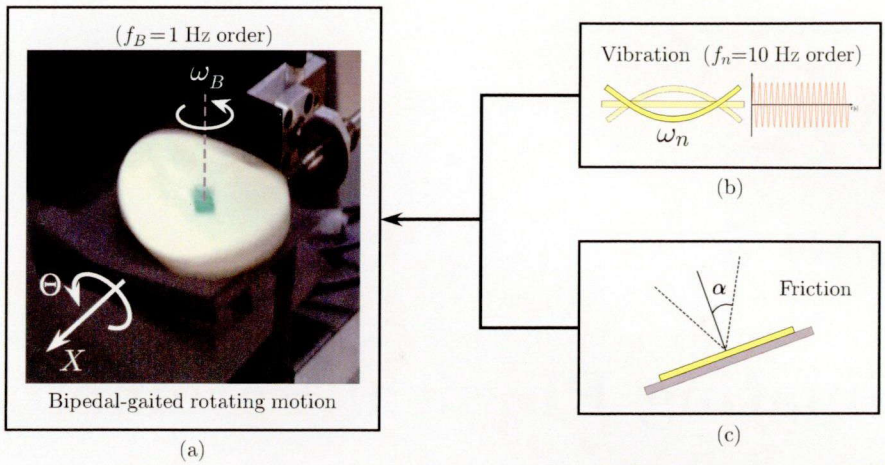


Figure 5.1: The object's angular velocity ω_B that corresponds to a low rotation frequency f_B in (a) is the result of the combination of the object's high natural angular frequency in bending w_n in (b) and the friction angle α between the plate and the object in (c).

5.2 Nonprehensile Approach to Estimate Physical Parameters of an Object

Let us focus on the fact that in the manipulation scheme used in this dissertation, the object's high frequency in bending vibration of 10 Hz order is converted to a low-frequency rotating motion of $f_B \approx 1$ Hz order, as a result of the friction effect together with the object's bipedal gait-like behavior, as illustrated in Fig. 5.1. This suggests that the information of two physical parameters of the object: the natural bending frequency of $f_n \approx 10$ Hz order when using comestible products such as cheese or ham, and the friction is included in the frequency of rotation of the object, that is, the object's angular velocity. Therefore, we may be able to estimate them by only observing the object's low rotation frequency on the plate. An important advantage is that as we only have to deal with the object's low rotation frequency, a normal camera with 30 fps can be utilized. Otherwise, to directly observe the object's high bending vibration frequency, a high-speed camera with hundreds or thousands fps order is required to guarantee a high accuracy in the measurements. This kind of nonprehensile approach for sensing the parameters of an object may be applicable to the evaluation of freshness and texture of food, which alters the bending frequency of food. Besides, as this manipulation scheme can prevent a large concentration of stress, it is also expected to significantly contribute

to the cell/tissue processing technology in the bioscience research. A change in tissue stiffness could be an indicator of some diseases such as cancer. In our approach the bending frequency may be use as a stiffness evaluation index.

5.3 Characterization of the Object's Angular Velocity

In this section, based on simulation analysis we show how the curve representing the relationship between the object's angular velocity ω_B and the plate's motion frequency f_p can be described by a peak function such as the Lorentz one, and its similarity with the resonance phenomenon.

5.3.1 Object's Angular Velocity Transition

Let us now focus on the transition of the object's angular velocity ω_B through simulation analysis. Fig. 5.2(a) shows examples of the relationship between the object's angular velocity ω_B, the plate's motion frequency f_p, and the plate's angular amplitude A_p for a deformable object of circular shape, with $\omega_n = 10\pi$ rad/s, a friction angle between the plate and the object of $\alpha = 36.9$ deg, and a translational amplitude $B_p = 3$ mm. From Fig. 5.2(a), it can be seen that for $A_p = 3$ deg the object has its maximal angular velocity $\omega_{B\,\max}$ around $f_p = 24$ Hz, and that for frequencies larger than this the object's angular velocity decreases as the object becomes unstable, forming a peak-shaped line. The combination of f_p and A_p will determined when the object becomes unstable and these cases are not plotted on Fig. 5.2. For this reason, in the extreme case of the largest $A_p = 24$ deg in Fig. 5.2(a), the plotted line do not have a peak as in the other cases ($A_p = 3$, 6, and 12 deg). On the other hand, a plate amplitude of $A_p = 1$ deg needs much larger frequencies of f_p for a peak to appear. Fig. 5.2(b) shows the relationship between f_p and ω_B for various deformable objects with different ω_n. From this figure, it can be seen that the frequency at which $\omega_{B\,\max}$ occurs, is uniquely determined for each of these deformable objects. Also, we would like to point out that in Fig. 4.3 the object is making contact with the plate frequently, as the object rotates on the plate with bipedal gait-like motions. This suggests that the energy dissipation of the object is mostly due to the friction between the plate and the object. In this case the damping effect of the viscoelastic joint units is considered to be negligible. Based on

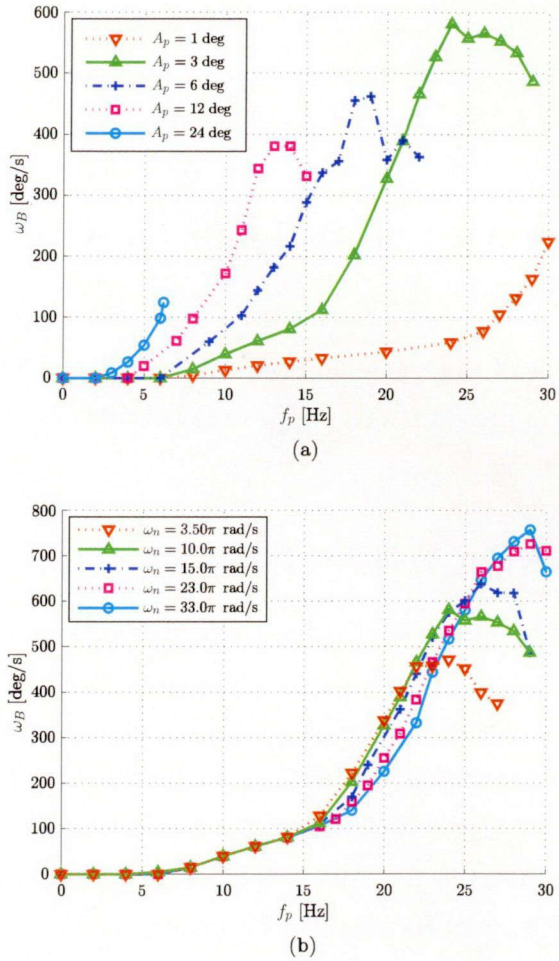


Figure 5.2: Relationship between the object's angular velocity ω_B and the plate's motion frequency f_p with respect to (a) the plate's angular amplitude A_p for $\omega_n = 10\pi$ rad/s, and (b) the object's first-order natural frequency in bending ω_n for $A_p = 3$ deg. Both (a) and (b) with $B_p = 3$ mm and $\alpha = 36.9$ deg.

this observation, we can expect that the object's angular velocity transition strongly depends not only on ω_n but also on α.

5.3.2 Curve Fitting Using the Lorentz Distribution Function

As mentioned before, the object's angular velocity transition has a peak-shaped line which is characteristic of a resonant behavior, i.e. the object's angular velocity ω_B reaches its maximal amplitude $\omega_{B\,\max}$ only at the frequency of resonance. Taking advantage of this similarity, we employ a nonlinear regression analysis to represent the

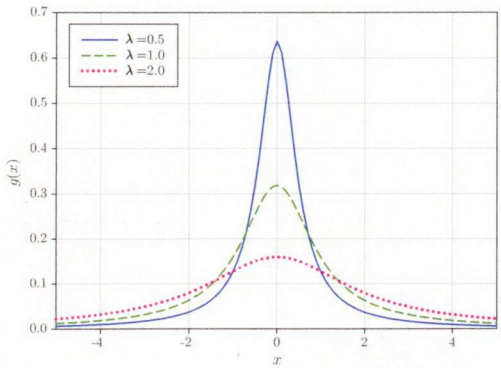


Figure 5.3: Lorentz distribution for three different values of λ and $x_0 = 0$.

transition of the angular velocity of the object by a simple mathematical expression, which otherwise would be rather complex due to the intricate dynamics involved in this system.

One of the most common functions describing a resonant behavior in curve fitting is the Lorentz distribution (also known as Cauchy distribution [100]) function

$$g(x) = \frac{1}{\pi\lambda\left(1 + \left(\frac{x-x_0}{\lambda}\right)^2\right)} \tag{5.1}$$

where x_0 is the median of the distribution, and λ is the half width at half maximal (HWHM) of the probability density function $g(x)$. These two parameters determine the shape of $g(x)$, and its maximal amplitude at $x = x_0$ is given by

$$a = \frac{1}{\pi\lambda}\ , \tag{5.2}$$

which depends on the value of λ. Fig. 5.3 shows the plot of equation (5.1) for three different values of λ and $x_0 = 0$. In this figure it can be seen that as the value of λ increases the value of the maximal amplitude of $g(x)$ decreases, as stated in equation (5.2). To have the maximal amplitude independent of the width of the curve we introduce a third parameter γ, equation (5.2) is now given as

$$\tilde{a} = \frac{\gamma}{\pi\lambda}\ . \tag{5.3}$$

Consequently, equation (5.1) is replaced by

$$\tilde{g}(x) = \frac{\tilde{a}}{1 + \left(\frac{x-x_0}{\lambda}\right)^2}\ . \tag{5.4}$$

In equation (5.3), the parameter γ can change the maximal amplitude, therefore we can have curves with the same maximal amplitude but different widths, that cannot be obtained by using equation (5.2). This third parameter γ allows the nonlinear regression to get a better approximation of the data to be fitted. Using equation (5.4) to express the transition of the object's angular velocity ω_B as a function of the plate's motion frequency f_p, we have

$$\omega_B(f_p) = \frac{\omega_{Br\,\max}}{1 + \left(\frac{f_p - f_0}{b}\right)^2}. \tag{5.5}$$

where $\omega_{Br\,\max}$ is the maximal amplitude of ω_B at $f_p = f_0$, b is the HWHM and f_0 is the frequency at which $\omega_B = \omega_{Br\,\max}$. The data analysis software Sigmaplot (Systat Software, Inc.) is utilized for the nonlinear regression analysis. This software uses the Marquardt-Levenberg algorithm to find the parameters $\omega_{Br\,\max}$, f_0, and b, that together with equation (5.5), yields the best approximation to the given data.

We carry out the nonlinear regression analysis of Fig. 5.2(b) for $\omega_n = 10\pi$ rad/s and $\omega_n = 33\pi$ rad/s with $\alpha = 36.9$ deg by using equation (5.5), the resulting line shapes are shown in Fig. 5.4(a) and (b), respectively, where the dotted line represents the simulation data and the solid line represents the regression line. The parameters obtained from this regression are $\omega_{Br\,\max} = 598.7$ deg/s, $b = 5.1$ Hz, and $f_0 = 25.1$ Hz, for $\omega_n = 10\pi$ rad/s and $\omega_{Br\,\max} = 746.9$ deg/s, $b = 5.8$ Hz, and $f_0 = 28.2$ Hz, for $\omega_n = 33\pi$ rad/s. Here the parameter f_0 can be regarded as a kind of frequency of resonance at which $\omega_{Br\,\max}$ occurs, and it can be seen that it is different for each object, as ω_n is different. The coefficient of determination is $R^2 = 0.99$ for $\omega_n = 10\pi$ rad/s and $R^2 = 0.99$ for $\omega_n = 33\pi$ rad/s, the closer R^2 is to one, the better the plate's motion frequency (independent variable) predicts the object's angular velocity (dependent variable). Additionally, the nonlinear regression analysis for $\omega_n = 10\pi$ rad/s and $\alpha = 56.3$ deg, is shown in Fig. 5.4(c). The parameters obtained from this regression are $\omega_{Br\,\max} = 520.9$ deg/s, $b = 5.8$ Hz, $f_0 = 24.6$ Hz, and $R^2 = 0.98$. If we compare the result in Fig. 5.4(c) with the one from Fig. 5.4(a), it can be observed that their f_0 are almost the same, while the values of $\omega_{Br\,\max}$ and b are different. The results in Fig. 5.4 imply that two physical parameters ω_n and α determine the combinations of the regression parameters $\omega_{Br\,\max}$, f_0, and b.

To simplify the simulation analysis, in the following sections we suppose that all the deformable objects have the same negligible thickness, the same circular shape, and

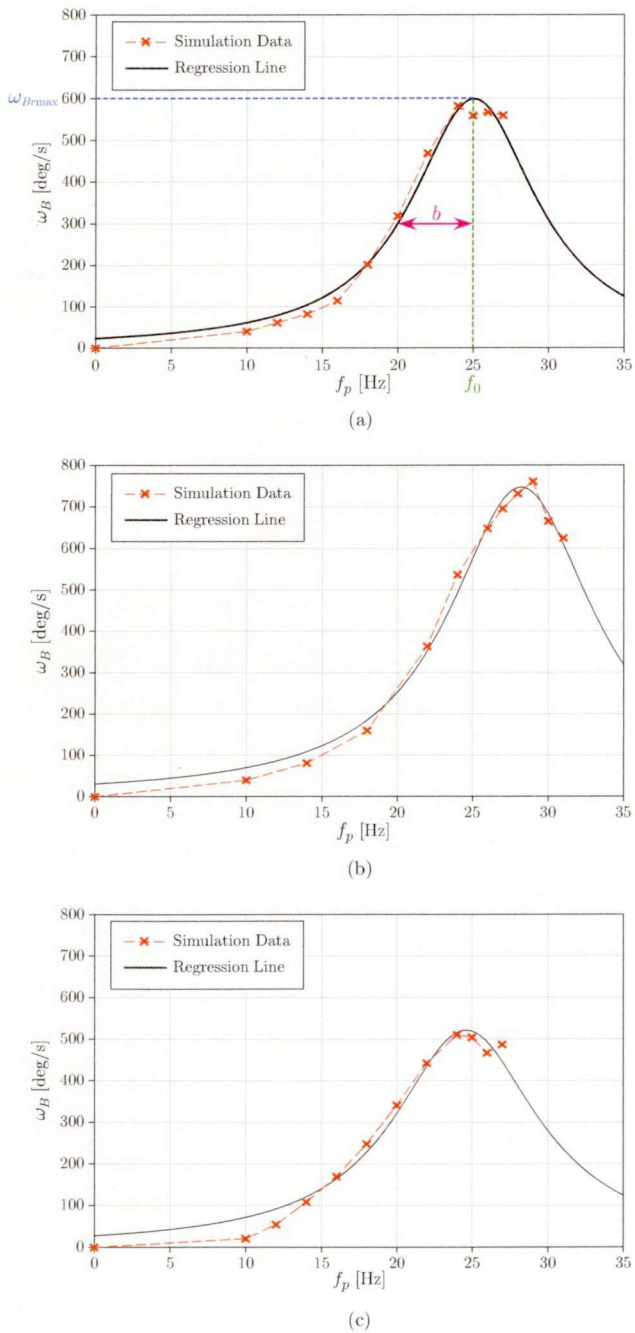


Figure 5.4: Relationship between the object's angular velocity ω_B and the plate's motion frequency f_p, for (a) $\omega_n = 10\pi$ rad/s, $\alpha = 36.9$ deg, (b) $\omega_n = 33\pi$ rad/s, $\alpha = 36.9$ deg, and (c) $\omega_n = 10\pi$ rad/s, $\alpha = 56.3$ deg.

the same diameter of 80 mm. Also we only use A_p = 3, 12 deg, and B_p = 3 mm for the plate's amplitudes.

In this section, we showed that the Lorentz distribution function can be used to represent the dynamic behavior of the object. This Lorentz distribution has its origins in the electromagnetic theory of Lorentz, typically used to express the light resonance radiation phenomenon[101]. Also, there is the "Breit-Wigner" resonance formula in quantum-mechanics, which is said to be the analog of the Lorentz one in electromagnetic theory[102] as they have the same line shape.

5.4 Estimation of the Object's Natural Angular Frequency in Bending

In this section, based on the curve fitting of the object's angular velocity line shape, we propose an identification method of the object's natural bending frequency ω_n that is supposed to be one of the dominating parameters in the object's angular velocity line shape as mentioned in section 5.3.2.

Fig. 5.5 shows the relationship between the object's angular velocity ω_B and the plate's frequency f_p, for different friction angles α and different deformable objects, that is ω_n is different, for plate amplitudes of A_p = 3 deg in (a) and A_p = 12 deg in (b). Fig 5.6 shows the values of the parameter $\omega_{Br\,\max}$ resulting from the nonlinear regression analysis of the simulation data of Fig. 5.5, for A_p = 3 deg in (a) and A_p = 12 deg in (b). The coefficients of determination of these regressions can be consulted in Appendix A. From this figure it can be seen that the value of $\omega_{Br\,\max}$ increases as ω_n increases. The thick straight line represents the regression line between $\omega_{Br\,\max}$ and ω_n that has a coefficient of determination of R^2 = 0.93 and 0.83, for A_p = 3 and 12 deg, respectively. However, it can be observed that for each ω_n the value of $\omega_{Br\,\max}$ also changes depending on the friction angle α, particularly for the biggest two α in Fig. 5.6(a), and that for each ω_n the value of $\omega_{Br\,\max}$ changes significantly depending on the friction angle α in particular for the two deformable objects with higher ω_n in Fig. 5.6(b). From this relationship it is difficult to decompose the effects of ω_n and α on $\omega_{Br\,\max}$. This means that ω_n cannot be estimated simply by observing $\omega_{Br\,\max}$.

We next focus on the parameter f_0. Fig 5.7(a) shows the resulting parameter f_0 with respect to ω_n for A_p = 3 deg and the same friction angles in Fig. 5.5(a). In the

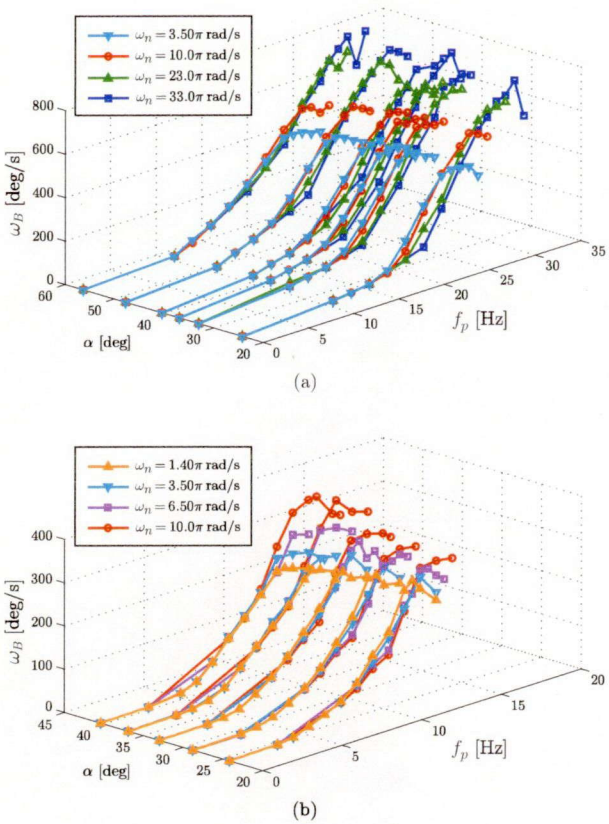


Figure 5.5: Relationship between the object's angular velocity ω_B and the plate's motion frequency f_p, for different friction angles α and different deformable objects for (a) $A_p = 3$ deg and (b) $A_p = 12$ deg, with $B_p = 3$ mm.

same way, Fig 5.7(b) shows the results of f_0 with respect to ω_n for $A_p = 12$ deg. In Fig. 5.7, it can be seen that the value of f_0 increases as ω_n increases for each α, and that the value of f_0 does not change significantly for the same ω_n and different α. Here, the thick straight line represents the regression line between f_0 and ω_n that has a coefficient of determination of $R^2 = 0.99$ for $A_p = 3$ in Fig. 5.7(a) deg and $R^2 = 0.96$ for $A_p = 12$ deg in Fig. 5.7(b), which are better than those obtained in Fig. 5.6(a) and (b), respectively. The lines for almost all the different α have a similar slope with the regression line. This result suggests that the object's ω_n can be estimated by a linear equation as a function of f_0, regardless of the friction angle α, as follows,

$$\hat{\omega}_n = p_1 f_0 + q_1 \tag{5.6}$$

for each of the plate amplitudes A_p. Therefore, if we obtain f_0 from the curve fitting

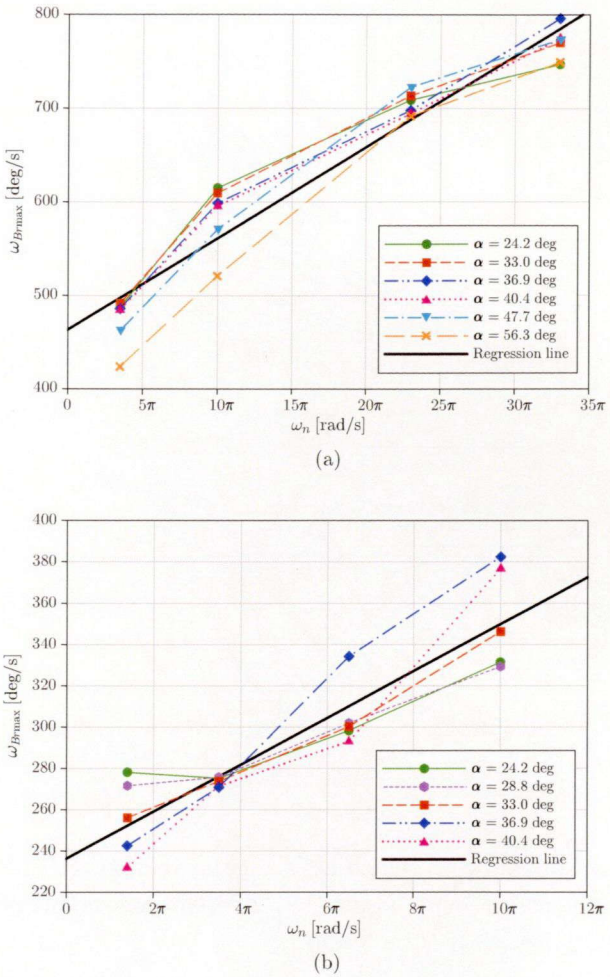


Figure 5.6: Relationship between the object's first-order natural angular frequency in bending ω_n and the parameter $\omega_{Br\,\max}$ obtained from the nonlinear regression of f_p vs. ω_B, for (a) $A_p = 3$ deg and (b) $A_p = 12$ deg, with $B_p = 3$ mm.

of the relationship between the object's angular velocity ω_B and the plate's motion frequency f_p, then we can estimate the value of the object's natural angular frequency in bending ω_n.

The frequency f_0 when $A_p = 3$ deg is in the range of $23 < f_0 < 30$ Hz, as shown in Fig. 5.7(a), while the frequency f_0 when $A_p = 12$ deg is in the range of $11 < f_0 < 14$ Hz, as shown in Fig. 5.7(b). Therefore, $A_p = 12$ deg is convenient from the experimental viewpoint of the actuators. However, for a plate amplitude of $A_p = 12$ deg the object easily becomes unstable or folded in half. As a result, it can only deal with objects

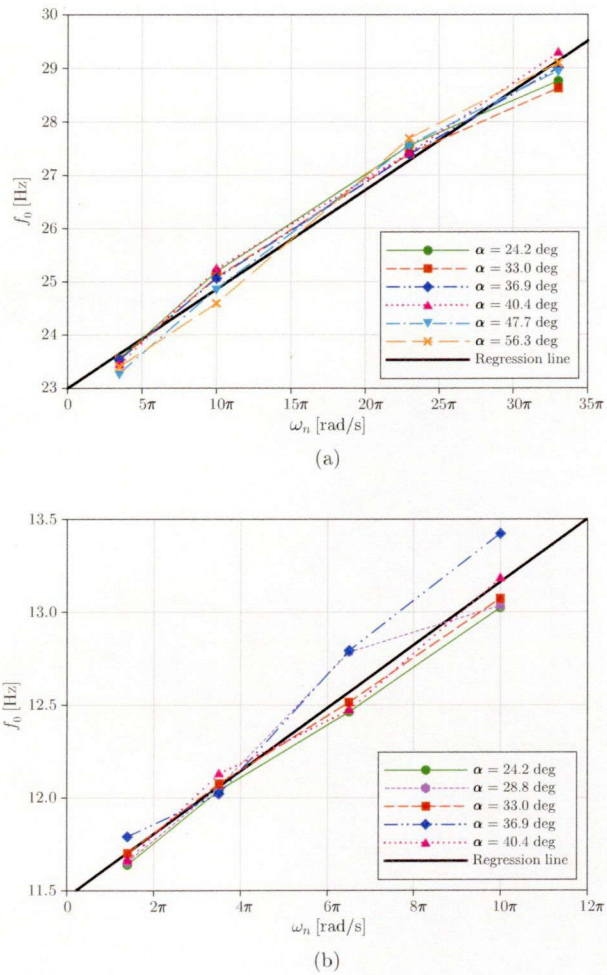


Figure 5.7: Relationship between the object's first-order natural angular frequency in bending ω_n and the parameter f_0 obtained from the nonlinear regression of f_p vs. ω_B, for (a) $A_p = 3$ deg and (b) $A_p = 12$ deg, with $B_p = 3$ mm.

whose ω_n are less than 12π rad/s.

5.5 Estimation of the Friction between the Object and the Plate

In this section, we propose an identification method of the friction angle α between the object and the plate that is supposed to be another dominating parameter in the object's angular velocity line shape.

We had already analyzed two ($\omega_{Br\,\max}$ and f_0) of the three parameters involved in

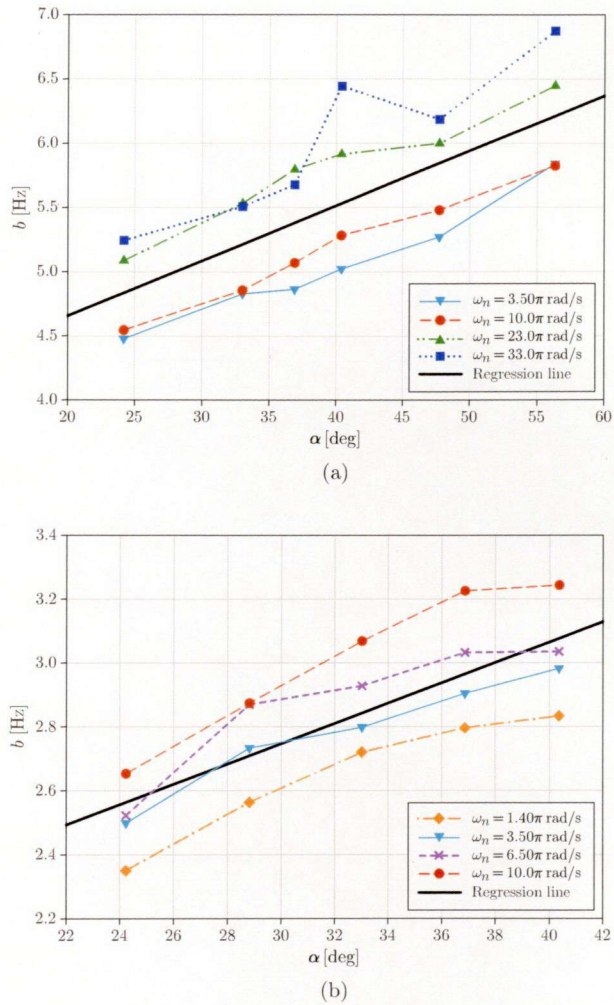


Figure 5.8: Relationship between the friction angle α and the half width at half maximal b obtained from the nonlinear regression of f_p vs. ω_B, for (a) $A_p = 3$ deg and (b) $A_p = 12$ deg.

the Lorentz curve fitting. Now we focus on the parameter b. Fig. 5.8 shows the results for the parameter b with respect to α obtained from the nonlinear regression analysis of the simulation data of Fig. 5.5, for $A_p = 3$ deg in (a) and $A_p = 12$ deg in (b). From Fig. 5.8(a) it can be seen that the values of b for $\omega_n = 3.5\pi$ rad/s and $\omega_n = 10\pi$ rad/s are similar, while the ones for $\omega_n = 23\pi$ rad/s and $\omega_n = 33\pi$ rad/s are near to each other and notably larger than the previous ones. Similarly in Fig. 5.8(b) it can be seen that the values of b for each of the deformable objects shown are significantly different from each other. The thick straight line represents the regression line between b and α

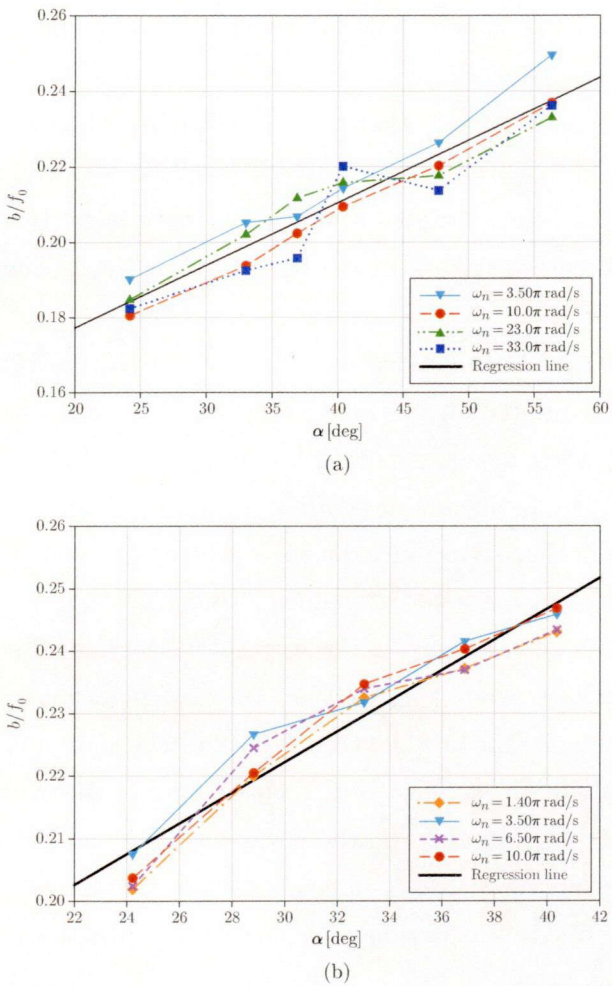


Figure 5.9: Relationship between the half width at half maximal b divided by the frequency of resonance f_0 and the friction angle α obtained from the nonlinear regression of f_p vs. ω_B, for (a) $A_p = 3$ deg and (b) $A_p = 12$ deg.

that has a coefficient of determination of $R^2 = 0.52$ for $A_p = 3$ in Fig. 5.8(a) deg and $R^2 = 0.62$ for $A_p = 12$ deg in Fig. 5.8(b). In this case there is no unique value of α for each value of b.

Let us now use the value of b normalized by f_0 and focus on the relationship between α and b/f_0 that contains the information of the sharpness of the curve. Fig 5.9(a) shows the relationship between α and b/f_0, for $A_p = 3$ deg and the same deformable objects in Fig. 5.5(a). In the same way, Fig 5.9(b) shows the results of b/f_0 with respect to α for $A_p = 12$ deg. From this figure, it can be observed that as the friction angle α

increases, b/f_0 also increases and that the values of b/f_0 of the four different objects for the same friction angle α are similar. Here, the thick straight line represents the regression line between α and b/f_0 that has a coefficient of determination of $R^2 = 0.90$ for $A_p = 3$ deg in Fig. 5.9(a) and $R^2 = 0.93$ for $A_p = 12$ deg in Fig. 5.9(b), which are better than those obtained in Fig. 5.8(a) and (b), respectively. It can be seen that the lines for all the different ω_n have similar slopes with the regression line in each of the graphs.

In general the parameter b divided by f_0 represents the damping coefficient which produces the energy dissipation of the system[103]. Fig. 5.10 shows the results for the parameter b/f_0 with respect to different damping coefficients for four different object's natural angular frequency in bending ω_n for $A_p = 3$ deg. Here, the damping coefficients c_c and c_b in Fig. 3.3 are varied using the expressions: $c_c = \eta c_{c_0}$ and $c_b = \eta c_{b_0}$, respectively. Where $c_{c_0} = 4.9 \times 10^{-4}$ N/(mm/s) and $c_{b_0} = 4.23 \times 10^{-6}$ N·mm/(deg/s) are those estimated in section 3.3. As it can be seen there is no significant difference among the values of b/f_0 when varying the damping coefficients. The thick straight line represents the regression line between b/f_0 and the damping coefficients, which coefficient of determination is $R^2 = 0.02$. This confirms that the damping effect of the object's viscoelastic joint units on the parameter $b/f0$ is negligible, as mentioned in section 5.3.1. In our model, b/f_0 depends on the friction angle α, as the energy dissipation is mainly due to the friction between the plate and the object, in the object's bipedal gaited-like motions.

From the linear regression in Fig. 5.9, the friction angle α can be estimated by a linear equation as a function of b/f_0 for each angular amplitude A_p as follows,

$$\hat{\alpha} = p_2(b/f_0) + q_2 \ . \tag{5.7}$$

Therefore, if we obtain b and f_0 from the curve fitting of the relationship between the object's angular velocity ω_B and the plate's motion frequency f_p, then we can estimate the value of the friction angle α between the plate and the object.

The friction angle α is in the range of $24 < \alpha < 57$ deg when $A_p = 3$ deg, as shown in Fig. 5.9(a), while it is in the range of $24 < \alpha < 41$ deg when $A_p = 12$ deg, as shown in Fig. 5.9(b). The smallest friction angle $\alpha = 24$ deg may seem large to be a lower limit, while the largest $\alpha = 57$ deg may seem small to be an upper limit, if we consider the theoretical full range of possible alpha $0 < \alpha < 90$ deg. As discussed in

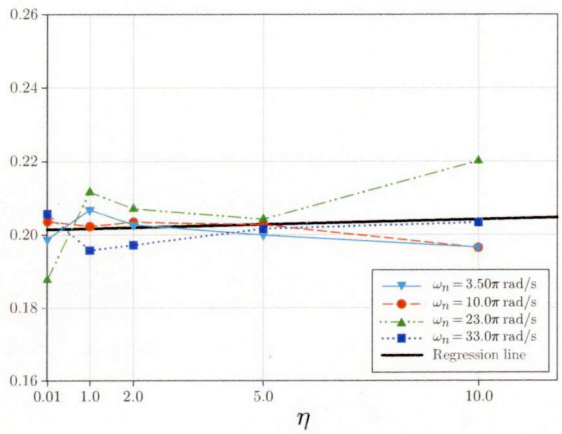


Figure 5.10: Relationship between the half width at half maximal b divided by the frequency of resonance f_0 and the ratio γ expressing the damping coefficients as $c_c = \eta c_{c_0}$ and $c_b = \eta c_{b_0}$, for four different ω_n and $A_p = 3$ deg.

the previous chapter in section 4.5, in the neighborhood of $\alpha = 0$ deg and 90 deg the object cannot rotate fast, thus the object's angular velocity peak-shaped line appearing for $24 < \alpha < 57$ deg is difficult to obtain. Since the method proposed is based on the nonlinear regression of the peak-shaped line of the object's angular velocity it is not possible to estimate friction angles outside the range $24 < \alpha < 57$ deg for $A_p = 3$ deg. For the same reason, this range becomes smaller for a plate amplitude of $A_p = 12$ deg, where the object easily becomes unstable or folded in half, as pointed out in the previous section. As a result, it can only deal with friction angles in the range of $24 < \alpha < 41$ deg.

5.6 Validation of the Proposed Method

In this section we show the simulation and experimental results of the real parameters against the estimated ones to confirm the validity of the proposed method.

5.6.1 Simulation Results

Using the simulation data of Fig. 5.7 and Fig. 5.9, the parameters obtained from the linear regression are $p_1 = 5.30$, $q_1 = -121.62$ for $A_p = 3$ deg, and $p_1 = 5.65$, $q_1 = -64.51$ for $A_p = 12$ deg in equation (5.6); and $p_2 = 545.02$, $q_2 = -74.71$ for $A_p = 3$ deg, and $p_2 = 379.24$, $q_2 = -54.10$ for $A_p = 12$ deg in equation (5.7). Using these parameters

Table 5.1: Parameters estimated by using equations (5.6) and (5.7) for $\omega_n = 3.5\pi$ rad/s and $A_p = 3$ deg.

ω_n [π rad/s]			α [deg]		
Real ω_n	Estimated $\hat{\omega}_n$	Absolute Error	Real α	Estimated $\hat{\alpha}$	Absolute Error
3.5	3.19	0.31	24.23	28.94	4.71
3.5	3.10	0.40	33.02	37.14	4.12
3.5	3.08	0.42	36.87	37.98	1.11
3.5	2.56	0.94	40.36	42.09	1.73
3.5	1.72	1.78	47.73	48.66	0.93
3.5	2.38	1.12	56.31	61.31	5.00
Average Error		0.83	Average Error		2.93

in equations (5.6) and (5.7), we estimate the object's physical parameters ω_n and α. The results are summarized in Tables 5.1–5.4 for $Ap = 3$ deg, and in Tables 5.5–5.8 for $A_p = 12$ deg. For the results with $A_p = 3$ deg, it can be observed that the estimated parameters $\hat{\omega}_n$ have the smaller average error for $\omega_n = 3.5\pi$ rad/s in Table 5.1. This can be intuitively understood from Fig. 5.7(a) as the values of f_0 for the same $\omega_n = 3.5\pi$ rad/s and different α, are very close to each other. In contrast, the values of f_0 for $\omega_n = 10\pi$ rad/s in Table 5.2, $\omega_n = 23\pi$ rad/s in Table 5.3 and $\omega_n = 33\pi$ rad/s in Table 5.4 have dispersion, thus their average error is larger than that of $\omega_n = 3.5\pi$ rad/s in Table 5.1. Likewise, for $A_p = 12$ deg it can be observed from Fig. 5.7(b) that for $\omega_n = 1.4\pi$ rad/s and $\omega_n = 3.5\pi$ rad/s most of their corresponding values of f_0 are close to the regression line, while those for $\omega_n = 6.5\pi$ rad/s and $\omega_n = 10\pi$ rad/s are not as close as the previous ones. Therefore the smallest errors are for the estimated parameters in Table 5.5 and 5.6. In the case of the estimated $\hat{\alpha}$ for $A_p = 3$ deg, as seen in Fig. 5.9(a), the values of b/f_0 for $\omega_n = 3.5\pi$ rad/s are separated from those of $\omega_n = 10\pi$ rad/s, $\omega_n = 23\pi$ rad/s and $\omega_n = 33\pi$ rad/s, as a result the error in estimating $\hat{\alpha}$ for $\omega_n = 3.5\pi$ rad/s in Table 5.1 is larger than the others, nevertheless the average error is still less than 4 deg. In the case of $A_p = 12$ deg, from Fig. 5.9(b) it can be seen that the values of b/f_0 are closer to the regression line than those for $A_p = 3$ deg, as a result the average error is less than 2 deg.

In Fig. 5.11, the real ω_n and the estimated $\hat{\omega}_n$ values of Tables 5.1–5.4, and Tables 5.5–5.8 are shown for $A_p = 3$ deg in (a) and $A_p = 12$ deg in (b), respectively. In this figure, ω_n denotes the object's natural bending frequency given to the simulation model and $\hat{\omega}_n$ denotes the estimated one using equation (5.6). The solid line is the

Table 5.2: Parameters estimated by using equations (5.6) and (5.7) for $\omega_n = 10\pi$ rad/s and $A_p = 3$ deg.

ω_n [π rad/s]			α [deg]		
Real ω_n	Estimated $\hat{\omega}_n$	Absolute Error	Real α	Estimated $\hat{\alpha}$	Absolute Error
10.0	11.89	1.89	24.23	23.64	0.59
10.0	11.30	1.30	33.02	30.83	2.19
10.0	11.20	1.20	36.87	35.52	1.35
10.0	12.12	2.12	40.36	39.38	0.98
10.0	10.18	0.18	47.73	45.29	2.44
10.0	8.71	1.29	56.31	54.37	1.94
Average Error		1.33	Average Error		1.58

Table 5.3: Parameters estimated by using equations (5.6) and (5.7) for $\omega_n = 23\pi$ rad/s and $A_p = 3$ deg.

ω_n [π rad/s]			α [deg]		
Real ω_n	Estimated $\hat{\omega}_n$	Absolute Error	Real α	Estimated $\hat{\alpha}$	Absolute Error
23.0	24.40	1.40	24.23	25.94	1.71
23.0	23.56	0.56	33.02	35.37	2.35
23.0	23.51	0.51	36.87	40.65	3.78
23.0	23.63	0.63	40.36	42.90	2.54
23.0	24.47	1.47	47.73	43.87	3.86
23.0	25.10	2.10	56.31	52.26	4.05
Average Error		1.11	Average Error		3.05

Table 5.4: Parameters estimated by using equations (5.6) and (5.7) for $\omega_n = 33\pi$ rad/s and $A_p = 3$ deg.

ω_n [π rad/s]			α [deg]		
Real ω_n	Estimated $\hat{\omega}_n$	Absolute Error	Real α	Estimated $\hat{\alpha}$	Absolute Error
33.0	30.78	2.22	24.23	24.69	0.46
33.0	30.06	2.94	33.02	30.17	2.85
33.0	32.09	0.91	36.87	32.00	4.89
33.0	33.56	0.56	40.36	45.24	4.88
33.0	31.79	1.21	47.73	41.74	5.99
33.0	32.59	0.41	56.31	54.03	2.28
Average Error		1.37	Average Error		3.56

result of the linear regression of the real data and the estimated one, and the dashed lines are the 95% confidence intervals of the regression line, i.e., if we take some extra data and added it to this plot, there is a 0.95 probability that the new regression line

Table 5.5: Parameters estimated by using equations (5.6) and (5.7) for $\omega_n = 1.4\pi$ rad/s and $A_p = 12$ deg.

ω_n [π rad/s]			α [deg]		
Real ω_n	Estimated $\hat{\omega}_n$	Absolute Error	Real α	Estimated $\hat{\alpha}$	Absolute Error
1.40	1.20	0.20	24.23	22.47	1.76
1.40	1.28	0.12	28.81	29.33	0.52
1.40	1.55	0.15	33.02	34.09	1.07
1.40	2.06	0.66	36.87	35.86	1.01
1.40	1.33	0.07	40.36	38.07	2.29
Average Error		0.24	Average Error		1.33

Table 5.6: Parameters estimated by using equations (5.6) and (5.7) for $\omega_n = 3.5\pi$ rad/s and $A_p = 12$ deg.

ω_n [π rad/s]			α [deg]		
Real ω_n	Estimated $\hat{\omega}_n$	Absolute Error	Real α	Estimated $\hat{\alpha}$	Absolute Error
3.50	3.46	0.04	24.23	24.60	0.37
3.50	3.58	0.08	28.81	31.87	3.06
3.50	3.67	0.17	33.02	33.79	0.77
3.50	3.36	0.14	36.87	37.53	0.66
3.50	3.96	0.46	40.36	39.16	1.20
Average Error		0.18	Average Error		1.21

Table 5.7: Parameters estimated by using equations (5.6) and (5.7) for $\omega_n = 6.5\pi$ rad/s and $A_p = 12$ deg.

ω_n [π rad/s]			α [deg]		
Real ω_n	Estimated $\hat{\omega}_n$	Absolute Error	Real α	Estimated $\hat{\alpha}$	Absolute Error
6.50	5.86	0.64	24.23	22.66	1.57
6.50	7.67	1.17	28.81	31.04	2.23
6.50	6.15	0.35	33.02	34.64	1.62
6.50	7.72	1.22	36.87	35.79	1.08
6.50	5.90	0.60	40.36	38.21	2.15
Average Error		0.80	Average Error		1.73

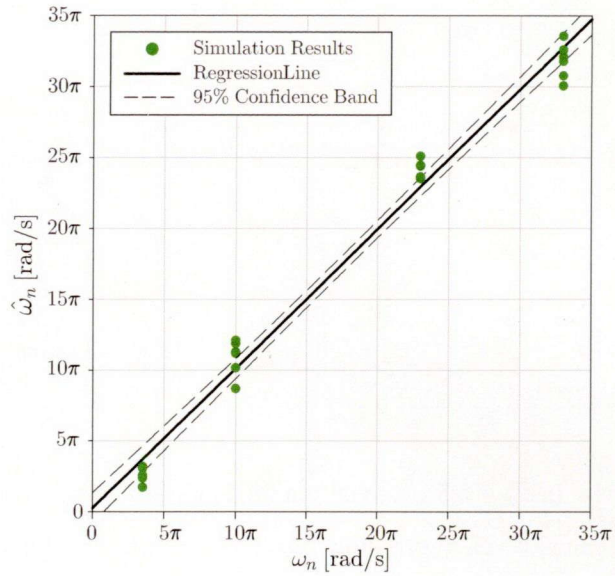
including this newly added data, would be somewhere between this confidence intervals. In Fig. 5.11(a), it can be seen that the estimated values are close to the real ones, the coefficient of determination is $R^2 = 0.99$. The regression line should ideally have a unit slope and an intercept of zero, that is the estimated value is identical to the real one. In this case, it has a slope of 0.99 and an intercept of 0.25, which are close to their

Table 5.8: Parameters estimated by using equations (5.6) and (5.7) for $\omega_n = 10\pi$ rad/s and $A_p = 12$ deg.

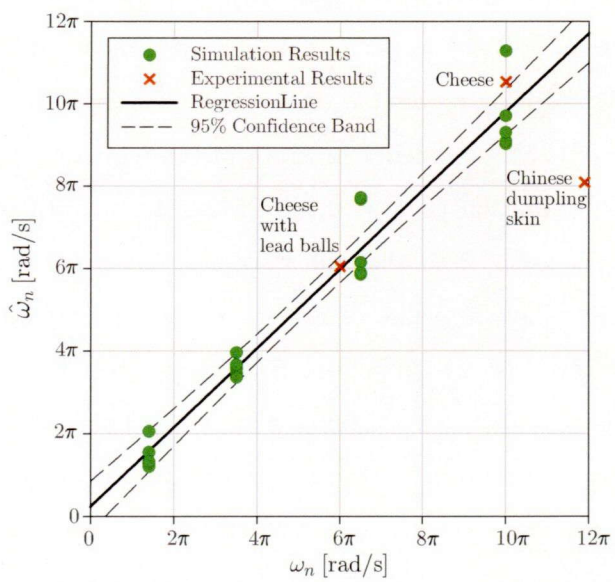
ω_n [π rad/s]			α [deg]		
Real ω_n	Estimated $\hat{\omega}_n$	Absolute Error	Real α	Estimated $\hat{\alpha}$	Absolute Error
10.0	9.02	0.98	24.23	23.17	1.06
10.0	9.09	0.91	28.81	29.53	0.72
10.0	9.30	0.70	33.02	34.91	1.89
10.0	11.28	1.28	36.87	37.04	0.17
10.0	9.70	0.30	40.36	39.48	0.88
Average Error		0.83	Average Error		0.94

ideal values. Similarly, in Fig. 5.11(b) the coefficient of determination is $R^2 = 0.96$ for $A_p = 12$ deg. In this case, the regression line has a slope of 0.96 and an intercept of 0.24, which are also close to their ideal values.

In Fig. 5.12, the real α and the estimated $\hat{\alpha}$ values of Tables 5.1–5.4, and Tables 5.5–5.8 are shown for $A_p = 3$ deg in (a) and $A_p = 12$ deg in (b), respectively. The solid line is the result of the linear regression of the real data and the estimated one, and the dashed lines are the 95% confidence intervals of the regression line. In Fig. 5.12(a), the coefficient of determination is $R^2 = 0.90$ and has a slope of 0.89 and an intercept of 4.15, which may seem far from their ideal values. Despite of this fact, by means of the t-test we verify that the value of the slope does not significantly differs from 1 (for details about this test see Appendix B), as the t-test result is $t_{s0} = 1.70$ (for $df = 22$) that yields $p = 0.1028$, satisfying $p > 0.05$. This indicates that the slope does not significantly differs from 1. For the intercept, we verify that its value does not significantly differs from zero, as $t_{i0} = 1.57$ (for $df = 22$) which yields $p = 0.1298$, also satisfies $p > 0.05$, meaning that the intercept does not significantly differs from zero. In the same way, in Fig. 5.12(b) the coefficient of determination is $R^2 = 0.93$ and has a slope of 0.93 and an intercept of 2.25. The t-test for the slope is $t_{s1} = 1.16$ (for $df = 18$) which yields $p = 0.2620$, satisfying $p > 0.05$, indicating that the slope does not significantly differs from 1. For the intercept, the t-test result is $t_{i1} = 1.14$ (for $df = 18$) which yields $p = 0.2681$, also satisfying $p > 0.05$, meaning that the intercept does not significantly differs from zero.

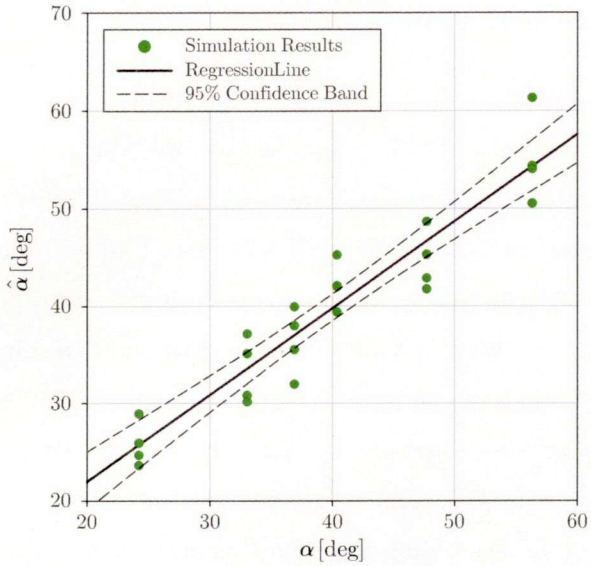


(a)

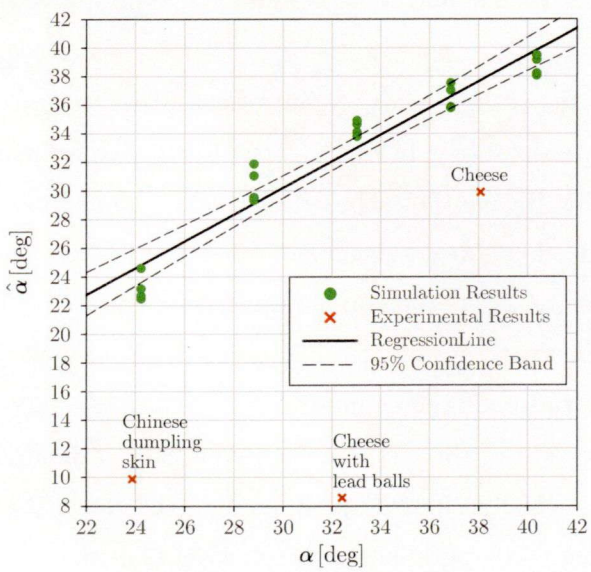


(b)

Figure 5.11: Linear regression between the object's real ω_n (first-order natural angular frequency in bending) and the estimated $\hat{\omega}_n$ obtained by using equation (5.6). Simulation results for $A_p = 3$ deg in (a) and simulation and experimental results for $A_p = 12$ deg in (b). The solid line represents the regression line and the dashed lines are the 95% confidence intervals.



(a)



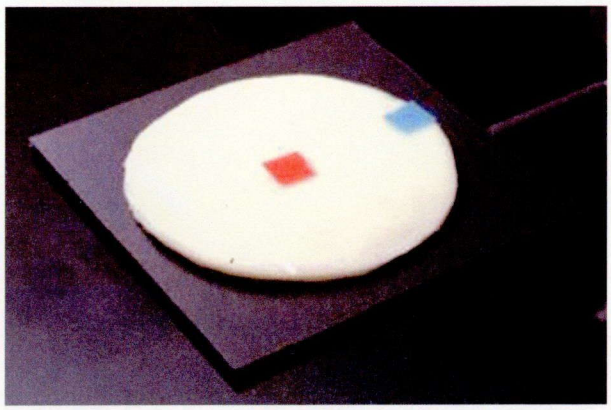
(b)

Figure 5.12: Linear regression between the real friction angle α and the estimated $\hat{\alpha}$ obtained by using equation (5.7). Simulation results for $A_p = 3$ deg in (a) and simulation and experimental results for $A_p = 12$ deg in (b). The solid line represents the regression line and the dashed lines are the 95% confidence intervals.

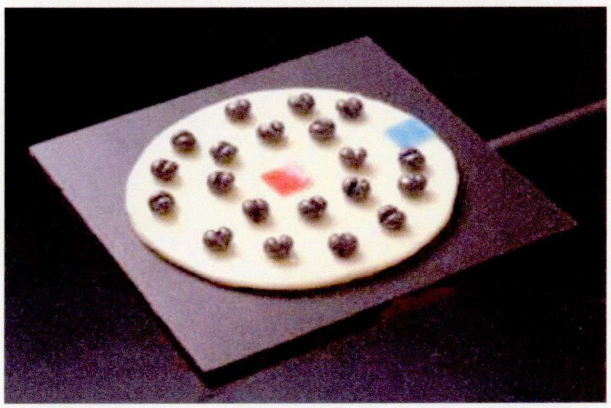
5.6.2 Experimental Results

To validate the proposed method we carried out experiments with a commercially available slice of cheese, a slice of cheese with lead balls that were used to increase the weight of the cheese and the skin of a Chinese dumpling. The three objects shown in Fig. 5.13 have the same circular shape with a radius of 40 mm, and the masses of the cheese, the cheese with lead balls and the skin of Chinese dumpling are 13.6 g, 39.5 g, and 6.9 g, respectively. Fig. 5.14 shows the experimental results of the relationship between the object's angular velocity ω_B and the plate's motion frequency f_p, for the three deformable objects described above, when the plate's motion is given by $A_p = 12$ deg and $B_p = 3$ mm. The solid line represents the regression line for equation (5.5). From Fig. 5.14 it can be seen that the experimental values can be described by its corresponding regression line, since $R^2 = 0.98$ for the slice of cheese, $R^2 = 0.99$ for the slice of cheese with lead balls, and $R^2 = 0.98$ for the skin of a Chinese dumpling, were obtained.

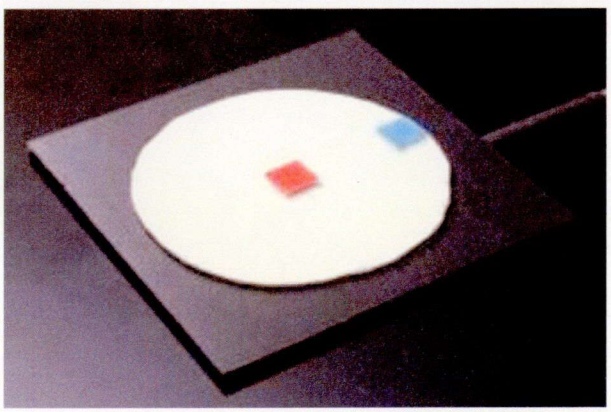
The real ω_n and the estimated $\hat{\omega}_n$ values of the experimental data are overlapped on the simulation data, as shown in Fig. 5.11(b). In the experimental results, as a real value of ω_n, we employ the cantilever based method explained in section 3.3 utilizing a piece of cut food and a high-speed vision system of 400 fps to measure this parameter. The estimated parameter $\hat{\omega}_n$ is the one obtained from equation (5.6) in the same way as with the simulation data. From Fig. 5.11(b), it can be seen that for the plain cheese and the cheese with lead balls the estimated value of ω_n has an error of $\approx 0.5\pi$ rad/s, while the one for the skin of the Chinese dumpling is of $\approx 3.8\pi$ rad/s. The latter has an $\omega_n = 11.9\pi$ rad/s which is in the upper limit of the range that can be dealt with, and the largest among the experimental objects. Being in the upper limit of the range may be the cause of the increase in the error of the estimated value $\hat{\omega}_n$. In this case, the slice of cheese and the skin of the Chinese dumpling have similar natural bending frequencies. However, the skin of the Chinese dumpling is lighter than the slice of cheese, which suggests that the skin of the Chinese dumpling has a bending stiffness smaller than the one of the cheese. In contrast, the slice of cheese with lead balls, has a smaller bending frequency than the one for the plain slice of cheese. This was expected as the lead balls increased the weight of the cheese, thus altering its mass-elasticity



(a) Slice of Cheese



(b) Slice of Cheese with lead balls



(c) Skin of a Chinese dumpling

Figure 5.13: Pictures of the deformable objects used in experiment.

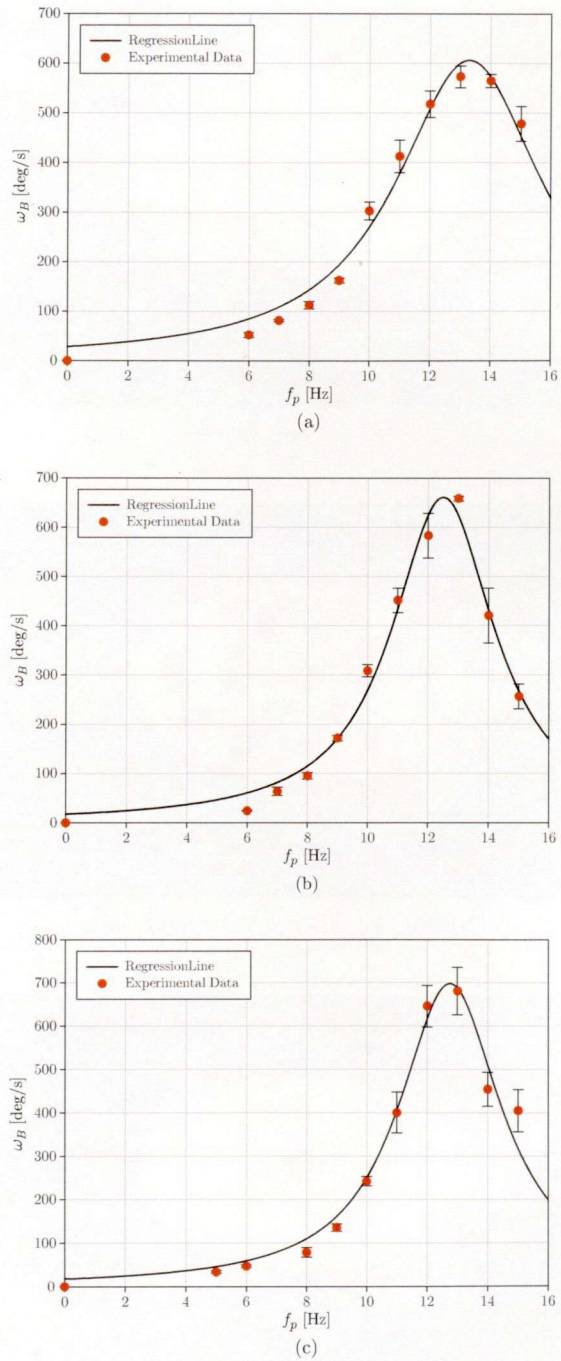


Figure 5.14: Relationship between the object's angular velocity ω_B and the plate's motion frequency f_p, for (a) a slice of cheese, (b) a slice of cheese with lead balls and (c) the skin of a Chinese dumpling, with $A_p = 12$ deg and $B_p = 3$ mm.

ratio. Like this, the object's natural angular frequency in bending ω_n can be used as an stiffness index for a known mass object.

The real α and the estimated $\hat{\alpha}$ values of the experimental data are overlapped on the simulation data, as shown in Fig. 5.12(b). In the experimental results, as a real value of α, we measure the angle of the inclined plate at which the object begins to slip from it, employing the same object used for the rotational motion experiment and a vision system to measure this parameter. The estimated parameter $\hat{\alpha}$ is the one obtained from equation (5.7) in the same way as with the simulation data. From Fig. 5.12(b), it can be seen that the friction angle estimated for the plain cheese has the smaller error ≈ 8.2 deg, while the error for the cheese with lead balls and the skin of the Chinese dumpling are ≈ 24 and ≈ 14 deg, respectively. Although the errors for the cheese with lead balls and the skin of the Chinese dumpling are about the value of the friction angle itself, it can be observed that there is a difference between their estimated values and that of the plain cheese. One possible cause may be the fluctuating friction angle in the experiments. Since we are dealing with food, it is difficult to keep constant the same conditions as in simulation. Also, we have not consider the influence of the dynamic coefficient of friction. We supposed a constant value for $\beta = \mu_k/\mu_s$ in the simulation analysis which is the case of the plain cheese, however, it may not necessarily be the case for the other two deformable objects. This may be overcome by analyzing and considering the influence of β, and by approximating the results of Fig. 5.9 by a quadratic equation instead of the linear equation (5.7) used for the sake of simplicity, sacrificing precision in the estimation of the friction between the object and the plate.

5.7 Discussion

As mentioned earlier in Section 5.1, a high frequency of the object's bending vibration is converted to a rotating motion of low frequency . The object's frequency of rotation f_B on the plate can be obtained from the object's maximal angular velocity $\omega_{Br\,\max}$ in Fig. 5.6, for each of the four deformable objects and each of the two plate amplitudes A_p used in this chapter. The results of f_B are shown in Table 5.9, where the object's bending vibration frequency f_n which corresponds with ω_n is also shown. It should be noted that especially for the deformable object of $\omega_n = 33\pi$ rad/s, its bending vibration

Table 5.9: Object's first-order natural frequency in bending and its rotation frequency.

A_p [deg]	ω_n [π rad/s]	f_n [Hz]	$\omega_{Br\,\max}$ [deg/s]	f_B [Hz]
3	3.50	1.75	491.5	1.36
	10.0	5.00	614.9	1.71
	23.0	11.5	722.8	2.01
	33.0	16.5	796.1	2.21
12	1.40	0.70	278.1	0.77
	3.50	1.75	275.8	0.77
	6.50	3.25	334.2	0.93
	10.0	5.00	382.4	1.06

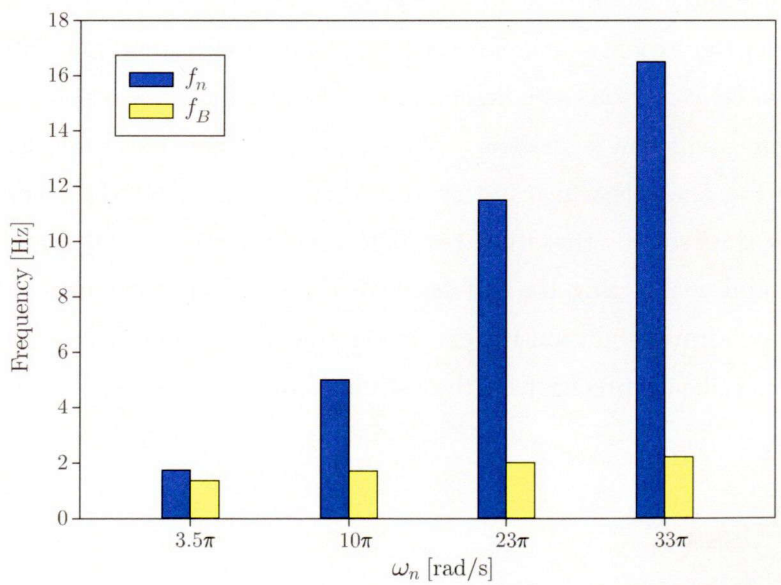


Figure 5.15: Comparison between the object's bending vibration frequency f_n and its frequency of rotation f_B for $A_p = 3$ deg and $B_p = 3$ mm.

frequency of $f_n = 16.5$ Hz is converted into a rotational motion with a frequency of $f_B = 2.21$ Hz, for $A_p = 3$ deg, as illustrated in Fig. 5.15. This represents only the 13.4% of the object's bending frequency f_n. Thus, the object's first-order natural angular frequency in bending ω_n can be measured through the object's dynamic behavior, observing its

low-frequency rotation motion f_B and equation (5.6), by using the manipulation scheme presented in this dissertation. For now we have only considered objects of the same size. However, in the future we would like to considered and analyzed the effect of the size of the object, so that the proposed method can be applied to any sized objects. This may be achieved by adding an extra parameter to the expression of the object's angular velocity.

5.8 Summary

In this chapter, the estimation of two physical parameters of the object was discussed. It was shown that the line shape of the angular velocity of the object with respect to the plate's motion frequency has a resonance-like behavior. Based on this nature, it was demonstrated that the object's angular velocity transition can be represented with a simple mathematical expression like the Lorentz distribution one, instead of a complex expression derived from the dynamics of the system. From the Lorentz-based curve fitting, it was found out that the frequency of resonance at which the object's maximal angular velocity occurs, depends on the first-order natural angular frequency in bending of the object, and that the characteristic width of the Lorentzian curve describing the object's angular velocity depends on the friction between the object and the plate. Based on this relationship, a method to estimate two physical parameters of the object from the regression parameters of the Lorentzian curve fitting was proposed. The validity of the proposed method was verified through simulation and experimental results.

Chapter 6

Conclusion

6.1 Conclusion

The aim of this dissertation was to develop a dynamic nonprehensile manipulation strategy to manipulate a thin deformable object by actively using its dynamic behavior caused by high-speed motions of a vibrating plate. We formulated two questions in Chapter 1. The first one was: What does actually happen when a deformable object is placed on a high-speed plate? The answer to this question is that, the object is considerably deformed by the high-speed motions of the plate, which allows the object to rotate faster. The object's angular velocity increases as the plate's motion frequency increases, and its rotational behavior is similar to a biped's gait sliding, walking and running, where the running gait is the fastest and dynamically stable. The second question was: Is there any effective strategy to manipulate the object and which is? The answer is that, there is an effective strategy to manipulate the object, and it is to generate the running gait of the object with the optimal plate's angular acceleration so that the object can run and rotate faster. The results of this dissertation are summarized below.

In chapter 1, we explained the background and goal of this dissertation, and we introduced the related works to dynamic and nonprehensile manipulation, as well as the manipulation of deformable objects.

In chapter 2, we explained the guideline for the design of the experimental system and discussed why we use a two-DOFs plate in the nonprehensile manipulation scheme. This two-DOFs plate scheme allowed us to manipulate remotely the object with less

environmental limitations than the typical nonprehensile manipulation, and without increasing the inertial loads applied to the handling location. The combination of a translational motion with a rotational motion generates the rotational moment that enabled the object to rotate on the plate. We showed how a deformable object rotates faster than a rigid one on the plate through basic experiments. Its bending motion generated by the plate's rotational motion reduces the braking moment, thus contributing to a faster and more stable rotation than the one for a rigid object.

In chapter 3, we introduced a simulation model to approximate the dynamic behavior of a deformable object. This model is composed of multiple mass nodes and joint units, where the joint units have three DOFs: bending, tension/compression and torsion. The bending and the tension/compression joints have viscoelastic elements given by a Kelvin–Voigt model while the torsion joint was left free for simplicity of the model. We explained the models used for experimentally estimating these viscoelastic parameters, and we showed the experimental results of these parameters estimation for a food product. Finally, we showed that the reconstructed data by simulation using the estimated parameters were consistent with the experimental data for both the bending and the tension/compression joints parameters.

In chapter 4, we discussed the optimal problem to produce the fastest object's rotation. We showed the simulation and experimental results to validate the introduced model. These results showed that the dynamic behavior in both simulation and experiment corresponded qualitatively to each other. By means of simulation analysis, we discovered that the transition of the object's rotational behavior with respect to the plate's frequency resembles either a sliding, walking, or running gait of a biped. We obtained the optimal plate motion leading to the object's maximal angular velocity, and we revealed that the angular acceleration of the plate is the most important factor for a dynamically stable and fast object rotation. Finally, we showed that the optimal coefficient of friction that yields the object's maximal angular velocity exists, and that it depends on the gait type of the object.

In chapter 5, we discussed the estimation of physical parameters of an object by a nonprehensile approach. We showed that the line shape of the object's angular velocity with respect to the plate's frequency has a resonance-like behavior. Based on this nature, we showed that the object's angular velocity transition can be represented with a simple mathematical expression like the Lorentz distribution one, instead of a

complex expression derived from the dynamics of the system. We found out that two physical parameters: the object's first-order natural angular frequency in bending and the friction between the object and the plate dominate the Lorentzian curve characteristics. We proposed how to estimate these two physical parameters of the object by employing the regression parameters of the Lorentzian curve fitting. The validity of the proposed method was verified through simulation and experimental results.

6.2 Future Work

The manipulation scheme used in this dissertation has still a number of possible developments. We will limit to the ones closest to this dissertation.

First, we focus on the manipulation of deformable objects by a nonprehensile scheme. The influence of the thickness, the size and the shape of the object in its gait-like rotational behavior should be investigated, as we supposed that the object's thickness is thin enough to be negligible and we only used circular shaped objects of the same size. Also, the accuracy of the simulation model may be improved by introducing viscoelastic elements to the torsion joint of the viscoelastic joint unit. Then, we should analyze its influence in the object's gait-like rotational behavior. The gait-like motion found and discussed in this dissertation is just one example of dynamic phenomena, and the strategies for other motions may be found based on this example. The behavior of the object may be further exploited by changing the sinusoidal wave's phase and period combination of the translational and rotational motions of the plate. Consequently, the object's locomotion may become diverse, such as taking steps forward, back, and turning. A flexible object with no active muscles nor actuators may move just as if it were a living creature and it may become the optimal solution for some particular task(s).

Through this work an analogy to bipedal gaits was discovered. The object's behavior similar to a running gait is useful for achieving high-speed rotations, and the best strategy for generating this behavior is to control the plate's motion. However, we have new questions, why does the object's behavior looks like a bipedal gait? Was this a coincidence or is there a logic in this behavior? Does this analogy exists only in appearance or does it exists also in dynamics? In the future we would like to answer these questions. This may be achieved by carrying out the dynamical analysis of the entire system. Then, we may found the dynamical analogy to bipedal gaits. Also, it

may be possible to construct the nonlinear system and resolved it from the viewpoint of control theory, thus finding the input motions of the plate needed to generate the desired locomotion of the object, and may found unforeseen motion strategies. This kind of manipulation may be used toward the simultaneous control of the position and orientation of deformable objects, which may be employed as a parts feeder or sorter for delicate and/or deformable objects.

On the other hand, focusing on the sensing of deformable objects by a nonprehensile scheme, the influence of the dynamic friction and the role of viscosity in the object's resonance-like behavior needs to be investigated. Then, it may be possible to evaluate the mass, elasticity, viscosity and friction of several deformable objects by characterizing its rotational behavior on a simple flat plate considering not only the object's first-order natural frequency of vibration but also higher orders. The proposed nonprehensile manipulation approach for sensing the physical parameters of an object may be applicable to the evaluation of freshness and texture of food, which alter the bending frequency of food, as illustrated in Fig. 6.1. Also, since this manipulation scheme can prevent a large concentration of stress, it is expected to significantly contribute to the cell/tissue processing technology in the bioscience research. A change in tissue stiffness could be an indicator of some diseases such as cancer. The bending frequency of the method proposed may be used as a stiffness evaluation index. Like this, the nonprehensile manipulation approach discussed in this dissertation may be considered for applications in the industrial, medical and biological fields.

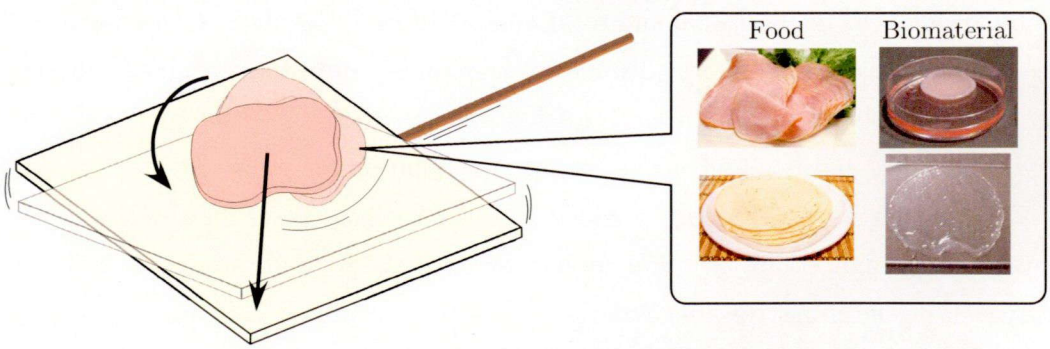


Figure 6.1: Future applications. The nonprehensile approach discussed in this dissertation may be employed for manipulating delicate and/or deformable objects. For example food products and biomaterials, in a parts feeder or sorter in the industrial sector. Also it may be applicable to evaluate freshness and texture of food, as well as to evaluate the stiffness of biomaterials.

Appendix A

Coefficients of Determination

In this section, we summarized the coefficients of determination of the nonlinear regressions of the data in Fig. 5.5. In Table A.1 for the data of Fig. 5.5(a) for $A_p = 3$ deg and in Table A.2 for the data of Fig. 5.5(b) for $A_p = 12$ deg. From these tables it can be confirm that the object's angular velocity line shape fits into the Lorentz distribution given by equation (5.5).

Table A.1: Coefficients of determination for $A_p = 3$ deg.

ω_n [rad/s]	α [deg]	R^2
3.5π	24.23	0.98
	33.02	0.99
	36.87	0.99
	40.36	0.99
	47.73	0.99
	56.31	0.98
23π	24.23	0.99
	33.02	0.99
	36.87	0.99
	40.36	0.99
	47.73	0.99
	56.31	0.99

ω_n [rad/s]	α [deg]	R^2
10π	24.23	0.99
	33.02	0.99
	36.87	0.99
	40.36	0.99
	47.73	0.99
	56.31	0.98
33π	24.23	0.98
	33.02	0.99
	36.87	0.99
	40.36	0.99
	47.73	0.99
	56.31	0.97

Table A.2: Coefficients of determination for $A_p = 12$ deg.

ω_n [rad/s]	α [deg]	R^2
1.4π	24.23	0.99
	28.81	0.98
	33.02	0.98
	36.87	0.98
	40.36	0.97
6.5π	24.23	0.99
	28.81	0.99
	33.02	0.99
	36.87	0.99
	40.36	0.98

ω_n [rad/s]	α [deg]	R^2
3.5π	24.23	0.99
	28.81	0.99
	33.02	0.98
	36.87	0.99
	40.36	0.97
10π	24.23	0.99
	28.81	0.99
	33.02	0.98
	36.87	0.98
	40.36	0.99

Appendix B

t Statistic Test

Here it is explained how we calculated the t statistic test.

Brief Introduction to the t-test

Suppose we have the following equation:

$$y = mx + b \tag{B.1}$$

where x is the independent variable, y is the dependent variable, and the regression coefficients m and b are the slope and the intercept, respectively. The values of m and b are obtained from the linear regression analysis of $\hat{x}$ and $\hat{y}$ that are the observations fitted in equation (B.1). The t statistic test is usually employed to verify whether the coefficient of the independent variable is zero or not; when its value is zero, this means the independent variable does not contribute to predicting the dependent variable. However, this test can also be employed to know whether the regression coefficient is equal to a given value or not, this is known as hypothesis testing in linear regression analysis and it assumes that the errors (the difference between $\hat{y}$ and y) are normally distributed[104], for example if we want to verify whether $m = \delta$ or not, the hypothesis are

$$\begin{aligned} H_0 &: m = \delta \\ H_1 &: m \neq \delta \end{aligned} \tag{B.2}$$

where H_0 and H_1 are mutually exclusive. The t-test is calculated as[104]:

$$t = \frac{|m - \delta|}{\sqrt{MS_E/S_{xx}}} \tag{B.3}$$

where MS_E is the residual mean square and S_{xx} is the corrected sum of squares of the least square estimation of the slope and the intercept.

From the value of t we can calculate the value of p which is the probability that the hypothesis H_0 is correct. Typically the threshold value of p used to determine that H_0 is correct, is $p > 0.05$[105]. This probability can be obtained from the t distribution tables found in books or using the predetermined functions in computer programs such as Excel, SigmaPlot, etc. This distribution has different values depending on the number of variables and the number of observations N of the regression. For this reason it is necessary to specify this number, which is usually known as the degrees of freedom (df) and it is calculated as

$$df = \text{number of observations} - \text{number of parameters in the equation} \ ,$$

in this case $df = N - 2$, since we have only two parameters: the slope and the intercept.

Obtaining the Value of t

In this dissertation we carried out the linear regression of the real values of the friction angle α versus the estimated ones $\hat{\alpha}$ to verify that the estimation method proposed is valid. In this case, as explained in chapter 5, the ideal regression line between α and $\hat{\alpha}$ would be with $m = 1$ and $b = 0$. Therefore, we are interested in knowing which of the next hypothesis is correct

$$\begin{aligned} H_{b0} &: b = 0 \\ H_{b1} &: b \neq 0 \\ H_{m0} &: m = 1 \\ H_{m1} &: m \neq 1 \end{aligned} \tag{B.4}$$

where H_{b0} and H_{b1} are for testing whether the intercept is zero or not, and H_{m0} and H_{m1} are for testing whether the slope is one or not.

For the linear regression analysis, we employ the software Sigmaplot (Systat Software, Inc.), from which we obtained the value of t for both the slope and the intercept when $\delta = 0$ in equation (B.3), as well as the value of p associated with t. This values are summarized in Table B.1. Thus, the verification of the hypothesis H_{b0} and H_{b1} can be done immediately from the values of p in Table B.1, which confirm that the value of the intercept is zero or that it does not differ from zero.

Table B.1: Regression Analysis Parameters.

$A_p = 3$ deg	$m_0 = 0.89$	$t_0 = 13.88$	$p < 0.0001$	$df = 22$
	$b_0 = 4.15$	$t_{i0} = 1.57$	$p = 0.1298$	$df = 22$
$A_p = 12$ deg	$m_1 = 0.93$	$t_1 = 15.65$	$p < 0.0001$	$df = 18$
	$b_1 = 2.25$	$t_{i1} = 1.14$	$p = 0.2681$	$df = 18$

Table B.2: Calculated values of t and its associated p.

$A_p = 3$ deg	$m_0 = 0.89$	$t_{s0} = 1.70$	$p = 0.1028$	$df = 22$
$A_p = 12$ deg	$m_1 = 0.93$	$t_{s1} = 1.16$	$p = 0.2620$	$df = 18$

For the slope, we rewrite equation (B.3) as

$$t_s = \frac{|m - 1|}{\varepsilon} \tag{B.5}$$

and noticing that the values of t_0 and t_1 in Table B.1 are for $\delta = 0$ in equation (B.3), we obtained ε_0 and ε_1 as

$$\begin{aligned} \varepsilon_0 &= \frac{m_0}{t_0} \\ \varepsilon_1 &= \frac{m_1}{t_1} \end{aligned} \tag{B.6}$$

for the slope m_0 and m_1, respectively. We calculated t_{s0} and t_{s1} to corroborate which of the hypothesis H_{m0} or H_{m1} is correct, as

$$\begin{aligned} t_{s0} &= \frac{|m_0 - 1|}{\varepsilon_0} \\ t_{s1} &= \frac{|m_1 - 1|}{\varepsilon_1} \end{aligned} \tag{B.7}$$

The results are summarized in Table B.2, where the values of p were obtained with the function TDIST of Excel. From the values of p it can be concluded that the values of both slopes m_0 and m_1 do not differ from one, that is, hypothesis H_{m0} is truth for both slopes.

APPENDIX B

References

1) H. Arai and O. Khatib, "Experiments with dynamic skills," in *Proceedings of 1994 Japan-USA Symposium on Flexible Automation*, Kyoto, Japan, July 1994, pp. 81–84.

2) K. F. Böhringer, B. Donald, R. Mihailovich, and N. C. MacDonald, "Sensorless manipulation using massively parallel microfabricated actuator arrays," in *Proceedings of the IEEE International Conference on Robotics and Automation*, vol. 1, San Diego, CA, USA, May 1994, pp. 826–833.

3) K. F. Böhringer, V. Bhatt, and K. Goldberg, "Sensorless manipulation using transverse vibrations of a plate," in *Proceedings of the IEEE International Conference on Robotics and Automation*, vol. 2, Nagoya, Japan, 1995, pp. 1989–1996.

4) K. F. Böhringer, K. Goldberg, M. Cohn, R. Howe, and A. Pisano, "Parallel microassembly with electrostatic force fields," in *Proceedings of the IEEE International Conference on Robotics and Automation*, vol. 2, Leuven, Belgium, May 1998, pp. 1204–1211.

5) K. F. Böhringer, V. Bhatt, B. R. Donald, and K. Goldberg, "Algorithms for sensorless manipulation using a vibrating surface," *Algorithmica*, vol. 26, no. 3-4, pp. 389–429, 2000.

6) N. B. Zumel and M. A. Erdmann, "Nonprehensile two palm manipulation with non-equilibrium transitions between stable states," in *Proceedings of the IEEE International Conference on Robotics Automation*, vol. 4, Minneapolis, MN, USA, April 1996, pp. 3317–3323.

7) ——, "Nonprehensile manipulation for orienting parts in the plane," in *Proceedings of the IEEE International Conference on Robotics Automation*, vol. 3, Albuquerque, NM, USA, April 1997, pp. 2433–2439.

8) K. M. Lynch and M. T. Mason, "Dynamic underactuated nonprehensile manipulation," in *Proceedings of the IEEE/RSJ International Conference on Intelligent Robots and Systems*, vol. 2, Osaka, Japan, November 1996, pp. 889–896.

9) ——, "Dynamic manipulation with a one joint robot," in *Proceedings of the IEEE International Conference on Robotics Automation*, vol. 1, Albuquerque, NM, USA, April 1997, pp. 359–366.

10) K. M. Lynch, N. Shiroma, H. Arai, and K. Tanie, "The roles of shape and motion in dynamic manipulation, the butterfly example," in *Proceedings of the IEEE International Conference on Robotics and Automation*, vol. 3, Leuven, Belgium, May 1998, pp. 1958–1963.

11) K. M. Lynch and M. T. Mason, "Dynamic nonprehensile manipulation: controllability, planning, and experiments," *The International Journal of Robotics Research*, vol. 18, no. 1, pp. 64–92, January 1999.

12) D. Reznik and J. Canny, "The coulomb punp: a novel parts feeding method using a horizontally vibrating surface," in *Proceedings of the IEEE International Conference on Robotics Automation*, vol. 1, Leuven, Belgium, May 1998, pp. 869–874.

13) ——, "A flat rigid plate is a universal planar manipulator," in *Proceedings of the IEEE International Conference on Robotics and Automation*, vol. 2, Leuven, Belgium, May 1998, pp. 1471–1477.

14) D. Reznik, E. Moshkovich, and J. Canny, "Building a universal planar manipulator," in *Proceedings Workshop on Distributed Manipulation at the International Conference on Robotics and Automation*, Detroit, Michigan, USA, May 1999.

15) D. Reznik and J. Canny, "C'mon part, do the local motion!" in *Proceedings of the IEEE International Conference on Robotics and Automation*, vol. 3, Seoul, Korea, May 2001, pp. 2235–2242.

16) D. Reznik, J. Canny, and N. Alldrin, "Leaving on a plane jet," in *Proceedings of the IEEE/RSJ International Conference on Intelligent Robots and Systems*, vol. 1, Maui, Hawaii, USA, October 2001, pp. 202–207.

17) M. Erdamann, "An exploration of nonprehensile two-palm manipulation," *The International Journal of Robotics Research*, vol. 17, no. 5, pp. 485–503, May 1998.

18) M. T. Mason, "Progress in nonprehensile manipulation," *The International Journal of Robotics Research*, vol. 18, no. 11, pp. 1129–1141, November 1999.

19) R. Šafarič, S. Uran, and K. T. Winther, "Close-loop control of rigid and flexible objects on a pneumatic active surface device," in *Proceedings of the IEEE/RSJ International Conference on Intelligent Robots and Systems*, vol. 1, Takamatsu, Japan, October 2000, pp. 486–491.

20) A. Amagai and K. Takase, "Implementation of dynamic manipulation with visual feedback and its application to pick and place task," in *Proceedings of the IEEE International Symposium on Assembly and Task Planning*, 2001, pp. 344–350.

21) W. H. Huang and G. F. Holden, "Nonprehensile palmar manipulation with a mobile robot," in *Proceedings of the IEEE/RSJ International Conference on Intelligent Robots and Systems*, vol. 1, Maui, Hawaii, USA, October 2001, pp. 114–119.

22) Y. Maeda, H. Kijimoto, Y. Aiyama, and T. Arai, "Planning of graspless manipulation by multiple robot fingers," in *Proceedings of the IEEE International Conference on Robotics Automation*, vol. 3, Seoul, Korea, May 2001, pp. 2474–2479.

23) Y. Maeda and T. Arai, "A quantitative stability measure for graspless manipulation," in *Proceedings of the IEEE International Conference on Robotics Automation*, vol. 3, Washington, DC, USA, May 2002, pp. 2473–2478.

24) ——, "Automatic determination of finger control modes for graspless manipulation," in *Proceedings of the IEEE/RSJ International Conference on Intelligent Robots and Systems*, vol. 3, Las Vegas, Nevada, USA, October 2003, pp. 2660–2665.

25) Y. Maeda, T. Nakamura, and T. Arai, "Motion planning of robot fingertips for graspless manipulation," in *Proceedings of the IEEE International Conference on Robotics Automation*, vol. 3, New Orleans, LA, USA, April 2004, pp. 2951–2956.

26) Y. Maeda and T. Arai, "Planning of graspless manipulation by a multifingered robot hand," *Advanced Robotics*, vol. 19, no. 5, pp. 501–521, 2005.

27) Y. Maeda and S. Makita, "A quantitative test for the robustness of graspless manipulation," in *Proceedings of the IEEE International Conference on Robotics Automation*, Orlando, Florida, USA, May 2006, pp. 1743–1748.

28) T. Tabata and Y. Aiyama, "Tossing manipulation by 1 degree-of-freedom manipulator," in *Proceedings of the IEEE/RSJ International Conference on Intelligent Robots and Systems*, vol. 1, Maui, Hawaii, USA, October 2001, pp. 132–137.

29) ——, "Passing manipulation by 1 degree-of-freedom manipulator -catching manipulation of tossed object without impact," in *Proceedings of the IEEE/RSJ International Conference on Intelligent Robots and Systems*, vol. 3, Las Vegas, Nevada, USA, October 2003, pp. 2920–2925.

30) P. U. Frei, "An intelligent vibratory conveyor for the individual object transportation in two dimensions," in *Proceedings of the IEEE/RSJ International Conference on Intelligent Robots and Systems*, vol. 2, Lausanne, Switzerland, October 2002, pp. 1832–1837.

31) A. Gupta and W. H. Huang, "A carrying task for nonprehensile mobile manipulators," in *Proceedings of the IEEE/RSJ International Conference on Intelligent Robots and Systems*, vol. 3, Las Vegas, Nevada, USA, October 2003, pp. 2896–2901.

32) M. Hara, Y. Tanaka, and T. Yabuta, "Dynamic manipulation of a sphere on a disk by inclination control of the disk," in *Proceedings of the IEEE International Conference on Robotics Automation*, Barcelona, Spain, April 2005, pp. 2511–2516.

33) M. Hara, Y. Tanaka, J. Huang, and T. Yabuta, "Indirect manipulation of a sphere on a flat disk using force information," *International Journal of Advanced Robotic Systems*, vol. 6, no. 4, pp. 267–276, December 2009.

34) T. Maneewarn and P. Detudom, "Mechanics of cooperative nonprehensile pulling by multiple robots," in *Proceedings of the IEEE/RSJ International Conference on Intelligent Robots and Systems*, Edmonton, Canada, August 2005, pp. 1319–1324.

35) A. Mitani, N. Sugano, and S. Hirai, "Microparts feeding by a saw-tooth surface," *IEEE/ASME Transactions on Mechatronics*, vol. 11, no. 6, pp. 671–681, December 2006.

36) A. Akbarimajd, M. N. Ahmadabadi, and B. Beigzadeh, "Dynamic object manipulation by an array of 1-dof manipulators: Kinematic modeling and planning," *Robotics and Autonomous Systems*, vol. 55, no. 6, pp. 444–459, June 2007.

37) T. H. Vose, P. Umbanhowar, and K. M. Lynch, "Vibration-induced frictional force fields on a rigid plate," in *Proceedings of the IEEE International Conference on Robotics Automation*, Roma, Italy, April 2007, pp. 660–667.

38) ——, "Friction-induced velocity fields for point parts sliding on a rigid oscillated plate," *International Journal of Robotics Research*, vol. 28, no. 8, pp. 1020–1039, August 2009.

39) ——, "Friction-induced lines of attraction and repulsion for parts sliding on a oscillated plate," *IEEE Transactions on Automation Science and Engineering*, vol. 6, no. 4, pp. 685–699, October 2009.

40) ——, "Toward the set of frictional velocity fields generable by 6-degree-of-freedom oscillatory motion of a rigid plate," in *Proceedings of the IEEE International Conference on Robotics and Automation*, Anchorage, Alaska, USA, May 2010, pp. 540–547.

41) ——, "Sliding manipulation of rigid bodies on a controlled 6-dof plate," *The International Journal of Robotics Research*, vol. 31, no. 7, pp. 819–838, 2012.

42) P. Umbanhowar and K. M. Lynch, "Optimal vibratory stick-slip transport," *IEEE Transactions on Automation Science and Engineering*, vol. 5, no. 3, pp. 537–544, July 2008.

43) P. Umbanhowar, T. Vose, A. Mitani, S. Hirai, and K. M. Lynch, "The effect of anisotropic friction on vibratory velocity fields," in *Proceedings of the IEEE International Conference on Robotics Automation*, Saint Paul, Minnesota, USA, May 2012, pp. 2584–2591.

44) W. Mori, J. Ueda, and T. Ogasawara, "1-dof dynamic pitching robot that independently controls velocity, angular velocity, and direction of a ball: contact models and motion

planning," in *Proceedings of the IEEE International Conference on Robotics Automation*, Kobe, Japan, May 2009, pp. 1655–1661.

45) U. Mettin, A. Shiriaev, G. Bätz, and D. Wollherr, "Ball dribbling with an underactuated continuous-time control phase," in *Proceedings of the IEEE International Conference on Robotics Automation*, Anchorage, Alaska, USA, May 2010, pp. 4669–4674.

46) G. Bätz, U. Mettin, A. Schmidts, M. Scheint, D. Wollherr, and A. Shiriaev, "Ball dribbling with an underactuated continuous-time control phase: Theory & experiments," in *Proceedings of the IEEE/RSJ International Conference on Intelligent Robots and Systems*, Taipei, Taiwan, October 2010, pp. 2890–2895.

47) G. Bätz, A. Yaqub, H. Wu, K. Kühnlenz, D. Wollherr, and M. Buss, "Dynamic manipulation: Nonprehensile ball catching," in *Proceedings of the IEEE 18th Mediterranean Conference on Control and Automation*, Marrakech, Morocco, June 2010, pp. 365–370.

48) J.-C. Ryu, F. Ruggiero, and K. M. Lynch, "Control of nonprehensile rolling manipulation: balancing a disk on a disk," in *Proceedings of the IEEE International Conference on Robotics Automation*, Saint Paul, Minnesota, USA, May 2012, pp. 3232–3237.

49) A. Namiki, Y. Imai, M. Ishikawa, and M. Kaneko, "Development of a high-speed multifingered hand system and its application to catching," in *Proceedings of the IEEE/RSJ International Conference on Intelligent Robots and Systems*, vol. 3, Las Vegas, Nevada, USA, October 2003, pp. 2666–2671.

50) Y. Imai, A. Namiki, K. Hashimoto, and M. Ishikawa, "Dynamic active catching using a high-speed multifingered hand and a high-speed vision system," in *Proceedings of the IEEE International Conference on Robotics Automation*, vol. 2, New Orleans, LA, USA, April 2004, pp. 1849–1854.

51) M. Kaneko, M. Higashimori, R. Takenaka, A. Namiki, and M. Ishikawa, "The 100g capturing robot -too fast to see," *IEEE Transactions on Mechatronics*, vol. 8, no. 1, pp. 37–44, March 2003.

52) M. Higashimori, M. Kaneko, A. Namiki, and M. Ishikawa, "Design of the 100g capturing robot based on dynamic preshaping," *The International Journal of Robotics Research*, vol. 24, no. 9, pp. 743–753, September 2005.

53) N. Furukawa, A. Namiki, S. Taku, and M. Ishikawa, "Dynamic regrasping using a high-speed multifingered hand and a high-speed vision system," in *Proceedings of the IEEE International Conference on Robotics and Automation*, Orlando, Florida, USA, May 2006, pp. 181–187.

54) M. Higashimori, M. Kimura, I. Ishii, and M. Kaneko, "Dynamic capturing strategy for a 2-*d* stick-shaped object based on friction independent collision," *IEEE Transactions on Robotics*, vol. 23, no. 3, pp. 541–552, June 2007.

55) S. Haddadin, K. K, M. Kunze, and A. Albu-Schäffer, "Exploiting potential energy storage for cyclic manipulation: an analysis for elastic dribbling with an anthropomorphic robot," in *Proceedings of the IEEE/RSJ International Conference on Intelligent Robots and Systems*, San Francisco, CA, USA, September 2011, pp. 1789–1796.

56) G. Bätz, M. Scheint, and D. Wollherr, "Toward dynamic manipulation for humanoid robots: experiments and design aspects," *International Journal of Humanoid Robotics*, vol. 8, no. 3, pp. 513–532, September 2011.

57) T. Kizaki and A. Namiki, "Two ball juggling with high-speed hand-arm and high-speed vision system," in *Proceedings of the IEEE International Conference on Robotics Automation*, Saint Paul, MN, USA, May 2012, pp. 1372–1377.

58) H. Wakamatsu, S. Hirai, and K. Iwata, "Static analysis of deformable object grasping based on bounded force closure," in *Proceedings of the IEEE International Conference on Robotics and Automation*, vol. 4, Minneapolis, MN, USA, 1996, pp. 3324–3329.

59) D. Sun, Y. Liu, and J. K. Mills, "Cooperative control of a two-manipulator system handling a general flexible object," in *Proceedings of the IEEE/RSJ International Conference on Intelligent Robots and Systems*, vol. 1, Grenoble, France, September 1997, pp. 5–10.

60) A. M. Howard and G. A. Bekey, "Recursive learning for deformable object manipulation," in *Proceedings of the 8th International Conference on Advanced Robotics*, Monterey, CA, USA, July 1997, pp. 939–944.

61) ——, "Intelligent learning for deformable object manipulation," *Autonomous Robots*, vol. 9, no. 1, pp. 51–58, August 2000.

62) D. Henrich, T. Ogasawara, and H. Wörn, "Manipulating deformable linear objects - contact states and point contacts-," in *Proceedings of the IEEE International Symposium on Assembly and Task Planning*, Porto, Portugal, July 1999, pp. 198–204.

63) A. Remde, D. Henrich, and H. Wörn, "Manipulating deformable linear objects -contact state transitions and transition conditions-," in *Proceedings of the IEEE/RSJ International Conference on Intelligent Robots and Systems*, vol. 3, Kyongju, Korea, October 1999, pp. 1450–1455.

64) S. Yue and D. Henrich, "Manipulating deformable linear objects: attachable adjustment-motions for vibration reduction," *Journal of Robotic Systems*, vol. 18, no. 7, pp. 375–389, July 2001.

65) ——, "Manipulating deformable linear objects: sensor-based fast manipulation during vibration," in *Proceedings of the IEEE International Conference on Robotics Automation*, vol. 3, Washington, DC, USA, May 2002, pp. 2467–2472I.

66) A. Schlechter and D. Henrich, "Manipulating deformable linear objects: manipulation skill for active damping of oscillations," in *Proceedings of the IEEE/RSJ International Conference on Intelligent Robots and Systems*, vol. 2, Lausanne, Switzerland, October 2002, pp. 1541–1546.

67) J. Acker and D. Henrich, "Manipulation of deformable linear objects: from geometric model towards program generation," in *Proceedings of the IEEE International Conference on Robotics Automation*, Barcelona, Spain, April 2005, pp. 1541–1457.

68) T. Fukuda, T. Matsuno, and F. Arai, "Flexible object manipulation by dual manipulator system," in *Proceedings of the IEEE International Conference on Robotics Automation*, vol. 2, San Francisco, CA, USA, 2000, pp. 1955–1960.

69) S. Hirai, T. Tsuboi, and T. Wada, "Robust grasping manipulation of deformable objects," in *Proceedings of the IEEE International Symposium on Assembly and Task Planning*, Fukuoka, Japan, May 2001, pp. 411–416.

70) G. L. Foresti and F. A. Pellegrino, "Automatic visual recognition of deformable objects for grasping and manipulation," *IEEE Transactions on Systems, Man, and Cybernetics, Part C: Applications and Reviews*, vol. 34, no. 3, pp. 325–333, August 2004.

71) M. Hashimoto, T. Ichikawa, S. Inui, and Y. Horiba, "Dynamic manipulation of a string using a manipulator -parameter identification and control based on a rigid body link model-," in *Proceedings of the IEEE International Conference on Robotics Automation*, vol. 5, New Orleans, LA, USA, April 2004, pp. 4815–4820.

72) H. Wakamatsu, A. Tsumaya, E. Arai, and S. Hirai, "Planning of one-handed knotting/raveling manipulation of linear objects," in *Proceedings of the IEEE International Conference on Robotics Automation*, vol. 2, New Orleans, LA, USA, April 2004, pp. 1719–1725.

73) ——, "Manipulation planning for knotting/unknotting and tightly tying of deformable linear objects," in *Proceedings of the IEEE International Conference on Robotics Automation*, Barcelona, Spain, April 2005, pp. 2505–2510.

74) ——, "Manipulation planning for unraveling linear objects," in *Proceedings of the IEEE International Conference on Robotics Automation*, Orlando, Florida, USA, May 2006, pp. 2485–2490.

75) ——, "Unraveling of deformable linear objects based on 2d information about their crossing states," in *Proceedings of the IEEE/RSJ International Conference on Intelligent Robots and Systems*, Beijing, China, October 2006, pp. 3873–3878.

76) H. Wakamatsu, E. Arai, and S. Hirai, "Knotting/unknotting manipulation of deformable linear objects," *International Journal of Robotics Research*, vol. 25, no. 4, pp. 371–395, 2006.

77) S. Garg and A. Dutta, "Grasping and manipulation of deformable objects based on internal force requirements," *International Journal of Advanced Robotic Systems*, vol. 3, no. 2, pp. 107–114, 2006.

78) T. Matsuno, D. Tamaki, F. Arai, and T. Fukuda, "Manipulation of deformable linear objects using knot invariants to classify the object condition based on image sensor information," *IEEE/ASME Transactions on Mechatronics*, vol. 11, no. 4, pp. 401–408, August 2006.

79) T. Matsuno and T. Fukuda, "Manipulation of flexible rope using topological model based on sensor information," in *Proceedings of the IEEE/RSJ International Conference on Intelligent Robots and Systems*, Beijing, China, October 2006, pp. 2638–2643.

80) M. Saha and P. Isto, "Manipulation planning for deformable linear objects," *IEEE Transactions on Robotics*, vol. 23, no. 6, pp. 1141–1150, December 2007.

81) Y. Yamakawa, A. Namiki, M. Ishikawa, and M. Shimojo, "One-handed knotting of a flexible rope with a high-speed multifingered hand having tactile sensors," in *Proceedings of the IEEE/RSJ International Conference on Intelligent Robots and Systems*, San Diego, CA, USA, October 2007, pp. 703–708.

82) Y. Yamakawa, A. Namiki, and M. Ishikawa, "Motion planning for dynamic knotting of a flexible rope with a high-speed robot arm," in *Proceedings of the IEEE/RSJ International Conference on Intelligent Robots and Systems*, Taipei, Taiwan, October 2010, pp. 49–54.

83) ——, "Dynamic manipulation of a cloth by high-speed robot system using high-speed visual feedback," in *Preprints of the 18th World Congress of the International Federation of Automatic Control (IFAC)*, Milano, Italy, 2011, pp. 8076–8081.

84) ——, "Simple model and deformation control of a flexible rope using constant, high-speed motion of a robot arm," in *Proceedings of the IEEE International Conference on Robotics Automation*, Saint Paul, MN, USA, May 2012, pp. 2249–2254.

85) Y. Kita, T. Ueshiba, E. S. Neo, and N. Kita, "A method for handling a specific part of clothing by dual arms," in *Proceedings of the IEEE/RSJ International Conference on Intelligent Robots and Systems*, St. Louis, USA, October 2009, pp. 4180–4185.

86) M. Shibata, T. Ota, and S. Hirai, "Wiping motion for deformable object handling," in *Proceedings of the IEEE International Conference on Robotics and Automation*, Kobe, Japan, May 2009, pp. 134–139.

87) C. Bersch, B. Pitzer, and S. Kammel, "Bimanual robotic cloth manipulation for laundry folding," in *Proceedings of the IEEE/RSJ International Conference on Intelligent Robots and Systems*, San Francisco, CA, USA, September 2011, pp. 1413–1419.

88) T. V. Vinh, T. Tomizawa, S. Kudoh, and T. Suehiro, "A new strategy for making a knot with a general-purpose arm," in *Proceedings of the IEEE International Conference on Robotics Automation*, Saint Paul, Minnesota, USA, May 2012, pp. 2217–2222.

89) A.-M. Cretu, P. Payeur, and E. M. Petriu, "Soft object deformation monitoring and learning for model-based robotic hand manipulation," *IEEE Transactions on Systems, Man, and Cybernetics, Part B: Cybernetics*, vol. 42, no. 3, pp. 740–753, June 2012.

90) F. F. Khalil and P. Payeur, "Dexterous robotic manipulation of deformable objects with multi-sensory feedback - a review," in *Robot manipulators trends and development*, A. Jimenez and B. M. A. Hadithi, Eds. InTech, March 2010, ch. 28, pp. 587–619.

91) P. Jimenez, "Survey on model-based manipulation planning of deformable objects," *Robotics and Computer-Integrated Manufacturing*, vol. 28, no. 2, pp. 154–163, April 2012.

92) E. W. Weisstein. Unknot. From MathWorld -A Wolfram Web Resource. [Online]. Available: http://mathworld.wolfram.com/Unknot.html

93) M. Higashimori, K. Utsumi, Y. Omoto, and M. Kaneko, "Dynamic manipulation inspired by the handling of a pizza peel," *IEEE Transactions on Robotics*, vol. 25, no. 4, pp. 829–838, August 2009.

94) M. T. Mason and J. K. Salisbury, *Robot Hands and the Mechanics of Manipulation.* The MIT Press, 1985.

95) M. T. Mason, "Mechanics and planning of manipulator pushing operations," *The International Journal of Robotics Research*, vol. 5, no. 3, pp. 53–71, 1986.

96) K. M. Lynch, "Locally controllable manipulation by stable pushing," *IEEE Transactions on Robotics and Automation*, vol. 15, no. 2, pp. 318–327, 1999.

97) P. Tiezzi and I. Kao, "Modeling of viscoelastic contacts and evolution of limit surface for robotic contact interface," *IEEE Transactions on Robotics*, vol. 23, no. 2, pp. 206–217, 2007.

98) M. Higashimori, Y. Omoto, and M. Kaneko, "Non-grasp manipulation of deformable object by using pizza handling mechanism," in *Proceedings of the IEEE International Conference on Robotics and Automation*, Kobe, Japan, May 2009, pp. 120–125.

99) M. Moore and J. Wihelms, "Collision detection and response for computer animation," *Computer Graphics*, vol. 22, no. 4, pp. 289–298, August 1988.

100) J. K. Patel, C. H. Kapadia, and D. B. Owen, *Handbook of statistical distributions*, ser. Statistics: textbooks and monographs. Marcel Dekker, Inc., 1976, p. 212.

101) A. C. G. Mitchell and M. W. Zemansky, *Resonance radiation and excited atoms.* Cambridge University Press, 1934, pp. 158–163.

102) R. G. Newton, *Scattering theory of waves and particles*, ser. International Series in Pure and Applied Physics. McGraw-Hill, 1966, pp. 62–63,326.

103) V. J. Logeeswaran, F. E. H. Tay, M. L. Chan, F. S. Chau, and Y. C. Liang, "First harmonic ($2f$) characterisation of resonant frequency and q-factor of micromechanical transducers," *Analog Integrated Circuits and Signal Processing*, vol. 37, no. 1, pp. 17–33, 2003.

104) D. C. Montgomery and E. A. Peck, *Introduction to Linear Regression Analysis*, 2nd ed., ser. Wiley series in probability and mathematical statistics. Applied probability and statistics. Wiley-Interscience, 1992, ch. 2, pp. 18–24.

105) *SigmaPlot 12 User's Manual.* Systat Software, Inc., 2010, ch. 15, pp. 655–657.

Achievements

Journal Papers

1. I. G. Ramirez-Alpizar, M. Higashimori, M. Kaneko, C.-H. D. Tsai, and I. Kao, "Dynamic Nonprehensile Manipulation for Rotating a Thin Deformable Object: an Analogy to Bipedal Gaits," *IEEE Transactions on Robotics*, vol. 28, no. 3, pp. 607–618, June 2012.

2. I. G. Ramirez-Alpizar, M. Higashimori, and M. Kaneko, "Characterization of Deformable Objects by Using Dynamic Nonprehensile Manipulation," *Journal of Robotics and Mechatronics*, vol. 25, no. 1, February 2013 (Accepted).

Proceedings of International Conferences

Full-Paper Review

1. I. G. Ramirez-Alpizar, M. Higashimori, M. Kaneko, C.-H. Tsai, and I. Kao, "Nonprehensile Dynamic Manipulation of a Sheet-like Viscoelastic Object," *Proceeding of IEEE International Conference on Robotics and Automation*, pp. 5103–5108, Shanghai, China, May 2011.

2. I. G. Ramirez-Alpizar, M. Higashimori, and M. Kaneko, "Estimation of a Thin Flexible Object with Bipedal Gaits," *Proceeding of IEEE International Conference on Automation Science and Engineering*, pp. 952–957, Seoul, Korea, August 2012.

Abstract Review

1. I. G. Ramirez-Alpizar, M. Higashimori, and M. Kaneko, "Bipedal Gait Like Motions of a Thin Viscoelastic Object," *Proceeding of 2011 International Symposium on Micro-Nano Mechatronics and Human Science*, pp. 519–522, Nagoya, Japan, November 2011.

Domestic Conferences in Japan

1. I. Ramirez, M. Higashimori, and M. Kaneko, "Nonprehensile Manipulation of a Visco-elastic Object," *The 28th Annual Conference of the Robotics Society of Japan*, 1D1-4, Nagoya, September 2010.

Award

1. IEEE Robotics and Automation Society Japan Chapter Young Award to Ramirez Alpizar Ixchel Georgina, (International Conference, Full-Paper Review no. 1)

Research Aid

1. International Exchange Grant sponsored by Osaka University Engineering Society to Ramirez Alpizar Ixchel Georgina (First period of Heisei year 24th)

Other Achievements

1. A. Shibata, M. Higashimori, I. G. Ramirez-Alpizar, and M. Kaneko, "Tongue Elasticity Sensing with Muscle Contraction Monitoring," *Proceeding of the 2012 ICME International Conference on Complex Medical Engineering*, pp. 511–516, Kobe, Japan, July 2012.

2. T. Inahara, M. Higashimori, I. Ramirez, and M. Kaneko, "Deformation Control of a Rheological Object by Nonprehensile Manipulation," *Proceedings of the 2011 JSME Conference on Robotics and Mechatronics*, 2A1-K04, Okayama, Japan, May 2011.

3. M. Higashimori, I. G. Ramirez Alpizar, and M. Kaneko, "Modeling and Handling of Deformable Object by Nonprehensile Dynamic Manipulation," *Proceeding of the International Conference on Advanced Mechatronics 2010*, pp. 427–432, Osaka, Japan, October 2010.

4. I. Ramirez, M. Hamaguchi, and T. Taniguchi, "Sliding Mode Control Based on Position and Inner Force of Two Manipulators in Cooperative Work," *The 48th Conference of the Japan Society of Mechanical Engineers Chugoku-Shikoku Branch*, 909, Hiroshima, Japan, March 2010.

5. J. Jaimes-Ponce, R. Alcantara-Ramirez, I. I. Siller-Alcala, I. Ramirez-Alpizar, N. Najera-Ramos, "Design, Development and Control of a Water Tank System," *WSEAS Transactions on Advances in Engineering Education*, issue 8, vol. 3, pp. 739–745, August 2006.